

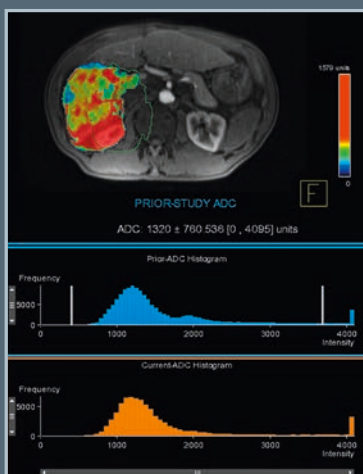
MAGNETOM Flash

The Magazine of MRI

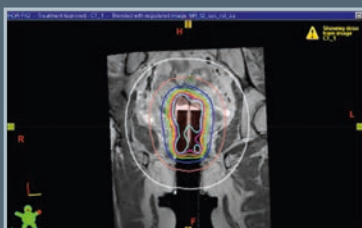
Issue Number 4/2013 | ASTRO Edition

Not for distribution in the US

Functional, Volumetric,
Treatment Response Assess-
ment Using MR OncoTreat
Page 24

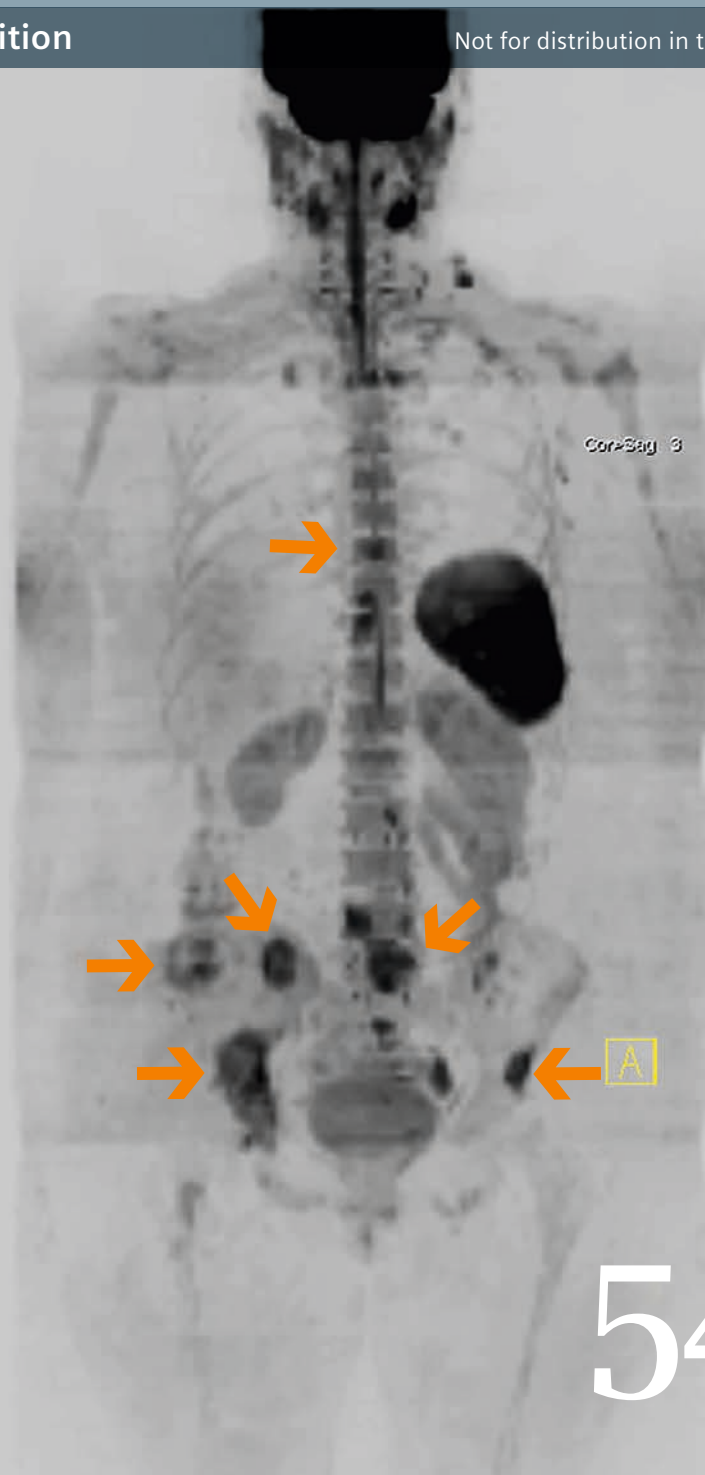


Optimizing MRI for
Radiation Oncology
Page 45



How-I-do-it

Tissue 4D on syngo.via
Page 18





Professor Heinz-Peter Schlemmer is the head of the radiology department at the German Cancer Research Center and coordinator of the 'Imaging and Radiooncology' research program. He is a professor of oncological radiology at the Medical Faculty of Heidelberg University. This year he founded the 'Oncological Imaging' working group within the German Roentgen Ray Society. In 2014 he will be the President of the International Cancer Imaging Society (ICIS) and host the ICIS's annual conference as a multidisciplinary event, entitled 'Working Together for the Patient'. The meeting will bring together radiologists, nuclear medicine physicians, and radiooncologists in Heidelberg for joint teaching and discussion.

Dear MAGNETOM Flash reader,

As radiologists, we are important partners of the interdisciplinary oncology team. The increasing complexity of diagnostic and treatment processes brings with it the need for ever closer collaboration among physicians in surgery, internal medicine, radiation therapy and radiology. And with many tumor diseases, imaging plays a key role in treatment decision making.

The rapid development of MRI and computer technology has provided us with impressive tools that allow us to detect and functionally/biologically characterize tumors with ever more accuracy. For many tumor entities, early detection, precise diagnosis, image-guided biopsy, staging of local and distant tumor growth, tumor characterization, treatment planning, treatment, treatment monitoring and follow-up essentially rely on imaging data. Changes of imaging parameters during treatment provide important information with regard to individual responses to treatment. Imaging is also an indispensable tool in oncology research and in the development of new oncological treatment procedures.

Particularly close links already exist but will increasingly be expanded between radiology and radiation

oncology. With the continued advancement of high-precision radiation therapy, time-resolved 4D and functional/biological MRI techniques are becoming increasingly important for target volume definition in radiation therapy planning as well as for intra- and interfractional tumor tracking. These imaging parameters are also essential for treatment monitoring and post-treatment follow-up supporting quality assurance and further improvement of therapy approaches.

MR imaging covers a wide range of techniques from time and spatially resolved high-resolution multiparametric MRI with e.g. diffusion and perfusion weighting through to whole-body MRI and PET/MRI with specific radiotracers. In future, it will be increasingly important that these complex examinations are performed and interpreted in a standardized way. Objective and quantitative image parameters can be used as biomarkers for individual tumor characterization and thus the stratification of patients. Oncological imaging can, in this way, contribute significantly to individually tailored patient treatment and objective assessment of treatment response. Prospective multicenter

studies, which are essential in clinical research, often use imaging parameters as end points. At present, it is common practice to use the merely morphological but internationally recognized RECIST criteria for solid tumors. But new functional MRI techniques will be of substantial importance for early assessment and further improvement of targeted therapies.

Another challenge is the collaboration among us radiologists, as modern MRI technology provides us with methods and concepts that go far beyond our organ-related subspecialization. Malignant tumors have *per se* infiltrative and metastatic potential why they should be considered systemic diseases that can affect the whole body until proven otherwise. It may therefore be necessary to image several body regions and organ systems respectively, or even the whole body in order to spy out distant tumor growth and metastatic spread. In the case of primary systemic tumor diseases such as hematologic tumors and tumors of the lymphatic system, this is mandatory.

Oncological radiology, however, is more than just performing complex MRI examinations. The entire proce-

“Oncological imaging contributes significantly to individually-tailored patient treatment and objective assessment of therapy response.”

Professor Heinz-Peter Schlemmer

From examination through to image postprocessing, standardized reporting, suitable report documentation, report communication as well as integration into treatment and treatment monitoring is a multi-layered, complex process that poses many challenges. These can only be met with the help of advanced IT concepts. Intelligent and process-oriented IT allows us to master modern MRI techniques in daily practice and is indispensable for competent interdisciplinary

communication. Only in this way can the complex and comprehensive image information be of benefit in ensuring optimal individual treatment of cancer patients.

In this MAGNETOM Flash magazine you will find exciting examples from the broad spectrum of oncological MRI applications. Using clinical examples, renowned experts demonstrate the potential of multiparametric MRI, whole-body MRI and MR-PET and how functional MRI parameters can

be used in radiation therapy planning. In addition, the possibilities of intelligent IT concepts for reporting and workflow optimization are illustrated.

I hope you find the articles interesting and exciting and wish you much success in your daily work for the wellbeing of your patients!



Editorial Board

We appreciate your comments.

Please contact us at magnetomworld.med@siemens.com



Antje Hellwich
Associate Editor



Wellesley Were
MR Business Development
Manager Australia and
New Zealand



Ralph Strecker
MR Collaborations Manager,
Sao Paulo, Brazil



Sven Zühlsdorff, Ph.D.
Clinical Collaboration
Manager, Chicago, IL, USA



Gary R. McNeal, MS (BME)
Advanced Application
Specialist, Cardiovascular
MR Imaging Hoffman
Estates, IL, USA



Peter Kreisler, Ph.D.
Collaborations & Applications,
Erlangen, Germany

Review Board

Lisa Chuah, Ph.D.

Global Marketing Manager Neurology

Wilhelm Horger

Application Development Oncology

Michelle Kessler

US Installed Base Manager

Berthold Kiefer, Ph.D.

Oncological and Interventional Applications

Sunil Kumar S.L., Ph.D.

Senior Manager Applications

Reto Merges

Head of Outbound Marketing MR Applications

Heiko Meyer, Ph.D.

Neuro Applications

Nashiely Sofia Pineda Alonso, Ph.D.

Global Marketing Manager

Men's and Women's Health

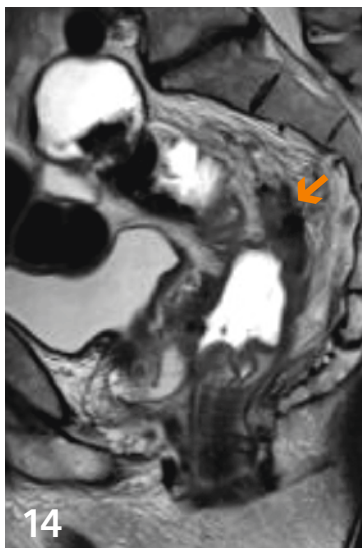
Silke Quick

Global Marketing Manager Body Imaging

Heike Weh

Clinical Data Manager

Content



Staging of rectal cancer

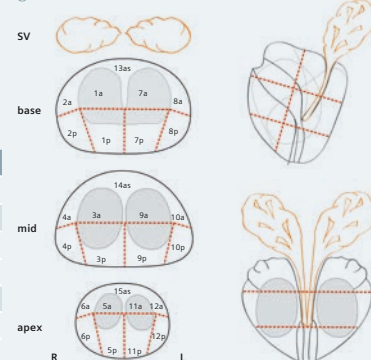
Standardized MRI Reporting Scheme

Name: _____
 Date: _____
 PSA: _____
 Previous Biopsies: _____
 Previous MRI scans: _____

Individual Scoring

Region	T2	DWI	DCE	MRS	Sum	PI-RADS

Total score PI-RADS:
 PI-RADS: 1 – benign; 2 – most probably benign;
 3 – intermediate; 4 – probably malignant;
 5 – highly suspicious of malignancy



30

PI-RADS



Learn from the experience of other MAGNETOM users

The MAGNETOM World is the community of Siemens MR users worldwide, providing you with relevant clinical information at your fingertips. Here you will find application tips and clinical methods to optimize your daily work. Lectures and presentations from experts in the field will allow you to be exposed to new ideas and alternative clinical approaches. Put the advantages of MAGNETOM World to work for you!

How I do it

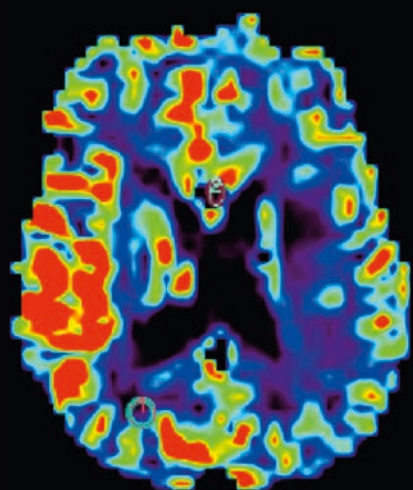
- 6** Whole-Body Diffusion-Weighted MRI for Bone Marrow Tumor Detection
 Anwar R. Padhani,
 Heminder Sokhi

Clinical Oncology

- 14** Comprehensive MRI-Based Staging of Rectal Cancer
 Arnd-Oliver Schäfer,
 Mathias Langer

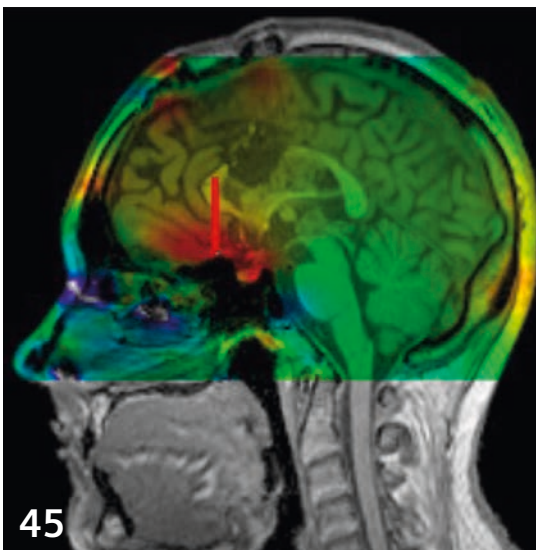
How I do it

- 18** Tissue 4D on syngo.via
 Anja Fernandez Carmona,
 Radim Chrastek



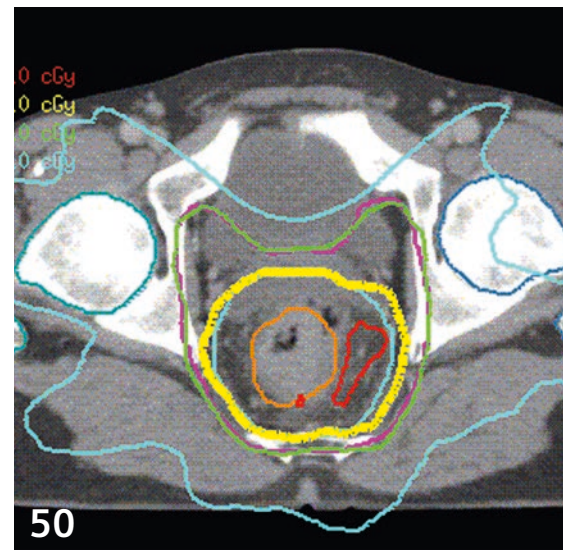
39

Therapy response



45

MRI for radiation oncology



50

MAGNETOM Combi Suite

Clinical Oncology

- 24** Case Report: Functional, Volumetric, Treatment Response Assessment Using MR OncoTreat*
Susanne Bonekamp, Ihab R. Kamel

Clinical Men's Health

- 30** PI-RADS Classification: Structured Reporting for MRI of the Prostate
Matthias Röthke, et al.

Clinical Oncology

- 39** Case Study: Tumor Recurrence versus Treatment-Induced Change in a Patient with High-Grade Gliomas
Girish Fatterpekar, et al.

Clinical Radiation Oncology

- 42** Clinical Application of Diffusion Tensor Imaging in Radiation Planning for Brain Tumors
Jatta Berberat, et al.
- 45** Optimizing MRI for Radiation Oncology: Initial Investigations
James Balter, et al.

Product News

- 50** MAGNETOM Combi Suite Radiation Therapy
Annemarie Hausotte

The information presented in MAGNETOM Flash is for illustration only and is not intended to be relied upon by the reader for instruction as to the practice of medicine. Any health care practitioner reading this information is reminded that they must use their own learning, training and expertise in dealing with their individual patients. This material does not substitute for that duty and is not intended by Siemens Medical Solutions to be used for any purpose in that regard. The treating physician bears the sole responsibility for the diagnosis and treatment of patients, including drugs and doses prescribed in connection with such use. The Operating Instructions must always be strictly followed when operating the MR System. The source for the technical data is the corresponding data sheets.

*Work in progress: The product is still under development and not commercially available yet. Its future availability cannot be ensured.

Whole Body Diffusion-Weighted MRI for Bone Marrow Tumor Detection

Heminder Sokhi, MBCHB, MRCS, FRCR; Anwar R. Padhani, MB BS, FRCP, FRCR

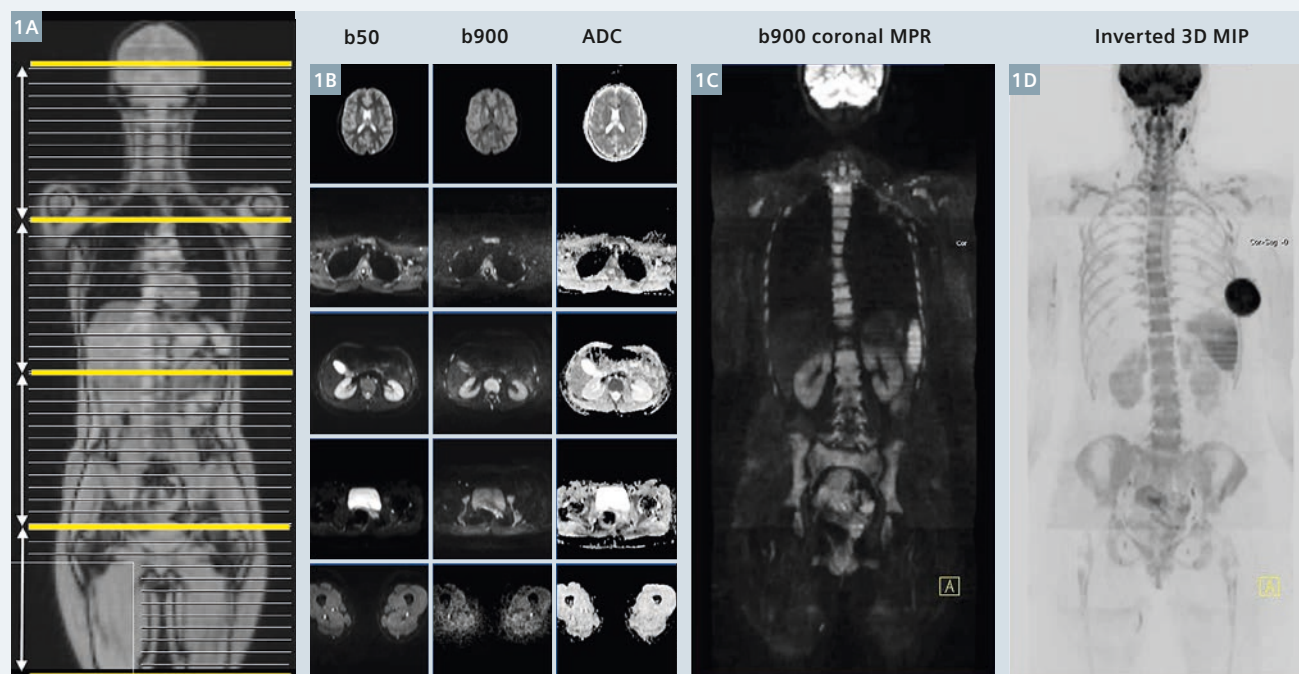
Paul Strickland Scanner Centre, Mount Vernon Cancer Centre, Northwood, Middlesex, UK

Background

Recent years have seen the evolution of body diffusion-weighted MRI (DWI) into an exciting, whole body (WB-DWI) imaging technique with a distinct clinical utility, particularly in the context of cancer imaging [1-3]. It is clear that, with its excellent sensitivity for detecting marrow infiltration and good spatial resolution, WB-DWI has the capability of providing functional information which complements conventional anatomic

MRI methods. At our institution, we use WB-DWI principally for evaluation of bone marrow metastases, both for detection and for evaluating disease response to therapy, where we have found particular utility for multiple myeloma, breast and prostate cancer. The technique is particularly useful when there is a need to minimize radiation exposure for serial evaluation of younger patients, pregnant women with cancer and in those in

whom intravenous contrast medium is contraindicated (allergy or impaired renal function). This article focuses on the technique for Siemens systems, common artifacts encountered in clinical practice, and alludes to its clinical utility regarding skeletal metastases detection. We do not discuss response assessment of malignant bone marrow disease in any detail but there are clear strengths in this regard also [2].



1 WB-DWI workflow. 27-year-old woman with sarcomatoid left breast cancer. The bone marrow pattern is normal for age. Axial DWI from the skull base to the mid-thigh is performed using 2 b-values (50 and 900 s/mm²) with a slice thickness of 5 mm in 4 stations. The b900 images are reconstructed into the coronal plane (5 mm) and displayed as thick 3D MIPs (inverted grey scale). ADC images are computed inline with mono-exponential fitting of b50 and b900 signal intensities.

Technique of whole body DWI

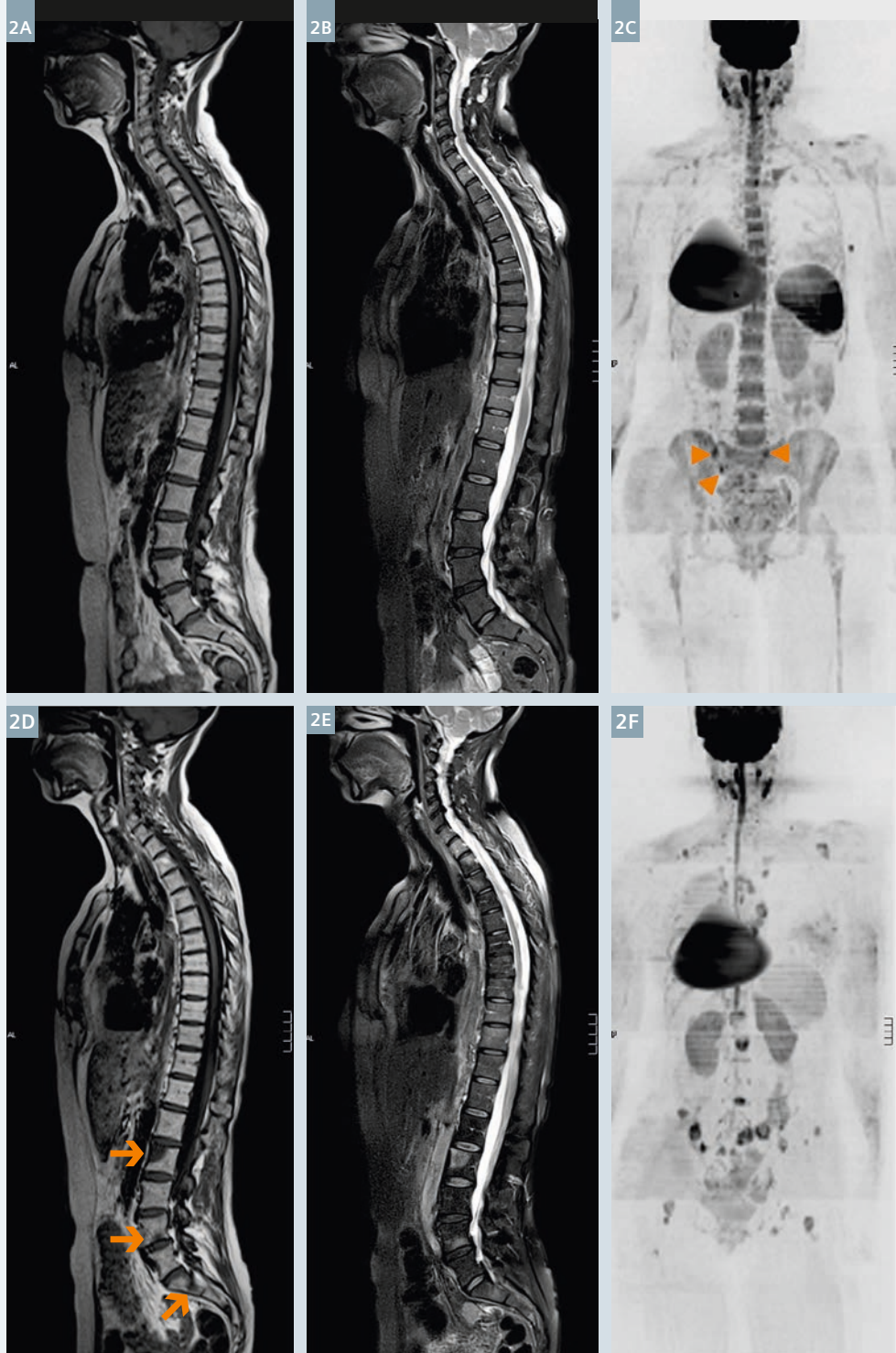
Although imaging at 3T increases the signal-to-noise ratio, WB-DWI at this field strength remains challenging because of increased susceptibility artifacts and poorer fat suppression; currently, we find that WB-DWI is best performed on a longer bore 1.5T scanner. All our WB-MRI scans are done on a Siemens MAGNETOM Avanto scanner equipped with a continuous moving table option (TimCT) and total imaging matrix (Tim) body surface coils. We always acquire morphologic images to accompany the WB-DWI images.

Our morphologic images consist of

- 1 whole spine: T1-weighted, turbo spin-echo sagittal images (acquisition time 2:21 minutes),
- 2 whole spine: T2-weighted, turbo spin-echo sagittal images with spectral fat suppression (acquisition time 2:36 minutes),
- 3 whole body: T1-weighted, gradient-echo axial 2-point Dixon sequence (acquisition time 3:00 minutes) that automatically generates four image-sets (in-phase, opposed phase, water-only (WO), and fat-only (FO)) from which T1w fat% and non-fat% images can be calculated if needed.
- 4 Finally whole body (vertex to upper mid thighs): T2-weighted, short-tau inversion recovery (STIR) axial images with half-Fourier single shot turbo spin-echo (HASTE) readouts (acquisition time 4:00 minutes) is also undertaken.

The axial images from the skull vault to the mid-thighs are acquired using the continuous table movement technology, employing multiple breath-holds for image acquisitions of the chest, abdomen, pelvis and upper thighs.

Axial DWI from the skull vault to the mid-thighs is then performed using b-values of 50 s/mm² and a b-value of 900 s/mm² with a slice thickness of 5 mm. The axial DWI acquisition is usually achieved in 4 contiguous stations using a free-breathing technique, with each station taking approximately 6 minutes to acquire. Our preferred



2 Bone marrow hypoplasia due to chemotherapy with disease progression. 49-year-old woman with metastatic breast cancer before and after 3 cycles of carboplatin chemotherapy. Both rows left-to-right: spine T1w spin-echo, spine T2w spin-echo with spectral fat saturation and b900 3D MIP (inverted scale) images. Top row before chemotherapy shows normal background bone marrow pattern with superimposed small volume bone metastases (arrow heads). Bottom row after chemotherapy shows disease progression with enlarging and new bony metastases (arrows). Note that bone marrow hypoplasia has developed in the ribs, spine and pelvis. Note reductions of signal intensity of the spleen secondary to iron deposition due to blood transfusions. There is a right sided silicone containing breast enhancement bra pad in place on both examinations.



3 Poor visibility of treated metastases and osteoblastic metastases. 69-year-old with metastatic prostate cancer on long term, third line hormonal therapy with abiraterone being evaluated for rising serum prostate specific antigen (PSA) levels. He has had an excellent response to 2 years of treatment with residual abnormalities in his bone marrow visible on T1w (3A) and T2w (with fat suppression) spinal images. No hyperintensity is seen on the b900 3D MIP (inverted scale) image (3C) indicating the absence of highly cellular infiltrative disease. Bone scan (3D) shows a focal area of osteoblastic uptake in the intertrochanteric region of the left femur (arrow) which is not visible as a discrete region on the b900 3D inverted MIP image.

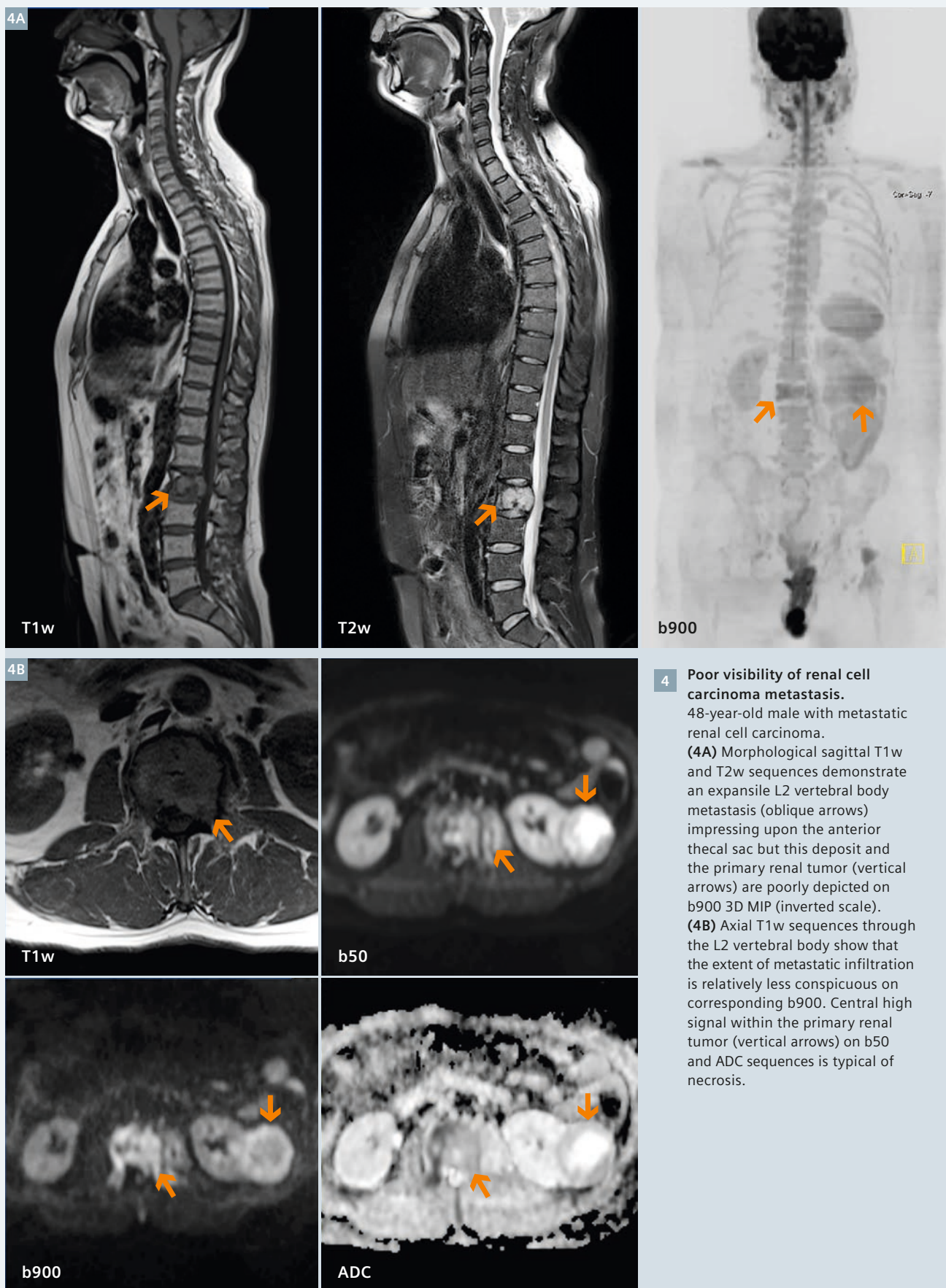
method for fat suppression uses inversion recovery because it allows uniform fat suppression over large fields-of-view [4]. An artificially 'fractured spine' observed on the post processed aligned images as a consequence of alignment mismatch can be minimized by manually adjusting and maintaining the transmitter frequency for each station. The b900 value images are reconstructed in the coronal plane (5 mm) and as thick 3D maximum intensity projections (MIPs) which are displayed using an inverted grey scale. ADC maps are computed inline with system software using mono-exponential fitting in which each voxel reflects the tissue diffusivity (units: $\mu\text{m}^2/\text{s}$) (Fig. 1).

Detailed scanning parameters for each sequence have been published [4, 5]; the entire examination takes 52 minutes to complete. The illustrations of this article were obtained from more than 2,000 WB-DWI scans done at our institution in the last 4 years using this protocol.

Normal bone marrow signal on WB-DWI

A thorough understanding of normal bone marrow signal distribution on b900 value images is vital for the accurate detection, characterization and treatment assessment of skeletal metastases [5]. This is because the bone marrow distribution can be visu-

alized by WB-DWI. The normal adult bone marrow pattern which is established by the age of 25 years can be seen as uniformly distributed, intermediate high signal intensity distributed in the axial skeleton (mixed red bone marrow); yellow marrow in the appendicular skeleton shows no/lower signal intensity (Fig. 1). The changing distribution of the normal marrow is also exquisitely demonstrated on WB-DWI. Red marrow conversion to yellow marrow is dependent on patient age, gender and underlying medical conditions [6]. Both bone marrow hypo- and hypercellularity are well depicted on WB-DWI.



The relationship between bone marrow cellularity and ADC values is non linear and highly dependent on the water, cellular and fat content of the marrow. The reduced water content [6], the larger-sized fat cells, the hydrophobic nature of fat and poorer perfusion all contribute to lower diffusion-weighted signal intensities and ADC values of the yellow bone marrow. On the other hand, with increasing cellularity and water content and greater perfusion, mixed yellow-red bone marrow returns higher signal intensities and paradoxically higher ADC values [5, 7-9].

Skeletal metastases detection

Skeletal metastases appear as focal or diffuse areas of high-signal intensity on high b-value WB-DWI (Fig. 2).

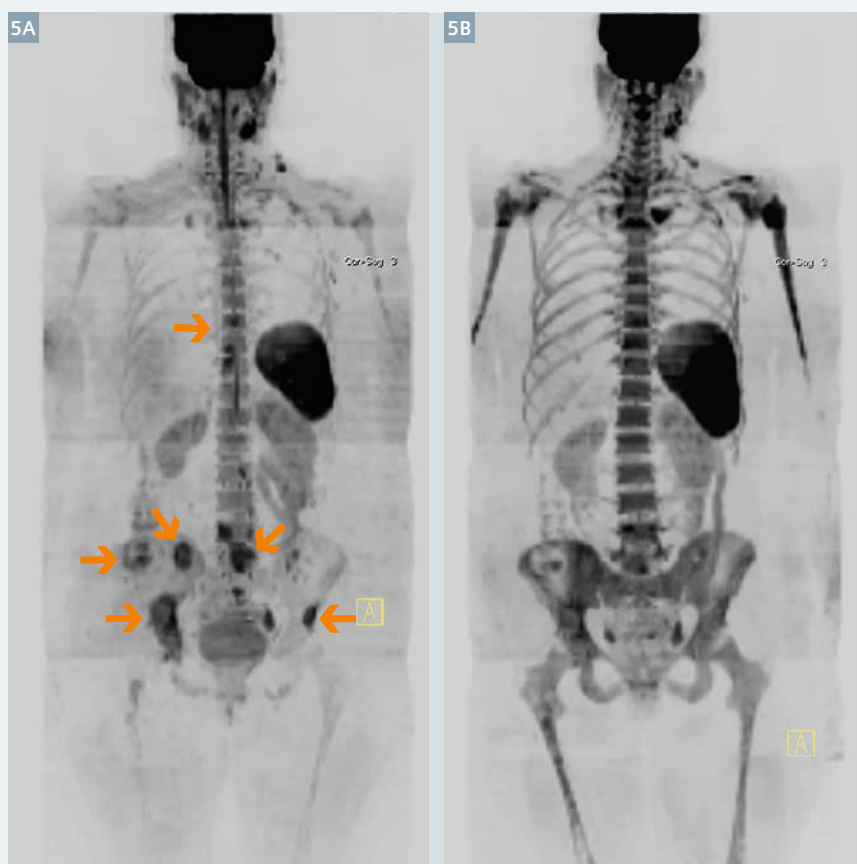
The ability to detect bone marrow lesions is dependent on the intrinsic signal intensity of the deposits and the background bone marrow. Other factors determining the visibility of bone lesions include their anatomic location and treatment status. It is imperative that WB-DWI is performed and interpreted in conjunction with conventional morphological WB-MRI sequences rather than in isolation.

This is because false positive and negative lesions do occur. This assertion was highlighted by a recent meta-analysis, which demonstrated that the high sensitivity of WB-DWI to detect metastases was at the expense of specificity [1].

Generally, infiltrative cellular lesions are better detected than *de-novo* sclerotic or treated lytic/sclerotic lesions (Fig. 3). This is due to the lower water and cellular content of sclerotic and treated metastases [7, 10]. This is the likely reason for the improved visibility of bone metastases of untreated breast cancer compared to prostate cancer; *de-novo* sclerotic metastases are commoner in prostate cancer. WB-DWI is better at detecting skeletal lesions from smaller cancer cell infiltrations such as those due to breast cancer, myeloma, lymphoma and small cell cancers as well as neuroendocrine tumors. On the other hand, bony metastases from clear cell renal cancers are sometimes poorly depicted (the presence of necrosis, large sized tumor cells and inherent lipogenesis contribute to the poorer visualization) (Fig. 4). On occasion, the high magnetic field susceptibility of melanin can also impair depiction of melanoma metastases.

The detection of skeletal metastases on WB-DWI may be impaired in areas of movement such as the anterior ribs and sternum. Visibility of skull vault infiltrations can be impaired because of the adjacent high signal of the normal brain. The visibility of skull base disease is impaired because of susceptibility effects.

Other causes for false-negative findings are low levels of bone marrow infiltration such as in smoldering multiple myeloma (when plasma cell infiltration fraction is less than background cell bone marrow cellularity) or when bone marrow hyperplasia results in diffuse increase in signal on high b-value images obscures the presence of metastases [2, 5] (Fig. 5). Relative bone marrow hypercellularity is observed in children and adolescents, chronic anemia, in smokers, chronic cardiac failure, in pregnancy

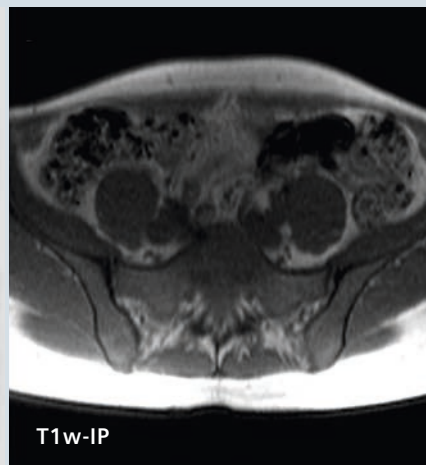
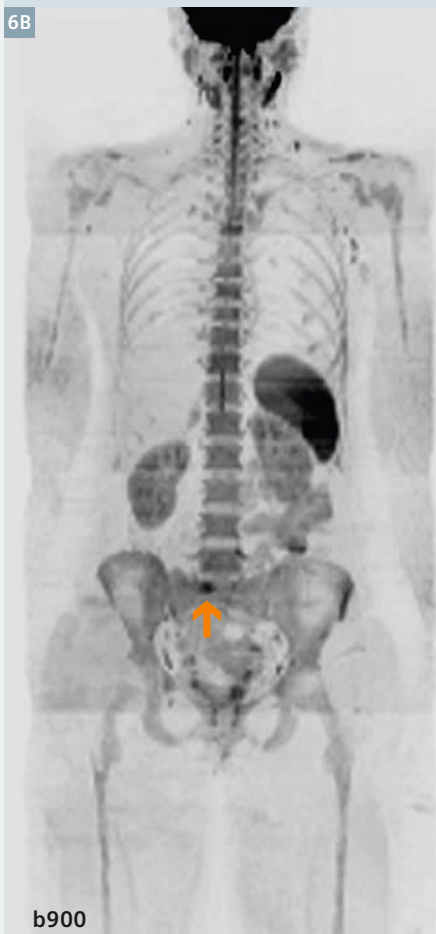


5 Bone marrow hyperplasia induced by G-CSF therapy obscuring metastases. 50-year-old woman with metastatic breast cancer before and after 3 cycles of erubulin chemotherapy with growth-colony stimulating factor (G-CSF) given to prevent neutropenia. b900 3D MIP (inverted scale) images. Image 5A shows multiple bone metastases (arrows). Image 5B after 3 cycles of chemotherapy shows increases in signal intensity of the bone marrow leading to the decreased visibility of the bone metastases. The splenic size has also increased. The increased signal intensity of the background bone marrow should not be misinterpreted as malignant progression.

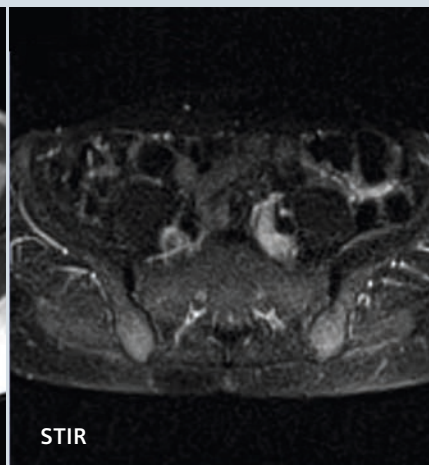


6 False positive whole body diffusion MRI.

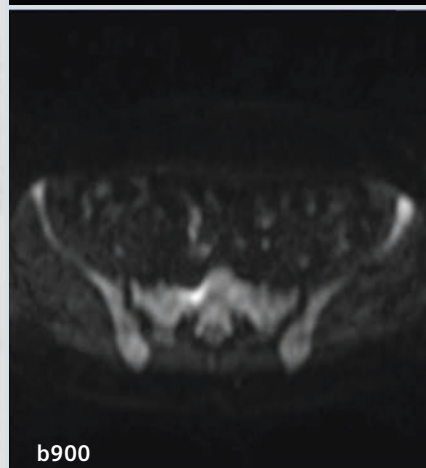
64-year-old female with breast cancer treated with right mastectomy, radiotherapy and chemotherapy. (6A) Bone scan shows increased uptake at L4/L5 – query metastases. (6B) Subsequent WB-DWI imaging 1 month later shows normal signal at L4/L5 with normal anatomic MRI images, but reveals a small focus of high signal intensity overlying the sacrum on b900 3D MIP (vertical arrow) and axial images. Corresponding anatomical T1w and STIR sequences show no focal abnormality within the sacrum; the high signal seen on b900 images is artifact from adjacent bowel. Note normal marrow signal on WB-DWI done eight months later (bottom right) with no development of metastases.



T1w-IP



STIR



b900



and in patients treated with hematopoietic growth factors such as granulocyte-colony stimulating factors (G-CSF).

Causes for false-positive findings include bone marrow edema caused by fractures, osteoarthritis, infection, bone infarcts, vertebral hemangiomas, isolated bone marrow islands and 'T2 shine through' – the latter observed in treated metastases. A variety of internal metallic (orthopedic) and silicone (breast) prostheses are routinely encountered in clinical practice. Magnetic field inhomogeneities secondary to metal and air interfaces will cause artifacts that cause false positive lesions (Fig. 6) and at the same time may obscure metastatic lesions in the adjacent bones. Many of these false-positive findings can be identified as not representing metastases by correlating the appearances of DW images with corresponding ADC maps and anatomical sequences [5].

Conclusions

WB-DWI is a contemporary imaging technique serving as an adjunct to conventional morphological whole body MRI, with high intrinsic sensitivity for detecting skeletal bone marrow metastases. However, there are several pitfalls that are encountered in routine clinical practice, the majority of which can be overcome by judicious interpretation of images in conjunction with standard anatomical sequences in light of relevant clinical knowledge.

References

- 1 Wu LM, Gu HY, Zheng J, et al. Diagnostic value of whole-body magnetic resonance imaging for bone metastases: a systematic review and meta-analysis. *J Magn Reson Imaging* 2011;34:128-135.
- 2 Padhani AR, Gogbashian A. Bony metastases: assessing response to therapy with whole-body diffusion MRI. *Cancer Imaging* 2011;11 Spec No A:S129-145.
- 3 Padhani AR. Diffusion magnetic resonance imaging in cancer patient management. *Semin Radiat Oncol* 2011;21:119-140.
- 4 Koh DM, Blackledge M, Padhani AR, et al. Whole-Body Diffusion-Weighted MRI: Tips, Tricks, and Pitfalls. *AJR Am J Roentgenol* 2012;199:252-262.
- 5 Padhani AR, Koh DM, Collins DJ. Whole-body diffusion-weighted MR imaging in cancer: current status and research directions. *Radiology* 2011;261:700-718.
- 6 Hwang S, Panicek DM. Magnetic resonance imaging of bone marrow in oncology, Part 1. *Skeletal Radiol* 2007;36:913-920.
- 7 Messiou C, Collins DJ, Morgan VA, Desouza NM. Optimising diffusion weighted MRI for imaging metastatic and myeloma bone disease and assessing reproducibility. *Eur Radiol* 2011;21:1713-1718.
- 8 Hillengass J, Bauerle T, Bartl R, et al. Diffusion-weighted imaging for non-invasive and quantitative monitoring of bone marrow infiltration in patients with monoclonal plasma cell disease: a comparative study with histology. *Br J Haematol* 2011;153:721-728.
- 9 Nonomura Y, Yasumoto M, Yoshimura R, et al. Relationship between bone marrow cellularity and apparent diffusion coefficient. *J Magn Reson Imaging* 2001;13:757-760.
- 10 Eiber M, Holzapfel K, Ganter C, et al. Whole-body MRI including diffusion-weighted imaging (DWI) for patients with recurring prostate cancer: Technical feasibility and assessment of lesion conspicuity in DWI. *J Magn Reson Imaging* 2011;33:1160-1170.



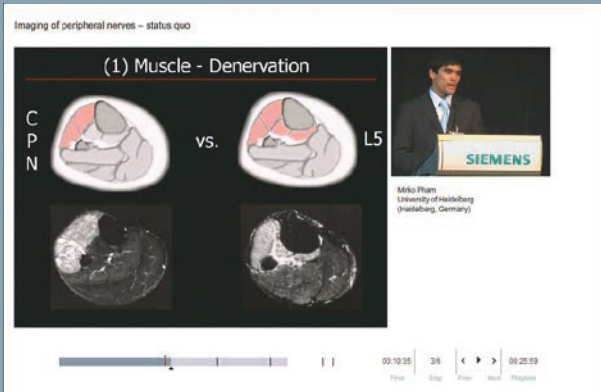
Contact

Professor Anwar R. Padhani,
MB BS, FRCP, FRCR
Paul Strickland Scanner Centre
Mount Vernon Cancer Centre
Rickmansworth Road
Northwood
Middlesex HA6 2RN
United Kingdom
Phone: +44 (0) 1923-844751
Fax: +44 (0) 1923-844600
anwar.padhani
@stricklandscanner.org.uk

Relevant clinical information at your fingertips

From technology to clinical applications, you will find all the latest news on Siemens MR at

www.siemens.com/magnetom-world



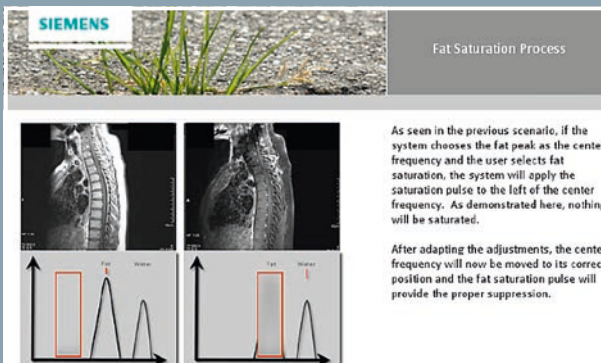
Don't miss the talks of international experts on Magnetic Resonance Imaging.

Go to
Clinical Corner > Clinical Talks



The centerpiece of the MAGNETOM World Internet platform consists of our users' clinical results. Here you will find case reports and clinical methods.

Go to
Clinical Corner > Case Studies



Just a mouse click away you will find application videos and useful tips allowing you to optimize your daily MR examinations.

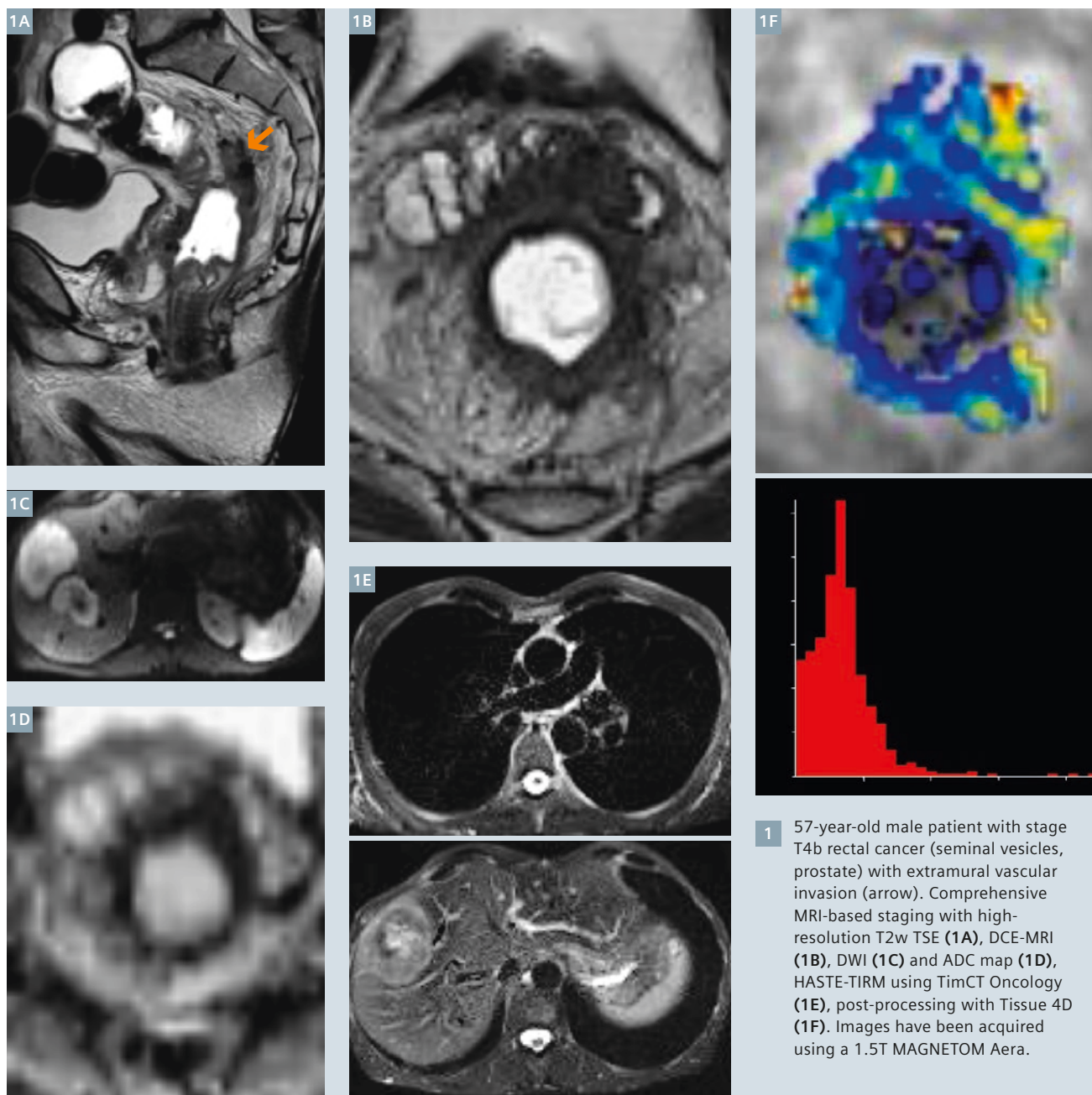
Go to
Clinical Corner > Application Tips

For the whole range of clinical MR information visit us at

www.siemens.com/magnetom-world

Comprehensive MRI-Based Staging of Rectal Cancer.

Beneficial Combination of Local High-Resolution Imaging and a Moving-Table Platform for Simultaneous Detection of Metastasis



**Arnd-Oliver Schäfer;
Mathias Langer**

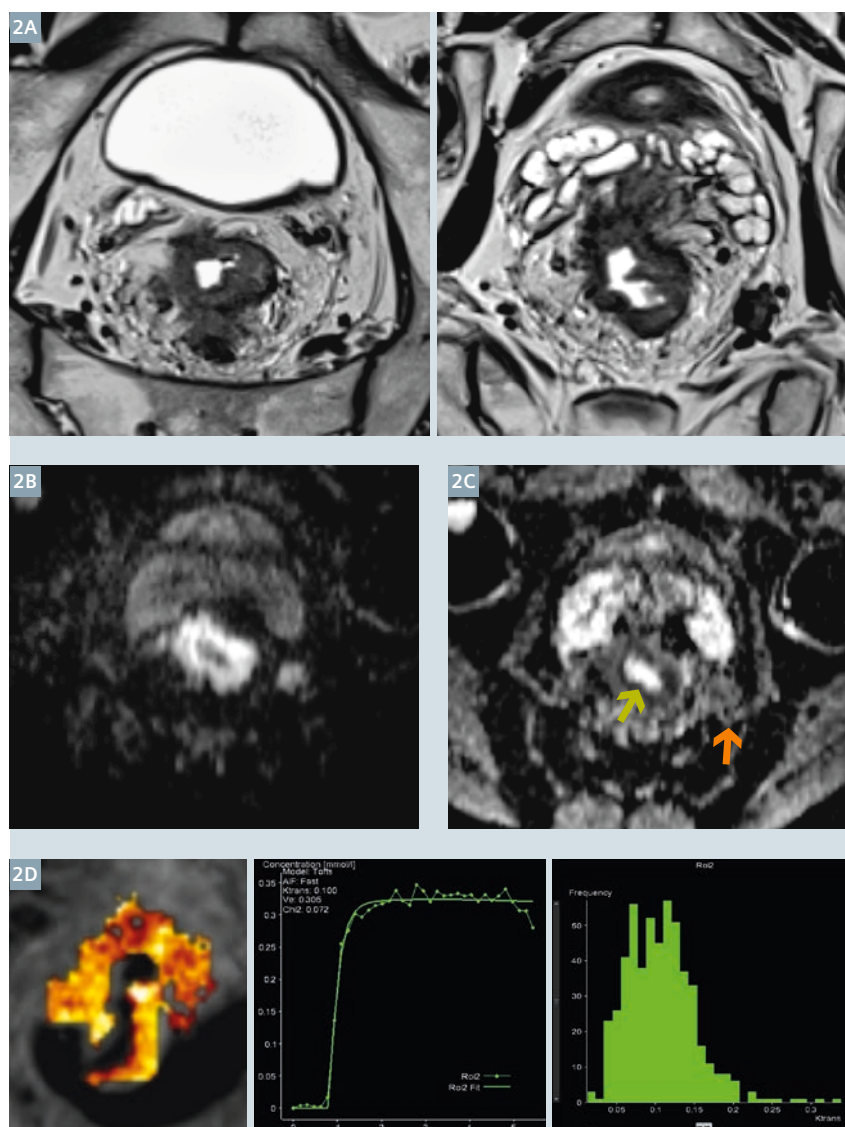
Freiburg University Hospital, Department of Diagnostic and Therapeutic Radiology, Freiburg, Germany

Although local tumor control is already established for rectal cancer due to multimodal therapy, its inherent tendency to metastasize still represents an unsolved problem and poses a major challenge for upcoming diagnostic and therapeutic strategies. Whilst standard long-course neoadjuvant chemoradiation has been shown to reduce the risk of local recurrence, nevertheless it demonstrates no substantial influence on the biological behavior of potential metastasis. In this context, the study by Ayez et al. [1] recommended the restaging of locally advanced rectal cancer by chest and abdominal CT after completion of long-course neoadjuvant therapy, given that additional findings may alter the treatment strategy.

In this setting, comprehensive staging algorithms using a single diagnostic modality would be highly reasonable. Specialized magnetic resonance imaging (MRI) is known to be the pivotal staging tool for locally advanced rectal cancer and particularly addresses the extent of mesorectal infiltration and the status of circumferential resection margin, which is known to be the most important prognostic indicator [2]. Whole-body MRI using a continuously moving patient table like in TimCT Oncology was originally developed at our institution in 2005 and clinically established in 2006 [3,4]. The Sliding Multislice application covers thorax, abdomen, and pelvis for staging of distant spread, especially to lungs, liver, nodes, and bone. Moving table MRI with Sliding Multislice has proved to greatly benefit scan efficiency and diagnostic accuracy when combined with local high-resolution rectal

cancer staging. With the adoption of this exciting technique, true comprehensive MRI-staging of rectal cancer is now possible and has gained substantial acceptance amongst colorectal surgeons, radiation oncologists, and oncologists. Technological advances enabled further diversification of our imaging protocol adding pelvic and upper abdomen diffusion-weighted imaging (DWI) and local

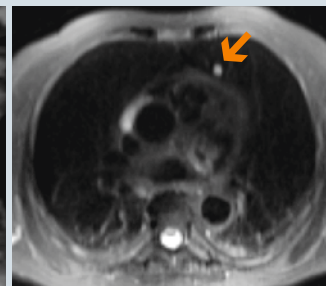
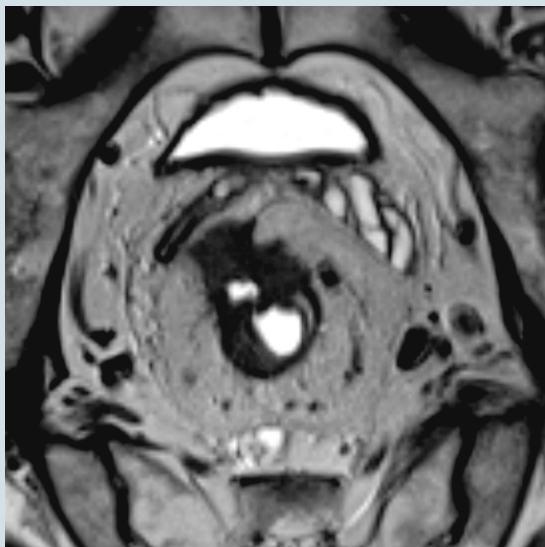
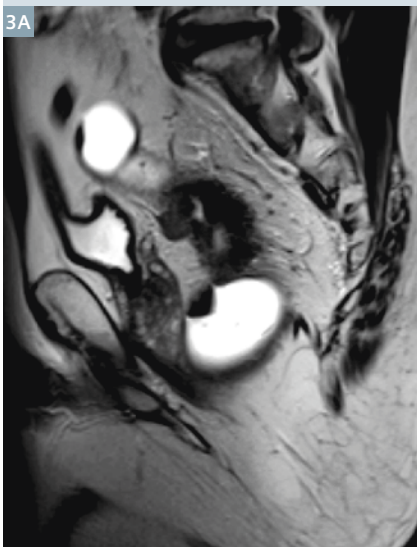
dynamic contrast-enhanced (DCE)-MRI using the Tissue 4D platform for post-processing. To better characterize early response to neoadjuvant chemoradiation and to a greater extent predict tumor aggressiveness would require multiparametric MRI which, in our opinion, will be the next logical step towards future-oriented comprehensive MRI-based staging of rectal cancer.



2 56-year-old male with stage T4a rectal cancer. Multiparametric imaging at 1.5T MAGNETOM Aera. (2A) Morphological overview, (2B) Diffusion-weighted imaging with a b-value of 1000 s/mm². (2C) ADC tumor $0,742 \times 10^{-3}$ mm²/s (green arrow) and node $0,692 \times 10^{-3}$ mm²/s (orange arrow). (2D) Post-processing with syngo Tissue 4D for color coded parametric maps, curves, and histograms.

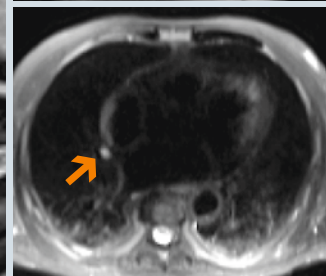
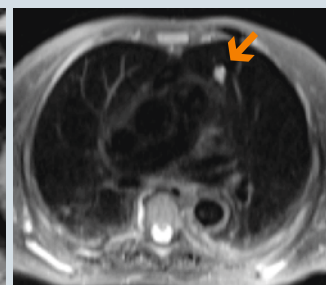
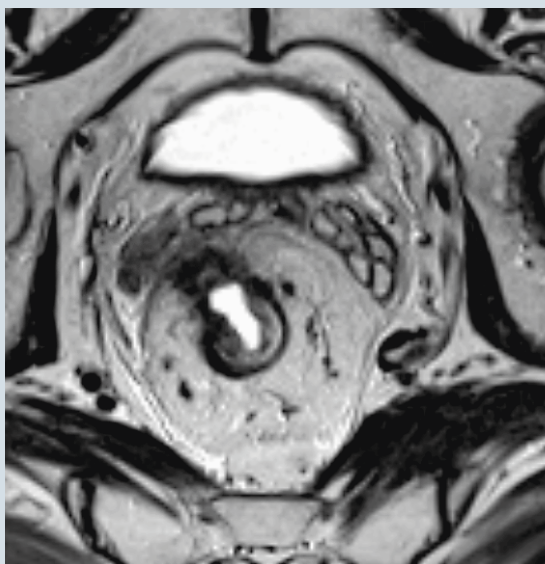
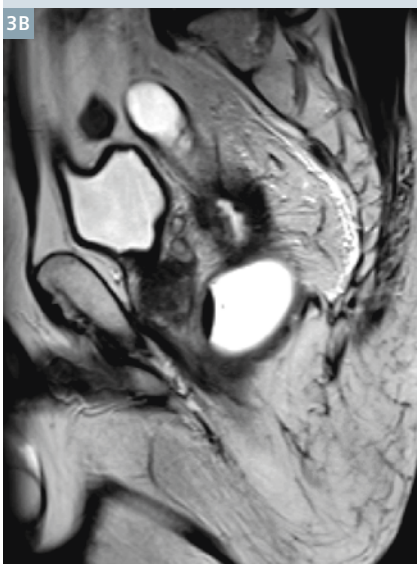
Baseline

3A



Control

3B



- 3** 73-year-old male with advanced rectal cancer. MRI before (**3A**) and after (**3B**) neoadjuvant chemoradiation. ypT3N2a(5/14), regression grade 3 (> 50% vital tumor cells) progression of lung metastases (arrows). Images have been acquired using a 1.5T MAGNETOM Avanto.

References

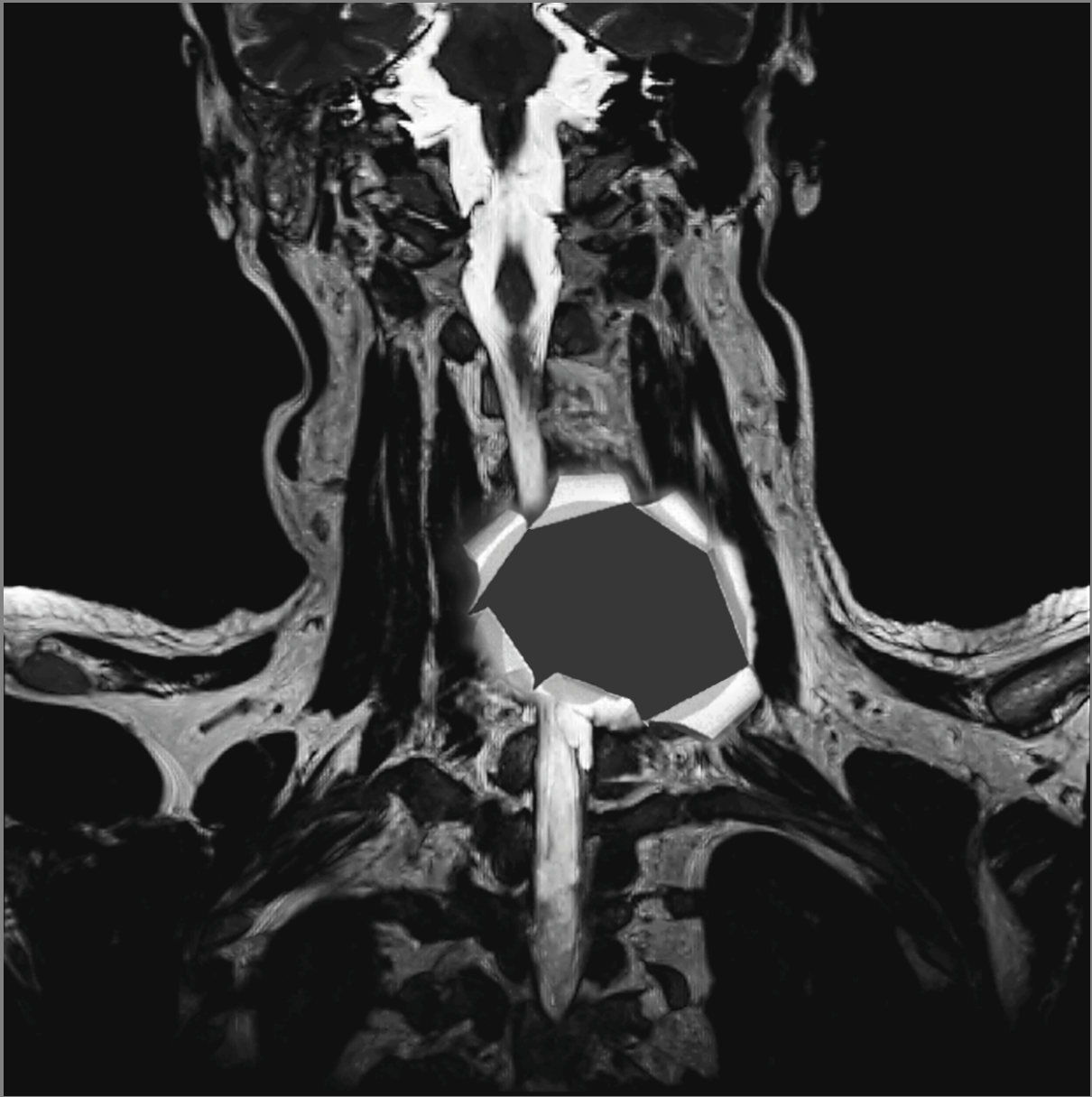
- 1 Ayez N, Alberda WJ, Burger JW et al. Is restaging with chest and abdominal CT scan after neoadjuvant chemoradiotherapy for locally advanced rectal cancer necessary? *Ann Surg Oncol* 2013; 20:155-160.
- 2 Heald RJ. A new solution to some old problems: transanal TME. *Tech Coloproctol* 2013; 17:257-258.
- 3 Fautz HP, Kannengießer SAR. Sliding multislice (SMS): a new technique for minimum FOV usage in axial continuously moving table acquisitions. *Magn Reson Med* 2006; 55:363-370.
- 4 Schaefer AO, Langer M, Baumann T. Continuously moving table MRI in oncology. *Fortschr Röntgenstr* 2010; 182:954-964.



Contact

Professor Arnd-Oliver Schäfer, M.D.
 Freiburg University Hospital
 Department of Diagnostic
 and Therapeutic Radiology
 Hugstetter Straße 55
 D-79106 Freiburg
 Germany
 arnd-oliver.schaefer
 @uniklinik-freiburg.de

Missing information?



To make sure you have all the information you need, register for our free monthly newsletter on clinical MRI information. Check out case reports from MAGNETOM users around the world and stay up-to-date with Siemens software applications.

Register at
www.siemens.com/magnetom-world
Go to
[Publications > Subscriptions](#)

Tissue 4D on syngo.via

Anja Fernandez Carmona; Radim Chrastek

Siemens Healthcare, Erlangen, Germany

Introduction

The Tissue 4D workflow facilitates the detection of tumors in organs, including the liver and prostate. It is a *syngo.via* workflow for reading and post-processing of dynamic contrast-enhanced 3D datasets. Tissue 4D describes the exchange of contrast agents between blood and tissue.

The MR Tissue 4D workflow provides two methods of evaluation:

1) A quantitative method following the Tofts model [1].

The Tofts model is based on the following parameters:

- K^{trans} (transfer constant)
- V_e (extra-vascular extra-cellular volume fraction)
- K_{ep} (reflux constant)

2) A qualitative evaluation method to retrieve the following parameters:

- **In** (Wash-in: enhancement in the tissue due to contrast uptake in a defined time interval)
- **Out** (Wash-out of contrast agent in a defined time interval)
- **TTP** (Time-to-Peak: time until the contrast enhancement reaches the highest concentration and wash-out starts)
- **AT** (Arrival time: time point when contrast enhancement starts)
- **PEI** (Positive Enhancement Integral: Value of concentration when the contrast enhancement reaches its highest concentration and wash-out starts)
- **IAUC** (initial Area Under Curve in 60 seconds)

Precondition and preparation

To evaluate and read data with the Tissue 4D workflow, the following series are required or recommended:

- Dynamic contrast-enhanced images with fixed flip angle (required)
- Pre-contrast series with variable flip angle to calculate the T1-map (recommended)
- Corresponding morphological images (recommended)

To start the evaluation, the images need to be assigned to a specific workflow template.

The workflow template offers a sequence of pre-configured workflow steps.

The workflow template can be selected according to the anatomical region.

Currently, there are two options for opening the image data:

- Tissue 4D only
- Prostate with integrated Tissue 4D

Post-processing steps can be highly automated if the steps have been properly pre-configured. To do so you have to be locked in as clinical administrator.

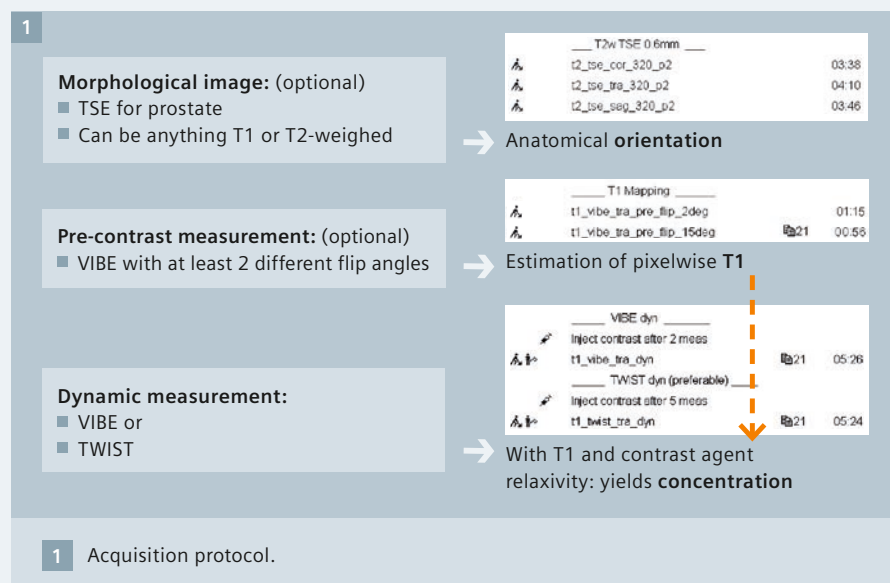
MR Tissue4D Analysis

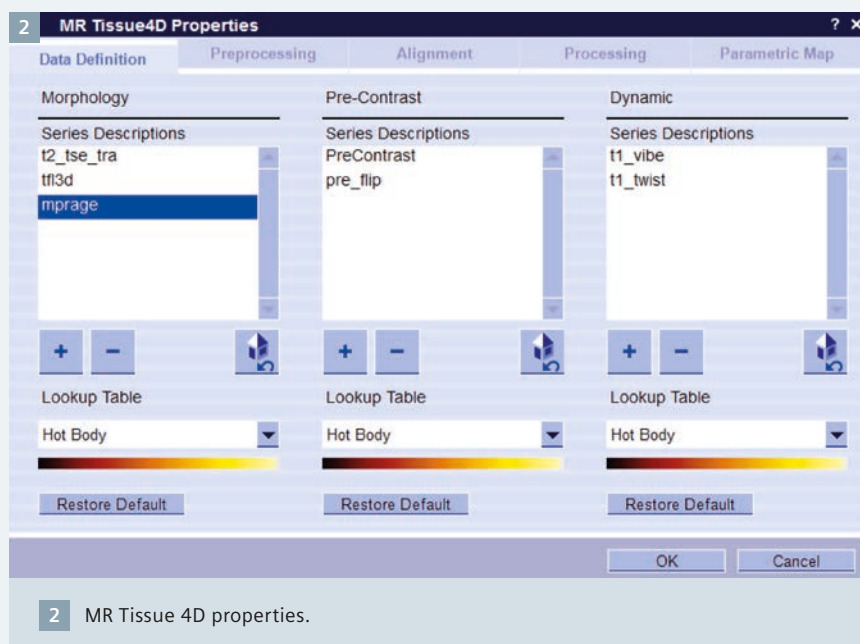
For the initial configuration open the Tissue 4D workflow with data in 'read only' mode. Once the case is opened, select the wrench icon in the workflow area for the Tissue 4D properties.

The configuration dialog 'Data Definition' allows to specify a series description for all data types, i.e. morphology, pre-contrast and dynamic series. All series that contain the given string are considered for automated case preparation. If there is more than one matching series for a data type, the latest series is used first.

Hint: The more precise the data type selection string is defined, the potentially shorter the case preparation time. This is because the case preparation is applied to all matching series, although the latest series is presented first.

After a reassignment of the Tissue 4D workflow the configuration settings are applied.





2 MR Tissue 4D properties.

An advanced functionality of Tissue 4D is automated alignment of data types, configurable in the 'Preprocessing' and 'Alignment' dialog. Automatically selected reference time phase of the dynamic data type serves as a reference for all alignment algorithms. For all three data types, there is an option 'None'. The option deactivates the alignment for the given data types.

All alignment algorithms, including motion correction for the dynamic data types, are based on an elastic registration. This kind of registration provides transformation for each individual pixel. The advantage of the approach is that local changes, e.g. due to breathing, can be mapped correctly without having to correct organ or bone positions not affected by the local motion. Generally, the registration provides a transformation of one data type to the other, so that the image pixels are displayed in the same geometrical position for both data sets. The image pixel values are interpolated if they do not match the grid of the original image. The 'Alignment' configuration dialog serves for expert settings and it is not recommended to change these configuration values.

'Preprocessing' allows the choice between two pharmacokinetic models: 'Qualitative' or 'Tofts'. The

latter requires the type of the Arterial Input Function (AIF), see below. Since the automated case preparation might take long for entire 3D datasets, the calculation is constrained to a 'volume-of-interest' (VOI). The VOI is defined by the center and radius for each direction, i.e. x, y, z. The center is given by the percentage of the 3D volume size. The default values are 50% for all three directions, i.e. the x, y, and z coordinates are exactly in the middle of the 3D volume. The radius is also given by the percentage of the 3D volume size. The smaller the VOI, the potentially faster the pharmacokinetic model calculation, especially for the Tofts model.

Evaluation and reading

Once the Tissue 4D properties have been configured, the case can be assigned and opened with the specific workflow template. Here is what you will see:

Motion correction step

You can use this step to verify the automatic alignment of the dynamic data set to a defined reference volume.

Time point slider



The time point slider visualizes the available time points in the dynamic data set. The current reference time point (reference volume) for motion correction is indicated by a small blue triangle.

Selecting a new reference time point:



In the **Case Navigator**, click the slider and move it to the required time point. Click this icon to confirm the new reference time point.

The blue triangle jumps to the new reference time point and the display in the image segments is updated accordingly.

Hint: Before you can change the reference time point you have to turn off motion correction.

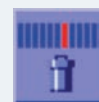
The Motion Correction step is used to align the dynamic dataset to a defined reference volume.



In the **Case Navigator**, click this icon to turn the motion correction on or off.

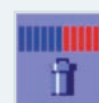
Motion correction is applied in all other volumes of the dynamic data set according to the reference time point.

You can delete time points from the current data set if, for example, the quality is not sufficient for the evaluation.



In the **Case Navigator**, click the slider and move it to the required time point. Click this icon to delete a specific time point.

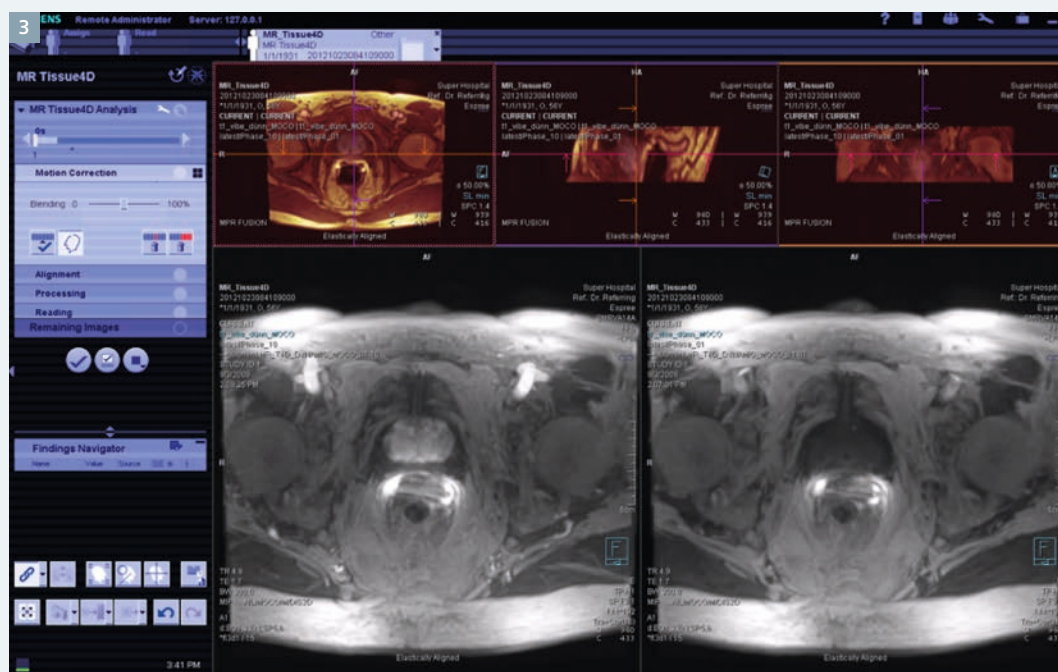
or



Click this icon to delete all time points after the selected time point (to the right side).

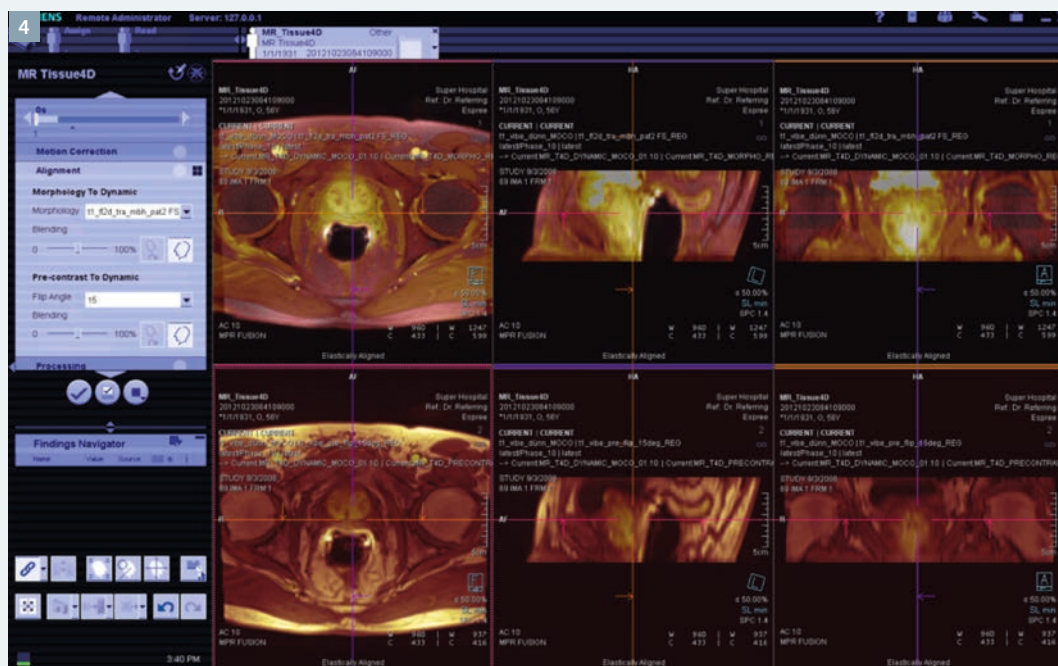
Alignment step

Here you see only the configured and available series. On a single monitor configuration the upper part shows the morphology aligned to the dynamic and the lower part the pre-contrast to the dynamic series.



- 3 The top row shows the fusion of current phase and reference phase. The images are displayed using the multi-planar reconstruction (MPR) volume rendering technique. If you navigate to the reference phase, only this reference phase is shown, without fusion. The bottom row shows the reference phase (left) and the current phase (right) using mean intensity projection (MIP) volume rendering technique.

In most cases the automatic alignment works fine and you can proceed directly to the next step. If, however, you are not satisfied with the alignment you can change it by using the visual alignment tool in the upper left corner menu.



- 4 Alignment



5 Alignment menu.

To verify the correctness of the alignment you can use the blending mode. Move the slider to the left and right side.



Before you can change the alignment you have to turn motion correction off.



Moco on



Moco off

There are different alignment modes:

- Automatic rigid: the entire volume is transformed. The transformation obtained by the registration algorithm is the same for all pixels. No local deformation can be compensated (such as breathing)
- Visual: you can shift and rotate the volumes
- Elastic: can compensate local deformations



6 Processing step qualitative.



7 Processing step quantitative.

Processing step

Here you can modify the pharmacokinetic modeling. You can change between Tofts and qualitative model, and also define the evaluation volume.

The qualitative model matches three lines to the measured concentration curve for each voxel within the VOI. It does not require any parameters. The first line fits the baseline phase, i.e. before contrast agent arrival. The second line fits the wash-in phase, i.e. it displays the enhancement in the tissue due to contrast

uptake in a defined time interval t . The third line fits the wash-out phase. The graph in the top right-hand corner shows the mean concentration curve for the entire VOI, together with the correspondingly fitted three lines.

The Tofts model matches a mathematical model defined by [1] to the measured concentration curves for each voxel within the VOI. Also for this model, a graph with the mean curve for the entire VOI is displayed in the top right-hand corner.

The selectable parameter for the Tofts modeling, the AIF, is based on mathematical simulation, slow [4], intermediate [3], and fast [2]. If you are not sure which AIF to use, the χ^2 parameter might help. The χ^2 parameter is an error measure of the fit. The smaller the parameter, the better the fit.

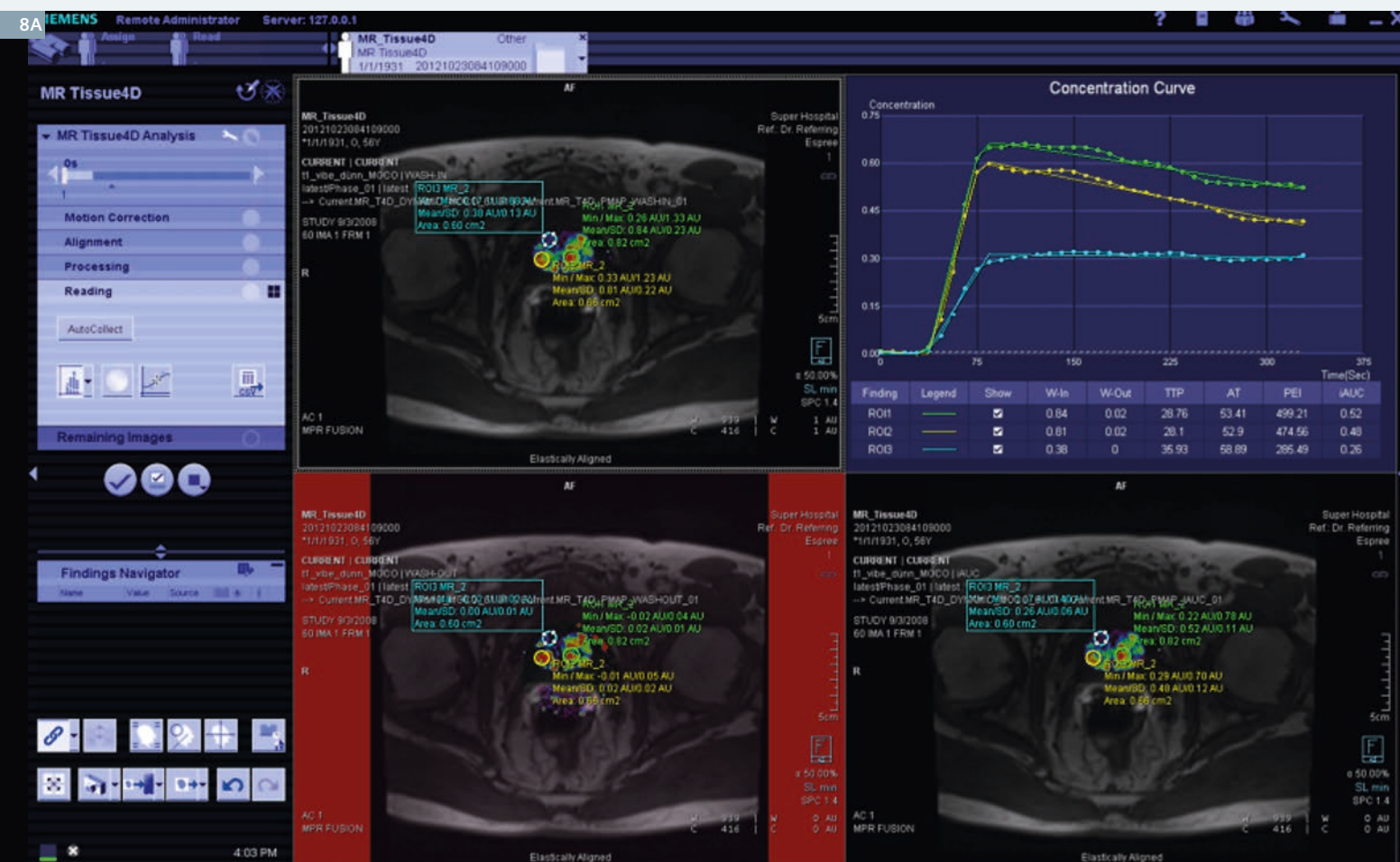
Recommendation: keep the size of the VOI as small as possible. The larger the VOI, the potentially longer the pharmacokinetic model calculation, especially for the Tofts model.

Reading step

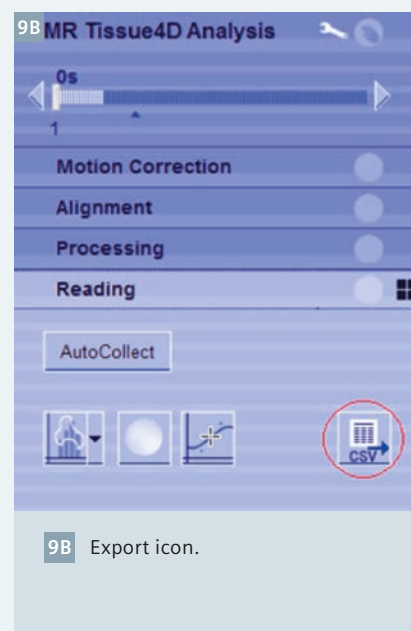
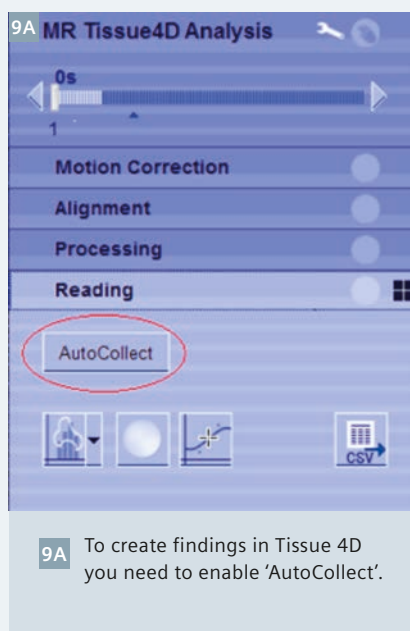
The last step enables you to read the resulting maps and create findings for your report.

Here are different Tissue 4D reading tools available to evaluate the mean and the standard deviation in a selected area.

In the upper right segment these curves are displayed.



8A Measurement icons.



To create findings in Tissue 4D workflow you need to enable the 'AutoCollect' button. Manual findings creation is only possible via snapshots.

Export of results: You can export reading results as text file (csv-files). The export icon (Fig. 9B) is context sensitive and exports the results of the selected segment.

Summary

This article describes the current version of the Tissue 4D for DCE evaluation. Case preparation can be highly automatized, allowing you to concentrate on the reading. The automatic case preparation takes care of the selection of the data types, their alignment to the reference phase of the dynamic data type and pharmacokinetic model calcula-

tion. You only have to verify the results of the automatic case preparation. Once done, you can immediately start reading. The results can be then exported to csv format. All documented findings, i. e. collected in the Findings Navigator, are automatically stored as DICOM Structured Report once the workflow has been completed.

References

- 1 Tofts P. T1-weighted DCE Imaging Concepts: Modelling, Acquisition and Analysis. MAGNETOM Flash 2010;3:31-39.
- 2 Orton MR, d'Arcy JA, Walker-Samuel S, Hawkes DJ, Atkinson D, Collins DJ, Leach MO. Phys Med Biol. 2008 Mar 7;53(5):1225-39. Computationally efficient vascular input function models for quantitative kinetic modelling using DCE-MRI.
- 3 Parker GJ, Roberts C, Macdonald A, Buonaccorsi GA, Cheung S, Buckley DL, Jackson A, Watson Y, Davies K, Jayson GC. Magn Reson Med. 2006 Nov;56(5):993-1000. Experimentally-derived functional form for a population-averaged hightemporal-resolution arterial input function for dynamic contrast-enhanced MRI.
- 4 Weinmann H, Laniado M, Mutzel W. Physiol Chem Phys Med NMR. 1984; 6(2):167-72. Pharmacokinetics of GdDTPA/dimeglumine after intravenous injection into healthy volunteers.

Contact

Anja Fernandez Carmona
Siemens Healthcare
IM MR R&D SW VIA PM
91050 Erlangen
Germany
Phone: +49 (9131) 84-3566
anja.fernandez_carmona@siemens.com

Case Report: Functional, Volumetric, Treatment Response Assessment Using MR OncoTreat

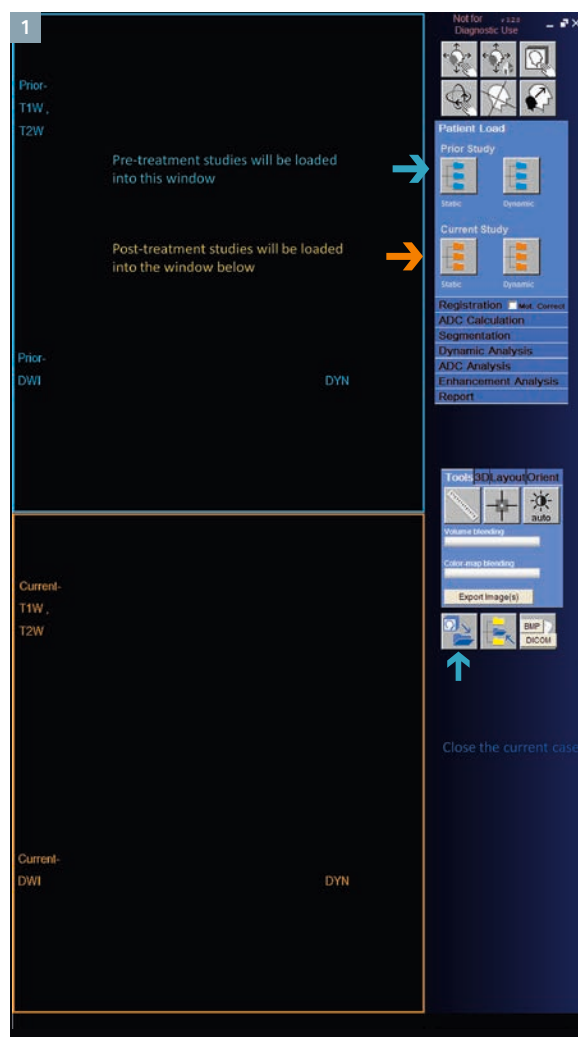
Susanne Bonekamp; Ihab R. Kamel

The Russell H. Morgan Department of Radiology and Radiological Science, The Johns Hopkins Hospital, Baltimore, MD, USA

Introduction

Hepatocellular carcinoma (HCC) is one of the most common malignancies worldwide and is associated with a very low survival rate [1]. Because the majority of HCC lesions are diagnosed at an advanced stage, few patients qualify for surgical resection or liver transplantation [2]. Loco-regional treatment methods, most commonly transarterial chemoembolization (TACE), are considered the standard of care in patients with unresectable HCC [3, 4]. Response to treatment is often assessed using cross-sectional imaging. Current guidelines include EASL (European Association for the Study of Liver Disease) and modified RECIST (Response Evaluation Criteria in Solid Tumors). Both metrics rely on the measurement of viable tumor burden in a single axial plane [5, 6]. However, assessment of a single axial slice can be misleading and may have low reproducibility. Furthermore, residual enhancement assessed by contrast-enhanced MRI or CT can be difficult to evaluate owing to the presence of changes in signal intensity (hyperintensity on unenhanced T1-weighted images) related to a combination of iodized oil injection and hemorrhagic necrosis.

Several recent publications have highlighted the advantage of volumetric assessment of tumor anatomy and function as a method of response assessment. Functional volumetric assessment of diffusion-weighted MRI (DWI) using apparent diffusion coefficient (ADC) maps and post-contrast-enhancement MRI have been successfully applied in the brain and liver [7, 8]. Using a prototype software



Overview of MR OncoTreat. First patient DICOM data is loaded. The pre-treatment data is loaded into the window outlined in blue, while the follow-up MRI data is loaded into the window outlined in orange. After loading patient data an automatic data classification is done after loading which classifies data into six categories: T1W, T2W, DWI, ADC, DIFF and OTHER based on the protocol settings stored in the DICOM header. These settings can be manually overwritten.

(MR OncoTreat*; Fig. 1) developed by Siemens Corporation; Corporate Technology, USA and Siemens Healthcare, Erlangen, Germany we have published several recent manuscripts that outline the feasibility of a volumetric, functional assessment of treatment response in patients with primary

and metastatic liver cancer [8-13]. This case report outlines the functional, volumetric analysis of response to TACE in a patient with HCC.

* Work in progress: The product is still under development and not commercially available yet. Its future availability cannot be ensured.

Patient history

The patient is a 61-year-old male with a history of hepatitis B, liver cirrhosis, and hepatocellular carcinoma. After diagnosis of a large lesion in the liver (14 cm in diameter) on CT imaging, he underwent one session of hepatic artery chemoembolization to the right lobe of the liver. MR imaging was performed one day before TACE to more accurately assess the lesion. Follow-up MRI was done one month after TACE.

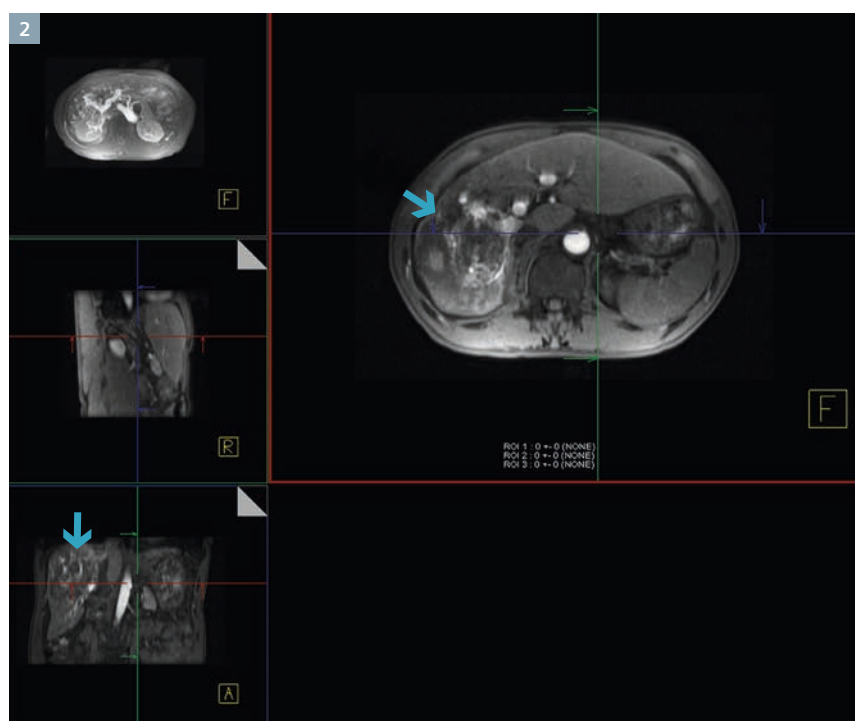
Sequence details

All images have been acquired on a 1.5T MAGNETOM Avanto (Siemens Healthcare, Erlangen, Germany). The patient underwent our standardized clinical imaging protocol. Which included breath-hold diffusion-weighted echo planar images (matrix, 128×128 ; slice thickness 8 mm; interslice gap, 2 mm; b-value, 0 s/mm^2 , 750 s/mm^2 ; repetition time (TR) 3000 ms; echo time (TE) 69 ms; received bandwidth 64 kHz) as well as breath-hold unenhanced and contrast-enhanced (0.1 mmol/kg intravenous gadobenate dimeglumine; Multihance; Bracco Diagnostics, Princeton, NJ, USA) T1-weighted three-dimensional fat suppressed spoiled gradient-echo images (field-of-view 320–400 mm; matrix 192×160 ; slice thickness 2.5 mm; TR 5.77 ms; TE 2.77 ms; received bandwidth 64 kHz; flip angle 10°) in the hepatic arterial phase (AE) (20 s), and portal venous phase (VE) (70 s).

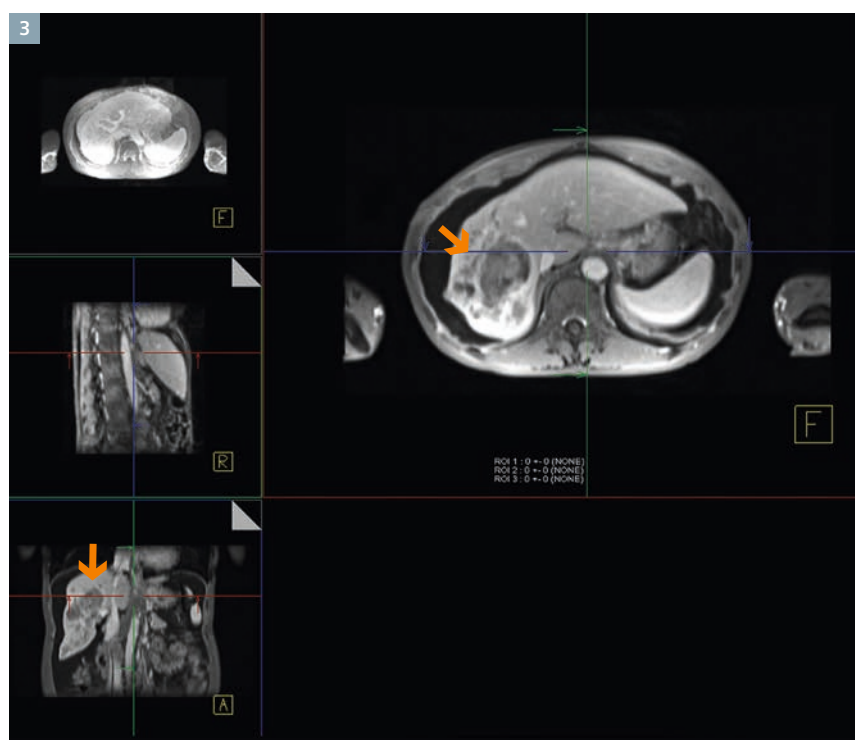
Volumetric functional MRI response

Image analysis was performed by an MRI researcher (S.B.) with 8 years experience in MR imaging using proprietary, non-FDA approved software, MR OncoTreat (Siemens Healthcare, Erlangen, Germany). A single, treated HCC index lesion was selected as the representative index lesion for the patient. Figure 2 shows the arterial phase images of the lesion (arrow) before treatment. Figure 3 shows the same lesion after treatment.

Lesion segmentation is shown in figure 4 (pre-treatment) and figure 5

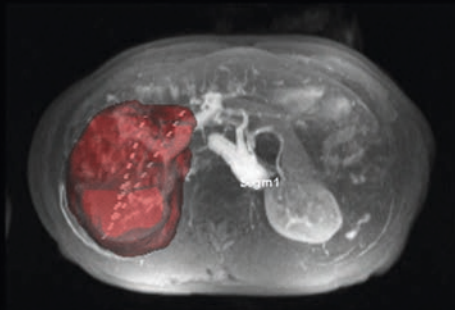


2 Arterial phase images of a liver with a large heterogeneously enhancing HCC lesion (arrows) in a 61-year-old male with a history of hepatitis B before loco-regional therapy.



3 Arterial phase images of a liver with a large heterogeneously enhancing HCC lesion (arrows) of the same patient after loco-regional therapy.

4

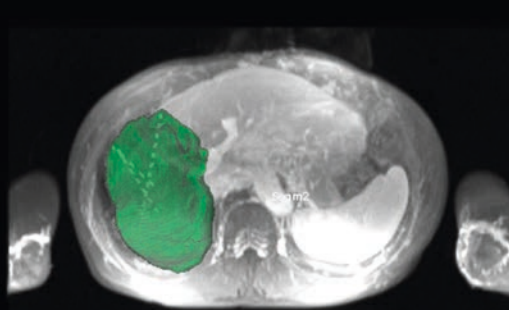


Total Volume : 547.5 0 cm3
Total Surface : 32.3 0 cm2
Total Diameter : 137.2 0 mm
Total RECIST : 115.1 0 mm

F

- 4 Segmentation of the HCC lesion before treatment performed using seed placement and 'Random Walker', a semi-automatic 3D segmentation technique.

5

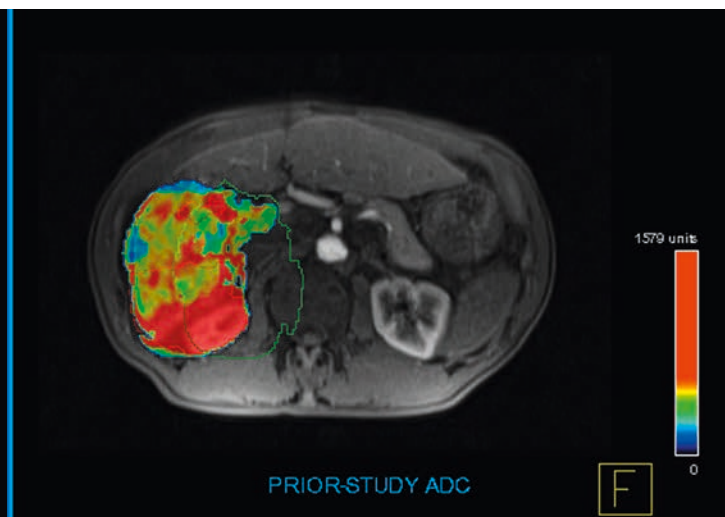


Total Volume : 0 420.7 cm3
Total Surface : 0 26 cm2
Total Diameter : 0 149.5 mm
Total RECIST : 0 105.7 mm

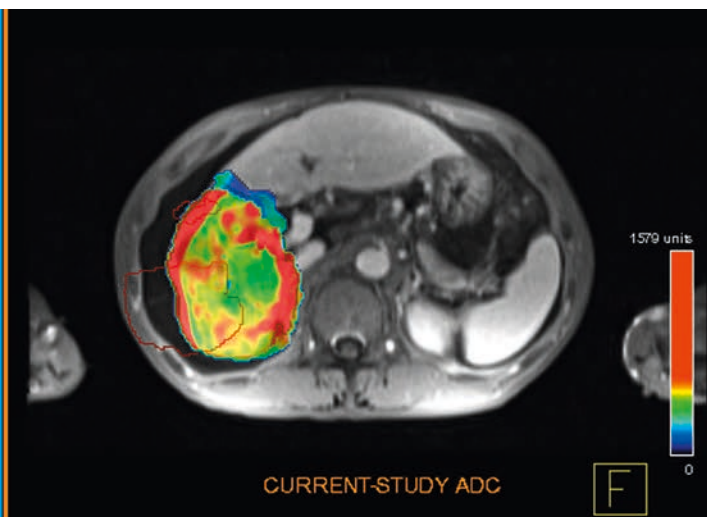
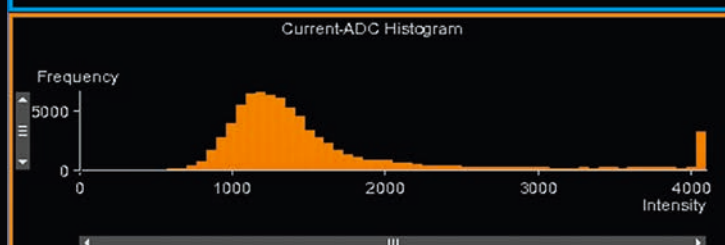
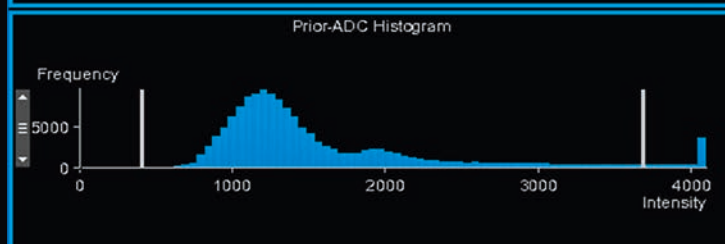
F

- 5 Segmentation of the HCC lesion after treatment performed using seed placement and 'Random Walker', a semi-automatic 3D segmentation technique. No co-registration of the HCC lesion was performed due to the change in size and structure.

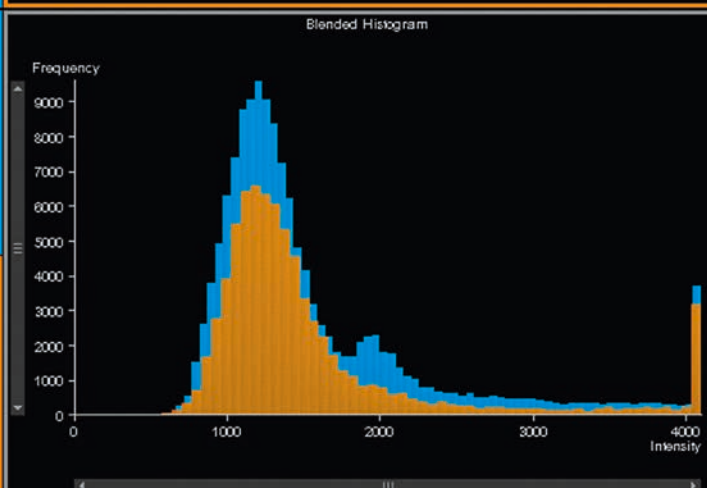
6



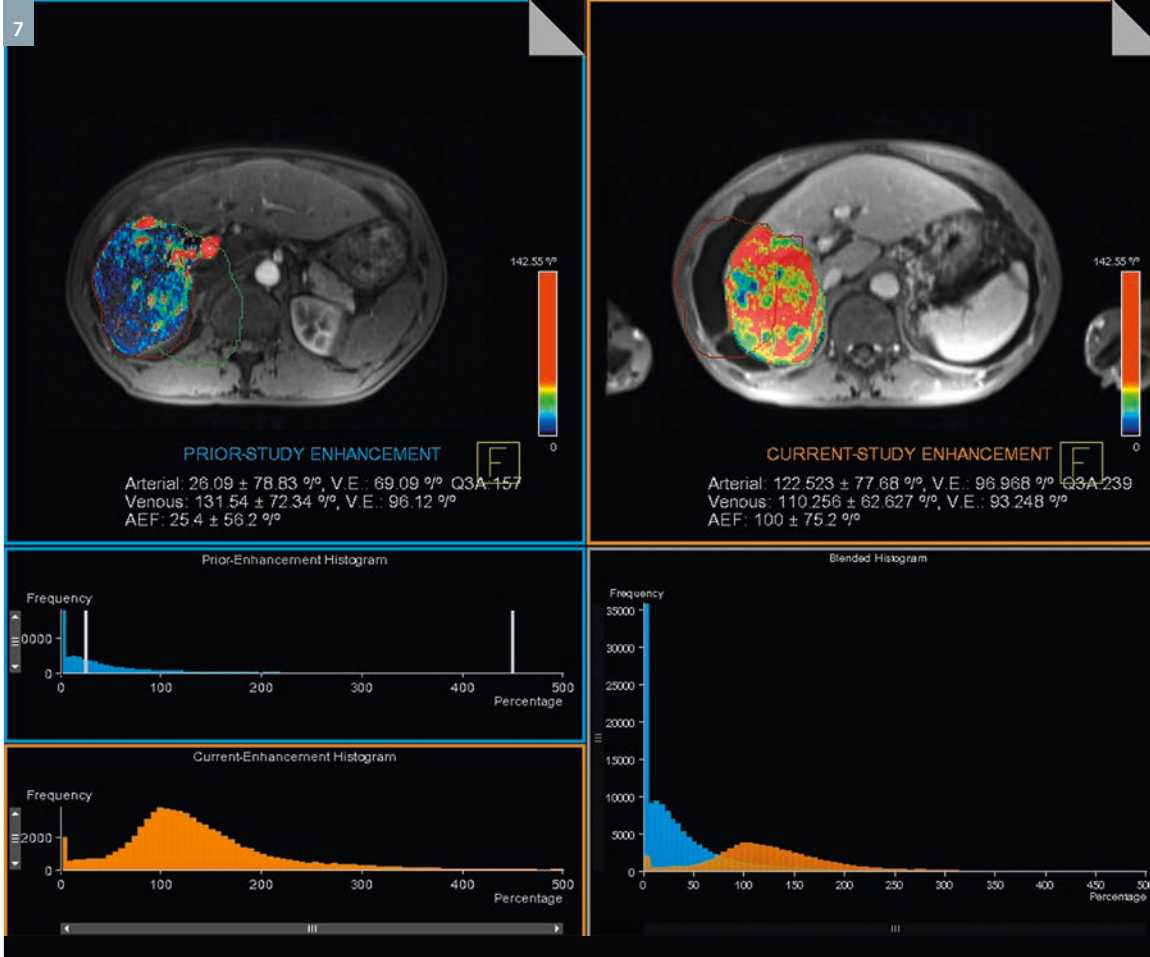
ADC: 1320 ± 760.536 [0 , 4095] units



ADC: 1318 ± 780.47 [81 , 4095] units

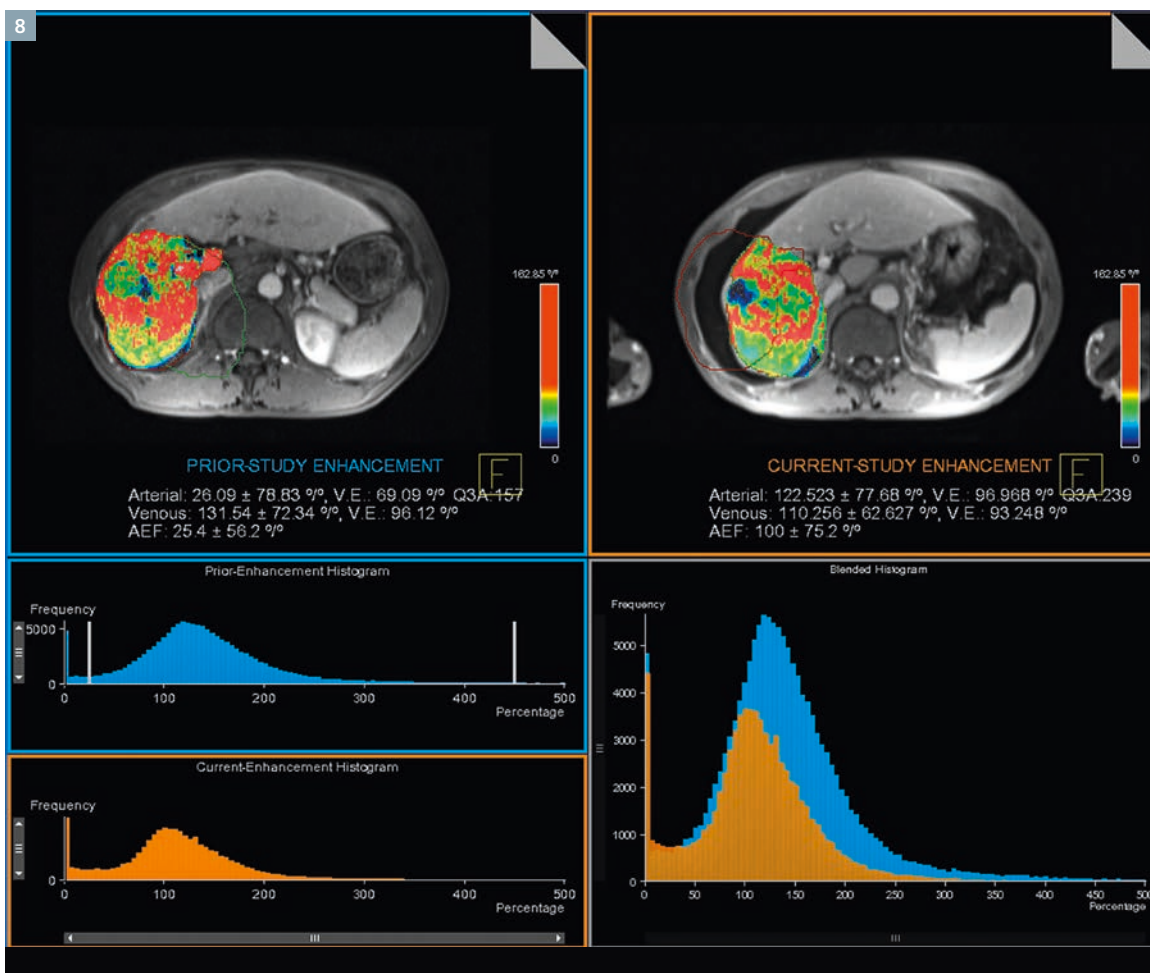


- 6 Comparison of the ADC values before and after TACE within the entire segmented tumor volume. The upper left window and the blue histogram show the heterogeneous distribution of ADC values before treatment, the upper right window and the orange histogram show the distribution of ADC values after treatment. The window in the lower left shows an overlay of the pre- and post-treatment ADC values and their distribution, allowing for easy visual assessment of treatment induced changes in ADC.



7

Comparison of the arterial enhancement (AE) values before and after TACE within the entire segmented tumor volume. The upper left window and the blue histogram show the heterogeneous distribution of AE values before treatment, the upper right window and the orange histogram show the distribution of AE values after treatment. The window in the lower left shows an overlay of the pre- and post-treatment AE values and their distribution, allowing for easy visual assessment of treatment induced changes in AE.



8

Comparison of the portal venous enhancement (VE) values before and after TACE within the entire segmented tumor volume. The upper left window and the blue histogram show the heterogeneous distribution of VE values before treatment, the upper right window and the orange histogram show the distribution of VE values after treatment. The window in the lower left shows an overlay of the pre- and post-treatment VE values and their distribution, allowing for easy visual assessment of treatment induced changes in VE.

(post-treatment). The software automatically generated tumor diameter, tumor volume, volumetric ADC and volumetric enhancement in the arterial (AE) and portal venous phase (VE).

ADC maps were reconstructed using a monoexponential fit between two b-values of 0 and 750 s/mm². Figure 6 depicts a comparison of the ADC values of the pre-treatment lesion (segment 1), along with the pre-treatment ADC histogram in blue, and the post-treatment lesion (segment 2), with the post-treatment ADC histogram in orange.

For the assessment of treatment response the percent change in volumetric tumor ADC at follow-up compared with baseline values can be calculated using the formula $\{(ADC_{post} - ADC_{pre})/ADC_{pre}\} \times 100$, where ADC_{pre} is the mean baseline volumetric ADC value and ADC_{post} is the mean follow up volumetric ADC value.

Enhancement in the portal venous phase was calculated by subtracting the native phase signal intensity from the venous phase signal intensity multiplied by 100 to obtain percentage change. Similar to the ADC results, figures 7 (AE) and 8 (VE) show a comparison of the pre-treatment enhancement values (segment 1, blue histogram) compared to the post-treatment enhancement values (segment 2, orange histogram).

Again, for the assessment of response to treatment the percent change in volumetric tumor AE or VE at follow up compared with baseline values can be calculated using the formula $\{(E_{post} - E_{pre})/E_{pre}\} \times 100$, where E_{pre} represents the mean baseline volumetric enhancement value and E_{post} represents the mean 3–4 weeks follow up volumetric enhancement value.

Diagnosis

Figures 4–8 show the large, heterogeneously enhancing HCC lesion before and after treatment. ADC values did not change significantly after TACE (1.320×10^{-3} mm²/s to 1.318×10^{-3} mm²/s, fig. 6). Enhancement values in the hepatic arterial phase were highly variable with

a standard deviation of 79% and increased after treatment (26.09% to 122.52%, fig. 7), while portal venous enhancement was also highly variable (standard deviation of 72%) and showed a slight decrease after TACE (131.54% to 110.26%, fig. 8). Together these functional parameters indicate that the lesion did not respond to treatment. The patient subsequently underwent treatment with doxorubicin eluting microspheres (DEB-TACE) which resulted in a more favorable outcome than the initial TACE.

Conclusion

The case shows how functional, volumetric analysis of MR imaging data using MR Oncotreat can assist diagnostic and interventional radiologist in the assessment of treatment response and planning of follow-up treatment.

Acknowledgement

We would like to thank Atilla Kiraly, Mehmet Akif Gulsun, and Li Pan (Siemens Corporation, Corporate Technology, USA), Peter Gall and Berthold Kiefer (Siemens Healthcare, Erlangen, Germany) for the development and the help and support with the MR OncoTreat software used for image processing.

References

- 1 Altekruse SF, McGlynn KA, Reichman ME. Hepatocellular carcinoma incidence, mortality, and survival trends in the United States from 1975 to 2005. *J Clin Oncol* 2009;27(9):1485-1491.
- 2 Jemal A, Siegel R, Xu J, Ward E. Cancer Statistics, 2010. *CA Cancer J Clin* 2010
- 3 Llovet JM, Bruix J. Systematic review of randomized trials for unresectable hepatocellular carcinoma: Chemoembolization improves survival. *Hepatology* 2003;37(2):429-442.
- 4 Camma C, Schepis F, Orlando A, et al. Transarterial chemoembolization for unresectable hepatocellular carcinoma: meta-analysis of randomized controlled trials. *Radiology* 2002;224(1):47-54.
- 5 Suzuki C, Jacobsson H, Hatschek T, et al. Radiologic measurements of tumor response to treatment: practical approaches and limitations. *RadioGraphics* 2008;28(2):329-344.

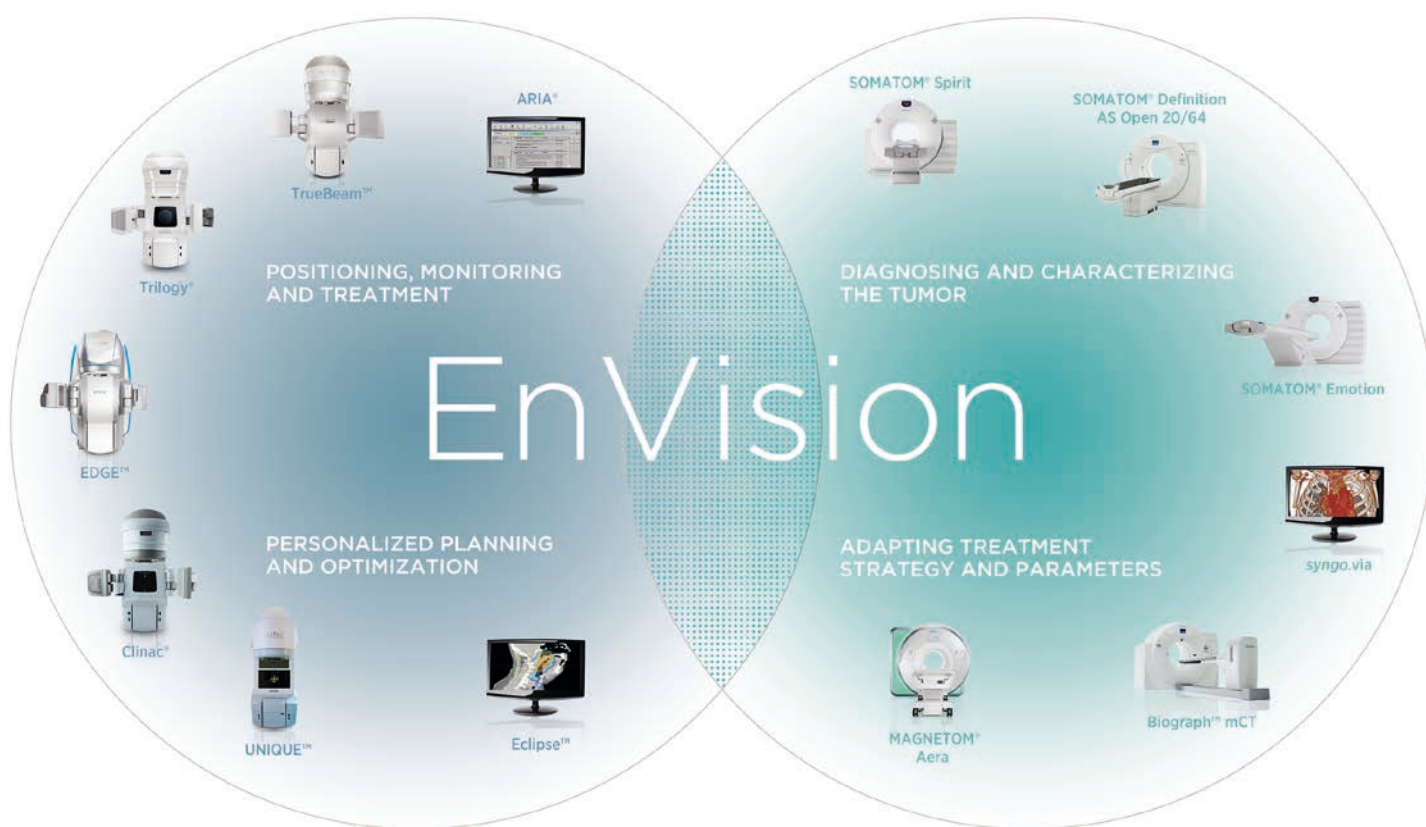
- 6 Suzuki C, Torkzad MR, Jacobsson H, et al. Interobserver and intraobserver variability in the response evaluation of cancer therapy according to RECIST and WHO-criteria. *Acta Oncol* 2010;49(4):509-514.
- 7 Moffat BA, Chenevert TL, Lawrence TS, et al. Functional diffusion map: a non-invasive MRI biomarker for early stratification of clinical brain tumor response. *Proc Natl Acad Sci U S A* 2005;102(15):5524-5529.
- 8 Bonekamp S, Jolepalem P, Lazo M, Gulsun MA, Kiraly AP, Kamel IR. Hepatocellular Carcinoma: Response to TACE Assessed with Semiautomated Volumetric and Functional Analysis of Diffusion-weighted and Contrast-enhanced MR Imaging Data. *Radiology* 2011;260(3):752-761.
- 9 Bonekamp S, Li Z, Geschwind JF, et al. Unresectable Hepatocellular Carcinoma: MR Imaging after Intraarterial Therapy. Part I. Identification and Validation of Volumetric Functional Response Criteria. *Radiology* 2013.
- 10 Bonekamp S, Halappa VG, Geschwind JF, et al. Unresectable Hepatocellular Carcinoma: MR Imaging after Intraarterial Therapy. Part II. Response Stratification Using Volumetric Functional Criteria after Intraarterial Therapy. *Radiology* 2013.
- 11 Gowdra Halappa V, Corona-Villalobos CP, Bonekamp S, et al. Neuroendocrine Liver Metastasis Treated by Using Intraarterial Therapy: Volumetric Functional Imaging Biomarkers of Early Tumor Response and Survival. *Radiology* 2012.
- 12 Halappa VG, Bonekamp S, Corona-Villalobos CP, et al. Intrahepatic cholangiocarcinoma treated with local-regional therapy: quantitative volumetric apparent diffusion coefficient maps for assessment of tumor response. *Radiology* 2012;264(1):285-294.
- 13 Li Z, Bonekamp S, Halappa VG, et al. Islet cell liver metastases: assessment of volumetric early response with functional MR imaging after transarterial chemoembolization. *Radiology* 2012;264(1):97-109.

Contact

Ihab R. Kamel, M.D., Ph.D.
The Johns Hopkins Hospital
Department of Radiology
600 N. Wolfe St, MRI 143
Baltimore, MD 21287
USA
Phone: +1 410-955-4567
ikamel@jhmi.edu

TOGETHER WE MOVE FORWARD IN THE FIGHT AGAINST CANCER

When two leading companies join forces in the fight against cancer, it broadens the realm of what's possible. That's why Varian and Siemens have partnered. Siemens' advanced diagnostic imaging capabilities coupled with Varian's powerful delivery systems and treatment planning tools give even more of an edge in the pursuit of our common goal: to **EnVision better cancer care**. Together we offer more personalized treatment and expanded care options that aid you in making the best possible decisions for your patients—with confidence. By gathering our strengths, we have the energy and vision to better help healthcare professionals detect, diagnose and treat cancer while paving the way for the future of cancer care.



VARIAN
medical systems

SIEMENS

Strategic Partner
of Varian for
Radiation Therapy

© 2013 Varian, Varian Medical Systems, Trilogy, and ARIA are registered trademarks, and TrueBeam, Edge Radiosurgery and Eclipse are trademarks of Varian Medical Systems, Inc. All other trademarks are property of Siemens AG.

Varian Medical Systems
International AG
Zug, Switzerland
Tel: +41 - 41 749 88 44
Fax: +41 - 41 740 33 40
varian.com
info.europe@varian.com

Global Siemens Healthcare
Headquarters
Siemens AG
Healthcare Sector
Henkestrasse 127
91052 Erlangen, Germany
Tel: +49 9131 84-0
siemens.com/healthcare

Find out more at varian.com/envision

PI-RADS Classification: Structured Reporting for MRI of the Prostate

M. Röthke¹; D. Blondin²; H.-P. Schlemmer¹; T. Franiel³

¹Department of Radiology, German Cancer Research Center (DKFZ), Heidelberg, Germany

²Department of Diagnostic and Interventional Radiology, University Hospital Düsseldorf, Germany

³Department of Radiology, Charité Campus Mitte, Medical University Berlin, Germany

Introduction

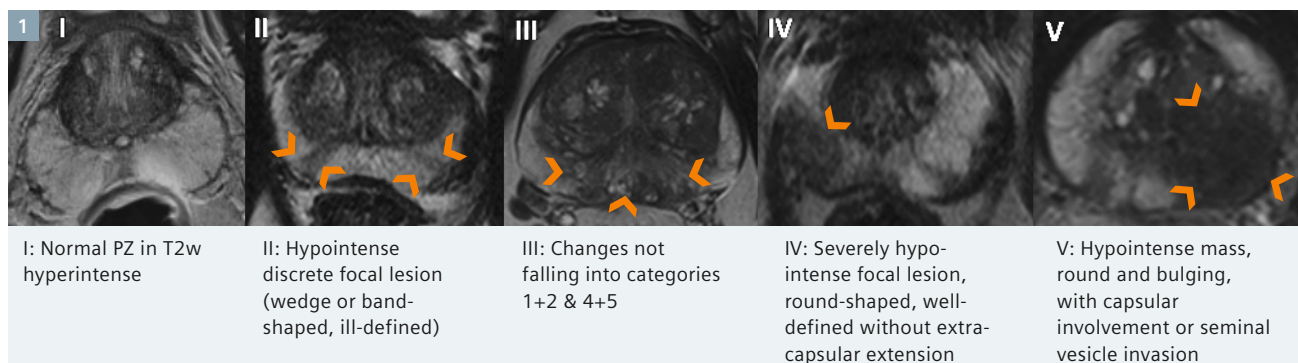
Prostate MRI has become an increasingly common adjunctive procedure in the detection of prostate cancer. In Germany, it is mainly used in patients with prior negative biopsies and/or abnormal or increasing PSA levels. The procedure of choice is multiparametric MRI, a combination of high-resolution T2-weighted (T2w) morphological sequences and the multiparametric techniques of diffusion-weighted MRI (DWI), dynamic contrast-enhanced MRI (DCE-MRI), and proton MR spectroscopy (¹H-MRS) [1, 2]. Previously, there were no uniform recommendations in the form of guidelines for the implementation and standardized communication of findings. To improve the quality of the procedure and reporting, a group of experts of the European Society of Urogenital Radiology (ESUR) has recently published a guideline for MRI of the prostate [3]. In addition to providing recommendations relating to indications and minimum standards for MR protocols, the guideline describes

a structured reporting scheme (PI-RADS) based on the BI-RADS classification for breast imaging. This is based on a Likert scale with scores ranging from 1 to 5. However, it lacks illustration of the individual manifestations and their criteria as well as uniform instructions for aggregated scoring of the individual submodalities. This makes use of the PI-RADS classification in daily routine difficult, especially for radiologists who are less experienced in prostate MRI. It is therefore the aim of this paper to concretize the PI-RADS model for the detection of prostate cancer using representative images for the relevant scores, and to add a scoring table that combines the aggregated multiparametric scores to a total PI-RADS score according to the Likert scale. In addition, a standardized graphic prostate reporting scheme is presented, which enables accurate communication of the findings to the urologist. Furthermore, the individual multiparametric techniques are described and critically

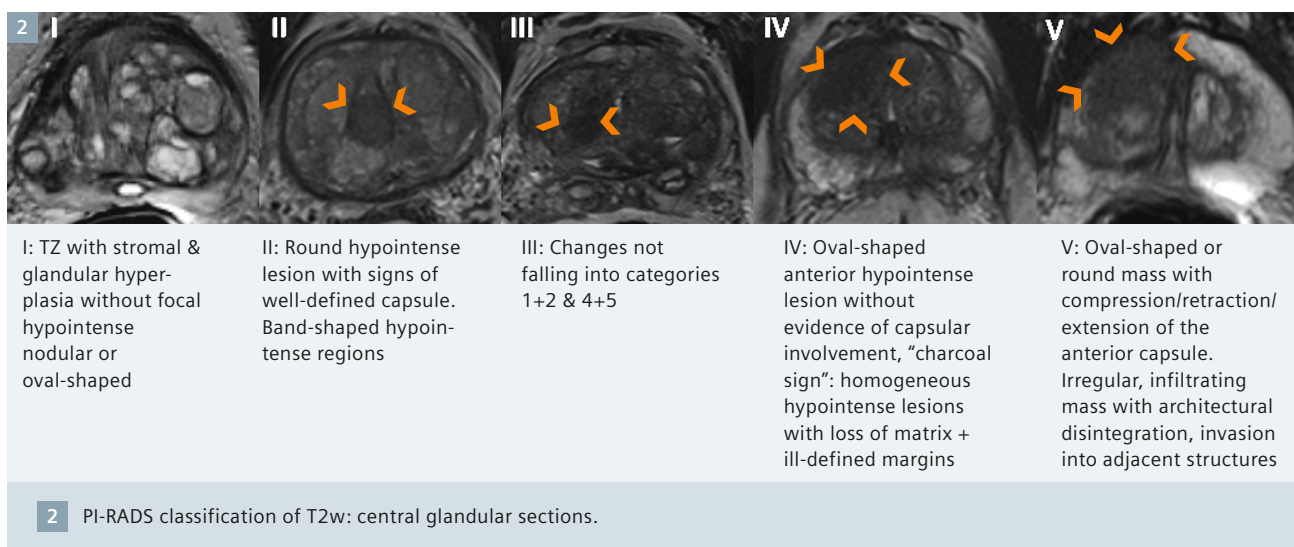
assessed in terms of their advantages and disadvantages.

Materials and methods

The fundamentals of technical implementation were determined by consensus. The sample images were selected by the authors by consensus on the basis of representative image findings from the 3 institutions. The scoring intervals for the aggregated PI-RADS score were also determined by consensus. The individual imaging aspects were described and evaluated with reference to current literature by one author in each case (T2w: M.R., DCE-MRI: T.F., DWI: D.B., MRS: H.S.). Furthermore, a graphic reporting scheme that allows the findings to be documented in terms of localization and classification was developed, taking into account the consensus paper on MRI of the prostate published in 2011 [4].



1 PI-RADS classification of T2w: peripheral glandular sections.



Implementation and technical requirements

According to the German interdisciplinary S3 guideline for prostate cancer, MRI of the prostate should be performed on a high-field scanner with a minimum field strength of 1.5 Tesla (T) using a combined endorectal-body phased-array coil in order to ensure a high signal-to-noise ratio in the prostate region [5]. If using 3T scanners and conventional MRI in combination with at least 2 multi-parametric techniques, an endorectal coil is not mandatory for the detection and localization of prostate cancer in our opinion. While administration of spasmolytics such as butylscopolamine is helpful in order to reduce intestinal peristalsis, we do not consider it essential [6].

Morphological T2w imaging

The high-resolution T2w turbo-spin-echo (TSE) sequences are the basis of MRI imaging of the prostate. T2w imaging visualizes morphological information of the prostate. A diagnostic challenge lies in the non-specific visualization of different but morphologically similar entities such as post-inflammatory or post-biopsy scars, atrophic changes, prostatitis, intraepithelial neoplasias (PIN), or post-treatment lesions [3]. The probability of detection decreases with decreasing size of the lesions [7].

In patients aged 50 years and older, the transition zone is increasingly

affected by nodular changes from benign prostatic hyperplasia (BPH), which complicate the detection of prostate cancer [8]. On the T2w images, the BPH nodules show different signal behaviors depending on the size of the epithelial and stromal components. While the epithelial component shows a hyperintense and the stromal component a hypointense signal behavior, combinations of both changes can also be seen. The BPH nodules are characterized by septation of the individual nodules, which can be seen as a hypointense rim on the T2w images [9]. Severely hypointense areas are non-specifically suggestive of prostate cancer [10]. Due to their infiltrating growth, aggressive prostate cancers in the central glandular zone spread across the septal structures, which is referred to as 'charcoal sign' [8]. Larger cancers of the central glandular zone also have a space-occupying component as a sign of malignancy. Aggressive cancers tend to have a more hypointense signal intensity with increasing Gleason score (≥ 7) [11].

At least 75% of all prostate cancers occur in the peripheral zone, where they appear localized and, when visualized by T2w imaging, predominantly distinctly hypointense compared to the hyperintense glandular tissue of the peripheral zone [12]. A visible space-occupying component or extracapsular extension must be interpreted as a reliable sign of malignancy. Smaller cancers can be localized,

but have irregular borders and finger-like processes. The cancer-specific changes shown on T2w images must be differentiated from the diffuse inflammatory contrasts caused by chronic prostatitis [13]. These can consist of mildly to severely hypointense diffuse changes which may be unilaterally localized, but may also affect the periphery on both sides. At the cicatricial stage, they consist of streaky changes which typically appear as triangular areas extending from the capsule to the apical/urethral margin. Less frequently than with diffuse changes, granulomatous prostatitis presents focal hypointense areas which can mimic prostate carcinoma. Post-biopsy hemorrhages (generally 3–6 months following biopsy) also appear hypointense on T2w, but hyperintense on T1w images. Previously biopsied areas may appear as scarred, strand-like hypo-intense changes on T2w images. Special attention must be paid to the rectoprostatic angle, since obliteration of the angle or asymmetry are indicative of extracapsular carcinoma [14].

The T2-weighted TSE sequence is acquired in the axial plane and complemented by a sagittal and/or coronal sequence. In addition to the T2w sequences, an axial T1w sequence should be acquired in order to visualize intraprostatic bleeding from inflammation or prior biopsies and, using an extended field-of-view (FOV), to detect enlarged parailiac and

locoregional lymph nodes suggestive of metastases. The high-resolution T2w sequences should have an echo time (TE) of 100 – 120 ms and a long repetition time (TR) of 4000–8000 ms (depending on the equipment and B₀ field strength). Parallel imaging may be used. A minimum slice thickness of 4 mm at 1.5 Tesla or 3 mm at 3 Tesla should be used, and a minimum in-plane resolution of 0.7 × 0.7 mm for both field strengths.

PI-RADS classification of T2w imaging

Since the diagnostic significance of the T2w-TSE sequences differs for the peripheral and central glandular zone, 2 separate schemes are recommended. Each lesion is given a score on a scale of 1 to 5. In the peripheral zone, in particular inflammatory lesions must be differentiated from lesions suspicious of cancer (Fig. 1). Lesions in the central glandular sections must be differentiated from clearly benign BPH nodules (Fig. 2). In addition, the presence of extracapsular extension, seminal vesicle invasion or involvement of the bladder neck must be documented [15].

Diffusion-weighted imaging

DWI allows the visualization and analysis of the movement (diffusion) of water molecules in the intracellular space. Molecular diffusion in tissue is generally restricted by cell structures and membranes. DWI allows the visualization and analysis of the movement (diffusion) of water molecules and expresses it by a parameter known as the apparent diffusion coefficient (ADC). Molecular diffusion in tissue is generally restricted by cell structures and membranes. Intracellular edemas or higher cell densities lead to a further reduction of free molecular movement. Such restrictions are reflected by a reduced ADC value. High cell densities occur, e.g., in tumor tissue, and thus also prostate carcinoma is characterized by reduced ADC values [16, 17]. Intracellular edemas or higher cell densities lead to a further reduction of free molecular movement, which is reflected by a reduced ADC value.

Consequently, prostate carcinoma is also characterized by reduced ADC values [16, 17]. In nearly all previously published studies, the ADC was analyzed using a mono-exponential model. As yet there have been only few publications on bi-exponential ADC analysis for the prostate [18, 19]. Therefore, the significance of the bi-exponential analysis, the static model, DTI or kurtosis [20 – 22] in the diagnosis of prostate cancer cannot be evaluated conclusively at this time. To allow the widespread use of DWI in multiparametric prostate MRI, the method used for calculation and analysis of the ADC should be practical, time-efficient and, above all, standardized. Several studies have shown that DWI analyzed with a mono-exponential model increases the sensitivity and specificity of detection of prostate cancer and allows better differentiation from benign hyperplasia [23–26]. The published ADC data are, however, inconsistent. The variations in the ADC results are due to different field strengths and different numbers and magnitudes of the selected b-values [27]. The most frequently used upper b-values are b=500, b=800 or b=1000 s/mm². The guidelines recommend an upper value of b=800–1000 s/mm². The authors prefer a value of 1000, which does, however, not deliver sufficient results with all gradient systems. In a study performed at 1.5T, the highest diagnostic accuracy in the detection of prostate cancer was achieved with a combination of T2 and DWI with an upper b-value of b=2000 s/mm² and using a surface coil [28]. For 3 Tesla exams, the use of an upper b-value of 2000 s/mm² cannot currently be recommended unequivocally [26], even though a current published study was able to demonstrate a benefit with b=2000 at 3 Tesla [29].

Prostate carcinomas usually show reduced ADC values and high signal intensity in the high-b-value image from DWI. In addition, the ADC values had negative correlation with the Gleason score of peripheral zone carcinomas. A significant difference was observed with tumors with a Gleason score of 6 compared to those with a

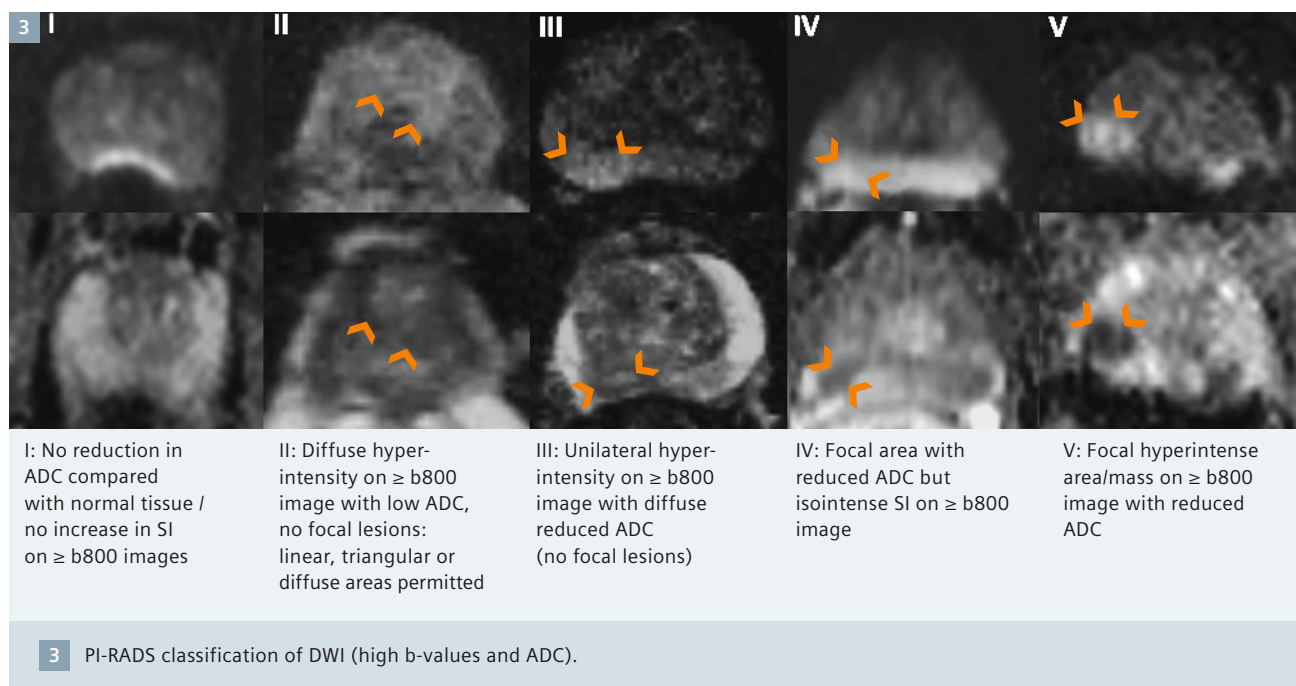
score of 7 or 8. There was no significant difference between tumors with a Gleason score ≥ 7 [30]. Other authors also demonstrated a linear reduction of the ADC of peripheral zone prostate carcinoma with increasing Gleason score and significant differences between low-grade, intermediate and high-grade PCa [31]. Even though there is not an exact correspondence of ADC thresholds and Gleason scores, DWI is still the most important tool in the detection of the most aggressive lesion (index lesion).

DWI should be performed with an echoplanar (EPI) sequence in the same axial orientation as the T2w imaging. The diffusion gradients should be applied in 3 orthogonal spatial directions. As a minimum 3, ideally 5, b-values between 0 and 800 – 1000 s/mm² should be used. Echo time should be as short as possible (typically < 90 ms). The sequence is prone to susceptibility artifacts, which can lead to distortions of the DWI images due to adjacent bowel gas. The measurement of the restricted diffusion in tumor tissue using high b-values improves the MRI diagnosis of prostate cancer.

PI-RADS classification of DWI

DWI is interpreted based on the high-b-value images (b ≥ 800 s/mm²) and the corresponding ADC parametric images (Fig. 3). A score of 1 is assigned if no focal decrease in signal intensity can be delineated on the ADC images, and no localized increase in signal intensity on the DWI images. Two points should be assigned for diffuse hyperintensities on the high-b-value image of the DWI with corresponding reduction of the ADC. This includes diffuse (e.g. triangular or linear) changes; focal, round areas are disregarded. Three points are assigned for unilateral (asymmetric) diffuse signal increase on the high-b-value image, which is diffusely decreased on the ADC map (no focality).

Four points are given for focal lesions that are clearly reduced on the ADC map, but are isointense on the high-b-value DWI image. Focal ADC reductions with corresponding focal signal increase on the DWI image (b ≥ 800 s/mm²) should be assigned 5 points.



For each evaluated lesion, an ADC value should be determined by ROI measurement and documented in the report. This quantitative ADC analysis depends on the magnetic field strength and the selected b-values. ADC limits should therefore be transferred or applied with caution [17]. Nevertheless, a high ADC value of $> 1000 \cdot 10^{-3} \text{ mm}^2/\text{s}$ is most likely to represent an inflammatory area or hyperplasia, and a significantly reduced ADC value of $< 600 \cdot 10^{-3} \text{ mm}^2/\text{s}$ a tumor.

DCE-MRI

DCE-MRI is a non-invasive technique that collects information on the vascularization of the prostate and the neo-angiogenesis of prostate cancer [32]. DCE-MRI usually measures T1w signal intensity (SI)-time(t) curves in the prostate tissue following the weight-adjusted administration of a gadolinium-based contrast medium (CM) in a bolus at an injection rate of 2.5 ml/s and subsequent injection of 20 ml of isotonic NaCl [2, 32]. For this, axial gradient echo sequences should be used. The temporal resolution should be at least 10 s (better ≤ 4 s to adequately follow the contrast medium through the tissue). To allow sufficient assessment of the SI-t curve, the sequence should be at least 5 min. long. Spatial resolution should be $0.7 \times 0.7 \text{ mm}^2$ to $1.0 \times 1.0 \text{ mm}^2$ at a slice thick-

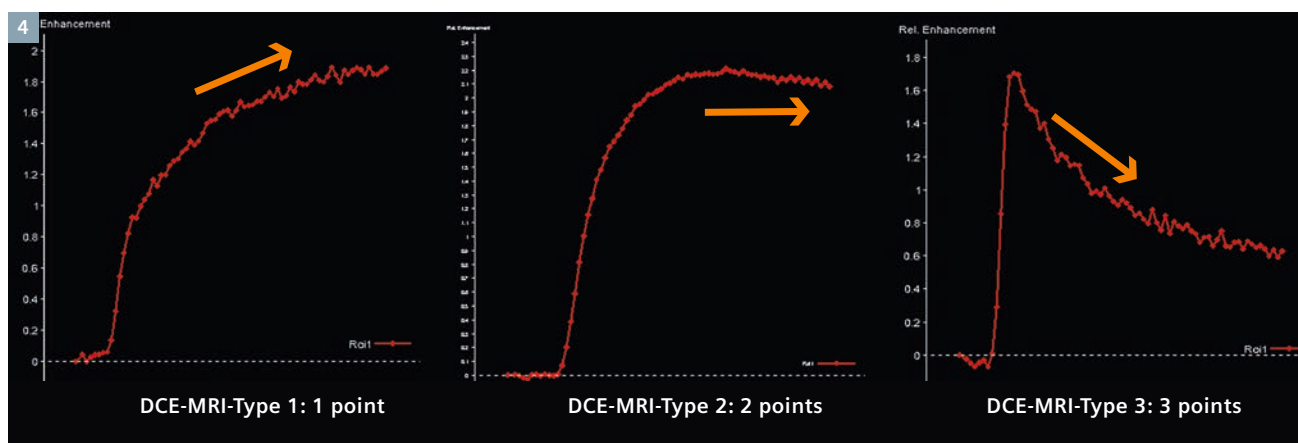
ness of 3 mm (distance factor 0.2). Alternatively, with 3 Tesla, isotropic voxels with a size of $(1.5 \text{ mm})^3$ can be generated, and optionally additional multiplanar reconstructions. The SI measurements enable a qualitative and semi-quantitative analysis of the DCE-MRI data. The qualitative analysis is based on the course of the SI-t curve. For the semi-quantitative analysis, a continuous SI-t curve is generated from the SI plotted over time. Based on this, the time to initial enhancement in the prostate tissue, the rise of the SI-t curve (wash-in), the maximum SI, and the fall of the SI-t curve (wash-out) is calculated [33]. Quantitative analysis of the DCE-MRI data by means of pharmacokinetic parameters requires conversion of the SI to CM concentrations [34]. The techniques and sequences used for this have recently been described in detail [2, 32]. The increasingly preferred pharmacokinetic model is the two-compartment model with the exchange constants K^{trans} (transfer constant) and k_{ep} (rate constant) [34].

Combined with conventional T1w and T2w imaging, DCE-MRI can detect and localize prostate cancer with better accuracy than conventional MRI [35 – 38], with the degree of improvement evidently depending on the experience of the reader.

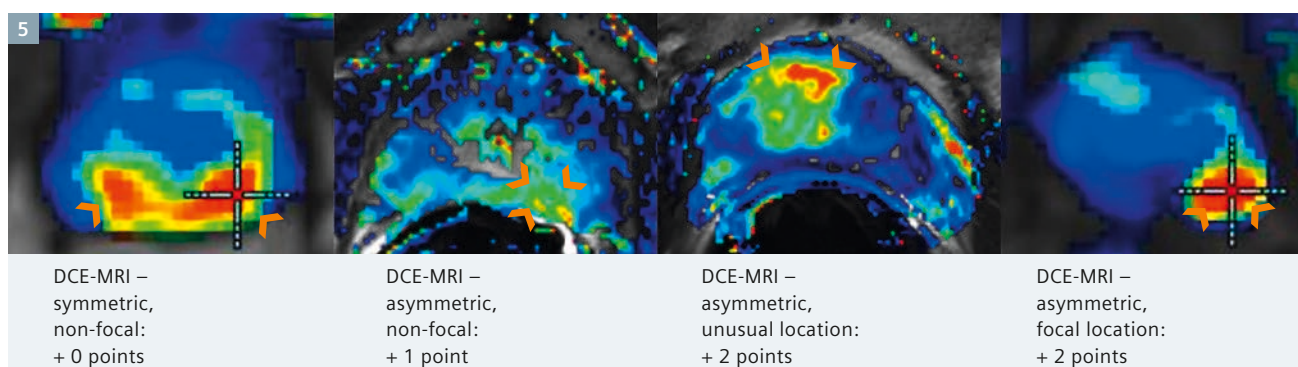
In the qualitative analysis, prostate cancers typically show a steeper wash-in slope, higher peak enhancement and steeper wash-out compared to normal prostate tissue. This correlates with the semiquantitative analysis, where prostate carcinoma tends to exhibit higher values of the individual parameter values as well [39, 40]. In the quantitative analysis, the pharmacokinetic parameters K^{trans} and k_{ep} also have higher values than normal prostate tissue [41].

In terms of differential diagnosis, prostatitis cannot be clearly differentiated from prostate cancer [42]. Similarly, it is not possible to reliably differentiate BPH nodules from central gland prostate cancers. The cause of false negative findings are prostate cancers which do not, or not significantly, differ from the surrounding normal tissue in terms of the degree of vascularization.

Based on current knowledge, no reliable recommendation can be made for assessing the aggressiveness of prostate cancer with DCE-MRI [4]. To date, only one study has demonstrated that low-grade prostate cancers were characterized by a statistically significantly larger blood volume and lower permeability than high-grade prostate cancers [43].



4 PI-RADS classification of DCE-MRI, part 1: Curve types.



5 PI-RADS classification of DCE-MRI, part 2: Additional points for distribution patterns with curve types II + III.

PI-RADS classification of DCE-MRI

The SI-t curves measured by DCE-MRI are the basis for the PI-RADS classification, the key element being the qualitative analysis of the curve shape following the initial rise of the SI-t curve (Fig. 4). In a type I curve, the SI gradually continues to increase (score 1). Type II curves are characterized by progressive SI stabilization (curve levels off) and a slight and late decrease in SI (score 2).

Type III curves show immediate wash-out after reaching peak enhancement (score 3). A point is added in the scoring system if there is a focal lesion with a type II or type III curve (Fig. 5). Another point is added for asymmetric lesions or unusually located lesions with type II or type III curves [3]. Unusual locations are the anterior parts of the transition zone and the anterior horns of the peripheral zone.

Symmetry and focality are assessed based on the surrounding tissue. In practice, it is helpful (although not mandatory) to assess focality by means of pharmacokinetic parameter maps. If new lesions are identified in the analysis of the pharmacokinetic parameter maps, these areas can also be assessed using the PI-RADS classification scheme. Here it must be noted that BPH nodules appear as focal lesions on the parameter maps and are characterized by type II or type III curves. No classification is necessary for lesions that can be clearly diagnosed as BPH nodules on the T2w image due to their hypointense rim.

MR spectroscopy of the prostate

Proton magnetic resonance spectroscopy allows the spatially resolved measurement of the relative concentration distributions of the metabo-

lites citrate, creatine and choline in the prostate. This metabolic information can increase the specificity of morphological prostate MRI and help assess individual tumor aggressiveness [44] and its progression over time, e.g. following antihormonal therapy [45] or during active surveillance [46].

Three-dimensional spatially resolved proton MR spectroscopy imaging (^1H -MRSI) is generally performed using a combination of two techniques, namely point resolved spectroscopy (PRESS) for volume-selective excitation, and chemical shift imaging (^1H -CSI) for spatial resolution with voxel sizes of up to 0.25 cm^3 . ^1H -MRSI is technically more complex than MR tomographic imaging and has several limitations in routine practice [47, 48]. Due to the high water content of human tissue, the proton, i.e. the nucleus of the most common hydro-

gen isotope (^1H), is the *in-vivo* nucleus that provides the strongest signal. Within the prostate parenchyma, the concentration of citrate, creatine and choline is approx. 10,000- to 100,000-fold lower than that of water. The signal intensity of these metabolite resonances in the ^1H -MR spectrum is thus reduced by the same factor, which complicates their visualization using this method. It is nevertheless possible to measure the resonances of the metabolites citrate, creatine and choline with only low signal-to-noise ratio. This requires a water and fat signal suppression pulse to enable the detection of the weak resonance lines of the metabolites against the background of the strong water signal on the one hand, and to suppress contamination of the spectra by signal from periprostatic lipids on the other hand. In addition, wide saturation bands must be placed closely around the prostate in order to suppress the strong water and fat signals from the surrounding tissue. Spectral quality critically depends on the local magnetic field homogeneity, which must be optimized prior to the data acquisition by automatic and possibly additional manual shimming. The total duration of the exam is approx. 10 – 15 min.

MRSI is evaluated by determining the relative signal intensity ratios of the resonance lines [choline + creatine]/citrate (CC/C). Since the choline and creatine resonances often cannot be resolved due to field inhomogeneities and consecutive line broadening, they are combined into one line (CC). The quality of the spectra should initially be assessed visually on a spectral map. For semiquantitative analysis of

the spectra, manufacturers are offering partly interactive software. To avoid partial volume effects, it may be necessary to retrospectively shift the voxel grid to adapt it to the precise anatomic localization of focal lesions.

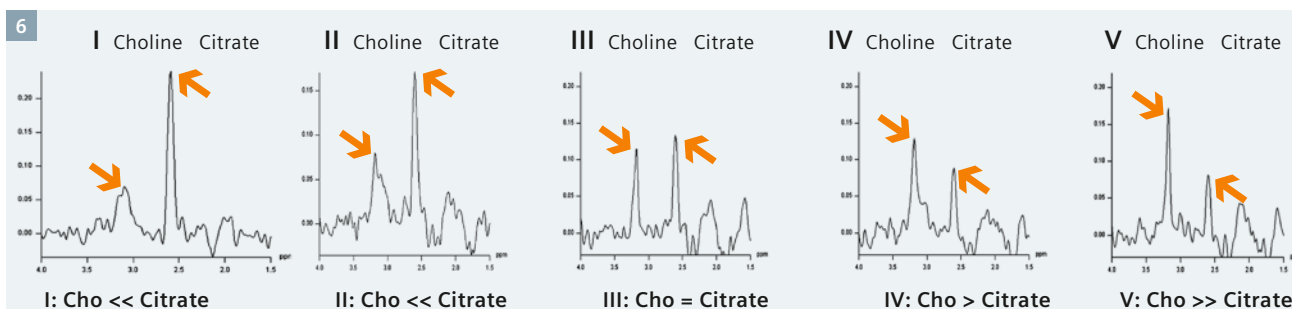
The MRSI procedure, including data acquisition, evaluation and interpretation of the spectra as well as documentation of the results, requires special expertise and a considerable amount of time (e.g. placement of saturation pulses, possibly manual shimming, interactive data evaluation and interpretation including quality assessment, visualization of results). The quality of the MRSI result depends not only on the physical-technical support, but also on the particular equipment (field strength, equipment generation, specific equipment properties, use of an endorectal coil) and the individual patient-specific examination setting (post-biopsy hemorrhage, possibly regional metal implants such as hip joint endoprosthesis or postoperative metal clips).

Citrate (C) is synthesized, secreted and stored in large quantities in normal glandular tissue of the prostate and is therefore used as an organ marker for healthy prostate tissue. Creatine plays an important role in the cells' energy metabolism and serves as an internal reference of intensity. Choline refers to the sum of choline-containing compounds, which includes various free choline compounds such as phosphocholine, glycerophosphocholine, free choline, CDP-choline, acetylcholine and choline plasmalogen. The intensity of the choline resonance reflects the

extent of membrane turnover and is significantly elevated in cancerous tissue [49]. The spatial distribution of relative signal intensity can be visualized through parameter maps and overlaid on the morphological T2w image as a color-coded map. MRSI does not provide any additional information on the localization of the cancer prior to radical prostatectomy as compared to conventional MRI [50]. Due to possible false negative results, in particular with small cancers, ^1H -MRSI also cannot be used to exclude cancer. Neither does MRS provide any additional information for local T-staging compared to MRI. Rather, it should be seen as an adjunctive tool to MRI that can increase the specificity in the classification of suspicious focal lesions, assess individual tumor aggressiveness, and provide progression parameters during active surveillance or conservative management. Compared to MRI, however, this method is more complex, more susceptible to artifacts and more difficult to standardize, resulting in it being of low practicality and acceptance outside specialized centers, and thus less commonly used.

PI-RADS classification ^1H -MRSI

In regard to the PI-RADS classification of the MR spectroscopy results, qualitative assessment of the CC/C ratio has proven useful in clinical routine. This involves the visual classification of relative signal intensities of the choline and citrate resonances based on a 5-point scale [51, 52]: Type 1: Cho is significantly lower than citrate (<<); type 2: Cho is elevated but still lower than citrate (<); type 3: Cho is approx-



6 PI-RADS classification of MR spectroscopy.

imately on the same level as citrate (=); type 4: Cho is elevated compared to citrate (>); type 5: Cho is significantly elevated compared to citrate (>>) (Fig. 6). Quantitative signal intensity ratios depend on the examination technique (1.5T versus 3T, sequence parameters), the evaluation program used and, in the case of interactive evaluation, examiner-related factors. Quantitative values for classifying the probability of cancer can only be determined in specialized centers and compared within a patient population examined and evaluated by consensus.

Sources of false positive findings are regions with either reduced citrate levels (in the anterior fibromuscular stroma and in stromal BPH nodules) or elevated choline levels (basal near the seminal vesicles and periurethral, since the seminal fluid contains elevated levels of glycerophosphocholine, as well as in prostatitis). False

negative findings can occur with small or infiltrating carcinomas, in particular mucous carcinomas.

Communication of findings

In analogy to the BI-RADS, the PI-RADS system offers the advantage of a standardized and easy communication of findings to other professional colleagues. Every lesion should be evaluated using a standardized graphic prostate scheme (Fig. 7) with at least 16, better 27, sectors. For each lesion, a point score between 1 and 5 is to be assigned per method. This is used to calculate the total score, which reflects the probability of the presence of clinically relevant cancer. The total score is then converted to the relevant PI-RADS score, providing the advantage that the final PI-RADS score is independent of the number of techniques used and can thus be easily communicated. Since the conversion of point scores is not explic-

itly explained in the ESUR guidelines, the authors recommend using the algorithm given in (Table 1). For routine clinical work, the authors further recommend that a diagnosis of suspected prostate cancer should be made if the PI-RADS score is 4 (≥ 10 points if 3 techniques are used and ≥ 13 points if 4 techniques are used) or higher. It must be stressed in this context that the thresholds of 10 and 13 are not yet evidence-based. A lower total score does not mean that the probability of prostate cancer is nil. These patients should therefore at least remain under clinical surveillance.

Conclusion

In summary, structured reporting of a lesion using the parametric approach increases the quality and diagnostic value of prostate MRI. Therefore, application of the PI-RADS scheme based on the representative images provided here is recommended for clinical rou-

7

Standardized MRI Reporting Scheme

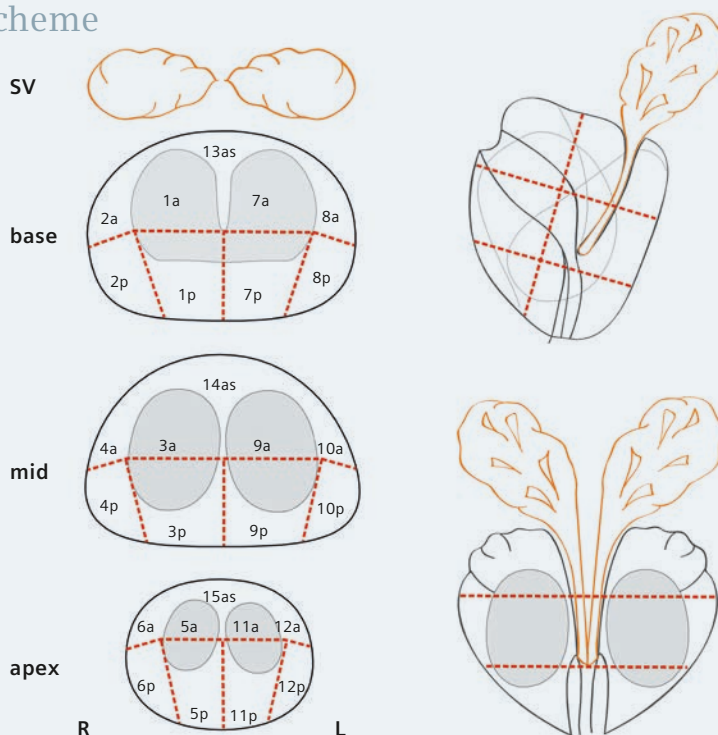
Name: _____
 Date: _____
 PSA: _____
 Previous Biopsies: _____
 Previous MRI scans: _____

Individual Scoring

Region	T2	DWI	DCE	MRS	Sum	PI-RADS

Total score PI-RADS:

PI-RADS: 1 – benign; 2 – most probably benign;
 3 – intermediate; 4 – probably malignant;
 5 – highly suspicious of malignancy



7

Standardized MRI prostate reporting scheme, PI-RADS.
 Parts of Fig. 7 are based on Dickinson et al. 2011 [4].

Table 1: PI-RADS score: Definition of total score and assignment of aggregate scores according to individual modalities used.

PI-RADS classification	Definition	Total score with T2, DWI, DCE	Total score with T2, DWI, DCE and MRS
1	most probably benign	3, 4	4, 5
2	probably benign	5, 6	6 – 8
3	indeterminate	7 – 9	9 – 12
4	probably malignant	10 – 12	13 – 16
5	highly suspicious of malignancy	13 – 15	17 – 20

tine. The standardized graphic reporting scheme facilitates the communication with referring colleagues.

Moreover, a standardized reporting system not only contributes to quality assurance, but also promotes wide-

spread use of the method and implementation of large-scale multicenter studies, which are needed for further evaluation of the PI-RADS system, in analogy to the BI-RADS system used in breast imaging.

This article has been reprinted with permission from: M. Röthke, D. Blondin, H.-P. Schlemmer, T. Franiel, PI-RADS-Klassifikation: Strukturiertes Befundungsschema für die MRT der Prostata Fortschr Röntgenstr 2013; 185(3): 253-261, DOI: 10.1055/s-0032-1330270 © Georg Thieme Verlag KG Stuttgart New York.

References

- Schlemmer HP. Multiparametric MRI of the prostate: method for early detection of prostate cancer? Fortschr Röntgenstr 2010; 182: 1067–1075. DOI: 10.1055/s-0029-1245786.
- Franiel T. Multiparametric magnetic resonance imaging of the prostate – technique and clinical applications. Fortschr Röntgenstr 2011; 183:607–617. DOI: 10.1055/s-0029-1246055.
- Barentsz JO, Richenberg J, Clements R et al. ESUR prostateMR guidelines 2012. Eur Radiol 2012; 22: 746–757. DOI: 10.1007/s00330-011-2377-y.
- Dickinson L, Ahmed HU, Allen C et al. Magnetic resonance imaging for the detection, localisation, and characterisation of prostate cancer: recommendations from a European consensus meeting. European urology 2011; 59: 477–494. DOI: 10.1016/j.eururo.2010.12.009.
- Krebsgesellschaft D. Interdisziplinäre Leitlinie der Qualität S3 zur Früherkennung, Diagnose und Therapie der verschiedenen Stadien des Prostatakarzinoms. 2011.
- Wagner M, Rief M, Busch J et al. Effect of butylscopolamine on image quality in MRI of the prostate. Clin Radiol 2010; 65: 460–464. DOI: S0009-9260(10)00106-6.
- Roethke MC, Lichy MP, Jurgschat L et al. Tumorsize dependent detection rate of endorectal MRI of prostate cancer – a histopathologic correlation with whole-mount sections in 70 patients with prostate cancer. Eur J Radiol 2011; 79: 189–195. DOI: S0720-048X(10)00045-8.
- Akin O, Sala E, Moskowitz CS et al. Transition zone prostate cancers: features, detection, localization, and staging at endorectal MR imaging. Radiology 2006; 239: 784–792. DOI: 2392050949.
- Janus C, Lippert M. Benign prostatic hyperplasia: appearance on magnetic resonance imaging. Urology 1992; 40: 539–541.
- Oto A, Kayhan A, Jiang Y et al. Prostate cancer: differentiation of central gland cancer from benign prostatic hyperplasia by using diffusion-weighted and dynamic contrast-enhanced MR imaging. Radiology 2010; 257: 715–723. DOI: radiol.1010002.
- Wang L, Mazaheri Y, Zhang J et al. Assessment of biologic aggressiveness of prostate cancer: correlation of MR signal intensity with Gleason grade after radical prostatectomy. Radiology 2008; 246: 168–176. DOI: 2461070057.
- Hricak H. Imaging prostate cancer. J Urol 1999; 162: 1329–1330.
- Kim CK, Park BK, Kim B. Localization of prostate cancer using 3T MRI: comparison of T2-weighted and dynamic contrast-enhanced imaging. J Comput Assist Tomogr 2006; 30: 7–11. DOI: 00004728-200601000-00002 [pii].
- Beyersdorff D, Taymoorian K, Knosel T et al. MRI of prostate cancer at 1.5 and 3.0 T: comparison of image quality in tumor detection and staging. Am J Roentgenol 2005; 185: 1214–1220. DOI: 10.2214/AJR.04.1584.
- Roethke MC, Lichy MP, Knies M et al. Accuracy of preoperative endorectal MRI in predicting extracapsular extension and influence on neurovascular bundle sparing in radical prostatectomy. World J Urol 2012. DOI: 10.1007/s00345-012-0826-0.
- Zelhof B, Pickles M, Liney G et al. Correlation of diffusion-weighted magnetic resonance data with cellularity in prostate cancer. BJU Int 2009; 103: 883–888.
- Sato C, Naganawa S, Nakamura T et al. Differentiation of noncancerous tissue and cancer lesions by apparent diffusion coefficient values in transition and peripheral zones of the prostate. J Magn Reson Imaging 2005; 21: 258–262. DOI: 10.1002/jmri.20251.
- Mulkern RV, Barnes AS, Haker SJ et al. Biexponential characterization of prostate tissue water diffusion decay curves over an extended b-factor range. Magn Reson Imaging 2006; 24: 563–568.
- Quentin M, Blondin D, Klaser J et al. Comparison of different mathematical models of diffusion-weighted prostate MR imaging. Magnetic resonance imaging 2012. DOI: 10.1016/j.mri.2012.04.025.
- Le Bihan D, Breton E, Lallemand D et al. Separation of diffusion and perfusion in intravoxel incoherent motion MR imaging. Radiology 1988; 168: 497–505.
- Yablonskiy DA, Bretthorst GL, Ackerman JJH. Statistical model for diffusion attenuated MR signal. Magn Reson Med 2003; 50: 664–669.
- Jensen JH, Helpert JA, Ramani A et al. Diffusional kurtosis imaging: the quantification of non-gaussian water diffusion by means of magnetic resonance imaging. Magn Reson Med 2005; 53: 1432–1440.
- Haider MA, van der Kwast TH, Tanguay J et al. Combined T2-weighted and diffusion-weighted MRI for localization of prostate cancer. Am J Roentgenol 2007; 189: 323–328.
- Pickles MD, Gibbs P, Sreenivas M et al. Diffusion-weighted imaging of normal and malignant prostate tissue at 3.0T. J Magn Reson Imaging 2006; 23: 130–134.

- 25 Ren J, Huan Y, Wang H et al. Diffusion-weighted imaging in normal prostate and differential diagnosis of prostate diseases. *Abdom Imaging* 2008; 33: 724–728.
- 26 Kim CK, Park BK, Kim B. High-b-value diffusion-weighted imaging at 3T to detect prostate cancer: comparisons between b values of 1,000 and 2,000 s/mm². *Am J Roentgenol* 2010; 194: 33–37. DOI: 10.1148/radiol.10091147.
- 27 Mueller-Lisse UG, Mueller-Lisse UL, Zamecnik P et al. Diffusion-weighted MRI of the prostate. *Radiologe* 2011; 51: 205–214.
- 28 Katahira K, Takahara T, Kwee TC et al. Ultra-high-b-value diffusion-weighted MR imaging for the detection of prostate cancer: evaluation in 201 cases with histopathological correlation. *Eur Radiol* 2011; 21: 188–196.
- 29 Kitajima K, Takahashi S, Ueno Y et al. Clinical utility of apparent diffusion coefficient values obtained using high b-value when diagnosing prostate cancer using 3 tesla MRI: Comparison between ultra-high b-value (2000 s/mm²) and standard high b-value (1000 s/mm²). *J Magn Reson Imaging* 2012. DOI: 10.1002/jmri.23627.
- 30 Woodfield CA, Tung GA, Grand DJ et al. Diffusion-weighted MRI of peripheral zone prostate cancer: comparison of tumor apparent diffusion coefficient with Gleason score and percentage of tumor on core biopsy. *Am J Roentgenol* 2010; 194: 316–322.
- 31 Vargas HA, Akin O, Franiel T et al. Diffusion-weighted endorectal MR imaging at 3T for prostate cancer: tumor detection and assessment of aggressiveness. *Radiology* 2011; 259: 775–784. DOI: 10.1148/radiol.11102066.
- 32 Franiel T, Hamm B, Hricak H. Dynamic contrast-enhanced magnetic resonance imaging and pharmacokinetic models in prostate cancer. *Eur Radiol* 2011; 21: 616–626. DOI: 10.1007/s00330-010-2037-7.
- 33 Huisman HJ, Engelbrecht MR, Barentsz JO. Accurate estimation of pharmacokinetic contrast-enhanced dynamic MRI parameters of the prostate. *J Magn Reson Imaging* 2001; 13: 607–614.
- 34 Tofts PS, Brix G, Buckley DL et al. Estimating kinetic parameters from dynamic contrast-enhanced T(1)-weighted MRI of a diffusible tracer: standardized quantities and symbols. *J Magn Reson Imaging* 1999; 10: 223–232.
- 35 Beyersdorff D, Ludemann L, Dietz E et al. Dynamic contrast-enhanced MRI of the prostate: comparison of two different post-processing algorithms. *Fortschr Röntgenstr* 2011; 183: 456–461. DOI: 10.1055/s-0029-1246051.
- 36 Franiel T, Stephan C, Erbersdobler A et al. Areas Suspicious for Prostate Cancer: MR-guided Biopsy in Patients with at Least One Transrectal US-guided Biopsy with a Negative Finding – Multiparametric MR Imaging for Detection and Biopsy Planning. *Radiology* 2011. DOI: radiol.10101251.
- 37 Ocak I, Bernardo M, Metzger G et al. Dynamic contrast-enhanced MRI of prostate cancer at 3 T: a study of pharmacokinetic parameters. *Am J Roentgenol* 2007; 189: 849.
- 38 Sciarra A, Panebianco V, Ciccariello M et al. Value of magnetic resonance spectroscopy imaging and dynamic contrast-enhanced imaging for detecting prostate cancer foci in men with prior negative biopsy. *Clin Cancer Res* 2010; 16: 1875–1883.
- 39 Engelbrecht MR, Huisman HJ, Laheij RJ et al. Discrimination of prostate cancer from normal peripheral zone and central gland tissue by using dynamic contrast-enhanced MR imaging. *Radiology* 2003; 229: 248–254.
- 40 Padhani AR, Gapinski CJ, Macvicar DA et al. Dynamic contrast enhanced MRI of prostate cancer: correlation with morphology and tumour stage, histological grade and PSA. *Clin Radiol* 2000; 55: 99–109.
- 41 Schlemmer HP, Merkle J, Grobholz R et al. Can pre-operative contrast-enhanced dynamic MR imaging for prostate cancer predict microvessel density in prostatectomy specimens? *Eur Radiol* 2004; 14: 309–317.
- 42 Franiel T, Lüdemann L, Rudolph B et al. Evaluation of normal prostate tissue, chronic prostatitis, and prostate cancer by quantitative perfusion analysis using a dynamic contrast-enhanced inversion-prepared dual-contrast gradient echo sequence. *Invest Radiol* 2008; 43: 481–487.
- 43 Franiel T, Lüdemann L, Taupitz M et al. Pharmacokinetic MRI of the Prostate: Parameters for Differentiating Low-Grade and High-Grade Prostate Cancer. *Fortschr Röntgenstr* 2009; 181: 536–542.
- 44 Shukla-Dave A, Hricak H, Ishill NM et al. Correlation of MR imaging and MR spectroscopic imaging findings with Ki-67, phospho-Akt, and androgen receptor expression in prostate cancer. *Radiology* 2009; 250: 803–812.
- 45 Mueller-Lisse UG, Swanson MG, Vigneron DB et al. Magnetic resonance spectroscopy in patients with locally confined prostate cancer: association of prostatic citrate and metabolic atrophy with time on hormone deprivation therapy, PSA level, and biopsy Gleason score. *Eur Radiol* 2007; 17: 371–378.
- 46 Fradet V, Kurhanewicz J, Cowan JE et al. Prostate cancer managed with active surveillance: role of anatomic MR imaging and MR spectroscopic imaging. *Radiology* 2010; 256: 176–183. DOI: radiol.10091147.
- 47 Verma S, Rajesh A, Futterer JJ et al. Prostate MRI and 3D MR spectroscopy: how we do it. *Am J Roentgenol* 2010; 194: 1414–1426.
- 48 Hoeks CMA, Barentsz JO, Hambrock T et al. Prostate cancer: multiparametric MR imaging for detection, localization, and staging. *Radiology* 2011; 261: 46–66.
- 49 Scheenen TWJ, Futterer J, Weiland E et al. Discriminating cancer from noncancer tissue in the prostate by 3-dimensional proton magnetic resonance spectroscopic imaging: a prospective multicenter validation study. *Invest Radiol* 2011; 46: 25–33.
- 50 Weinreb JC, Blume JD, Coakley FV et al. Prostate cancer: sextant localization at MR imaging and MR spectroscopic imaging before prostatectomy – results of ACRIN prospective multi-institutional clinicopathologic study. *Radiology* 2009; 251: 122–133. DOI: 251/1/122.
- 51 Futterer JJ, Scheenen TWJ, Heijmink SWTPJ et al. Standardized threshold approach using three-dimensional proton magnetic resonance spectroscopic imaging in prostate cancer localization of the entire prostate. *Invest Radiol* 2007; 42: 116–122.
- 52 Jung JA, Coakley FV, Vigneron DB et al. Prostate depiction at endorectal MR spectroscopic imaging: investigation of a standardized evaluation system. *Radiology* 2004; 233: 701–708.



Contact

Matthias Röthke, M.D.
 Department of Radiology
 German Cancer Research
 Center (DKFZ)
 Im Neuenheimer Feld 280
 69120 Heidelberg
 Germany
 Phone: +49(0)6221-422520
 m.roethke@dkfz.de

Case Study: Tumor Recurrence versus Treatment-Induced Change in a Patient with High-Grade Gliomas

Girish Fatterpekar, M.D.¹; Kent Friedman, M.D.¹; Christopher Glielmi, Ph.D.²; Fernando Boada, Ph.D.¹

¹ Department of Radiology, NYU Langone Medical Center, New York, NY, USA

² Siemens Healthcare, New York, NY, USA

Introduction

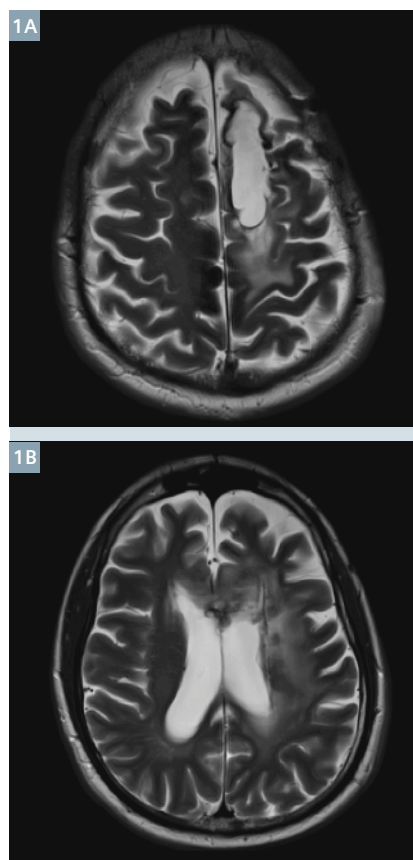
The prognosis for patients with high-grade gliomas is poor. Neuro-oncology trials are constantly looking to improve the overall survival of such patients. Toward this, the current treatment regimen following resection of primary high-grade glioma includes the use of radiation therapy, and chemotherapeutic agents such as temozolomide (TMZ) and bevacizumab. Preliminary results suggest some improvement in the overall survival of such patients. Unfortunately, the use of such a treatment regimen results in an imaging appearance that makes it difficult to distinguish treatment-induced changes from tumor recurrence based on conventional MR images. Advanced imaging techniques such as diffusion-weighted imaging (DWI) and dynamic susceptibility contrast (DSC)-perfusion imaging have tried to address this issue [1, 2]. The current case exquisitely illustrates the role of DWI, DSC-perfusion, and simultaneously acquired FDG-PET imaging in predicting tumor recurrence due to the presence of diffusion restriction and high rCBV values from the treatment bed. The highlighting feature of this case lies in demonstrating the utility of PET-MR in predicting tumor recurrence as suggested by foci of increased FDG-uptake corresponding to sites of tumor recurrence on DWI and DSC-perfusion imaging.

Patient history

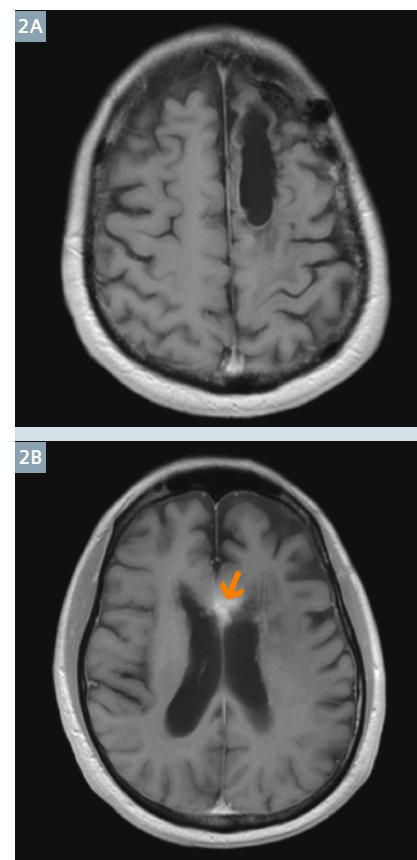
54-year-old male with history of left frontal glioblastoma. The presented imaging results follow surgical resection, radiation therapy and chemotherapy (TMZ and Avastin).

Sequence details

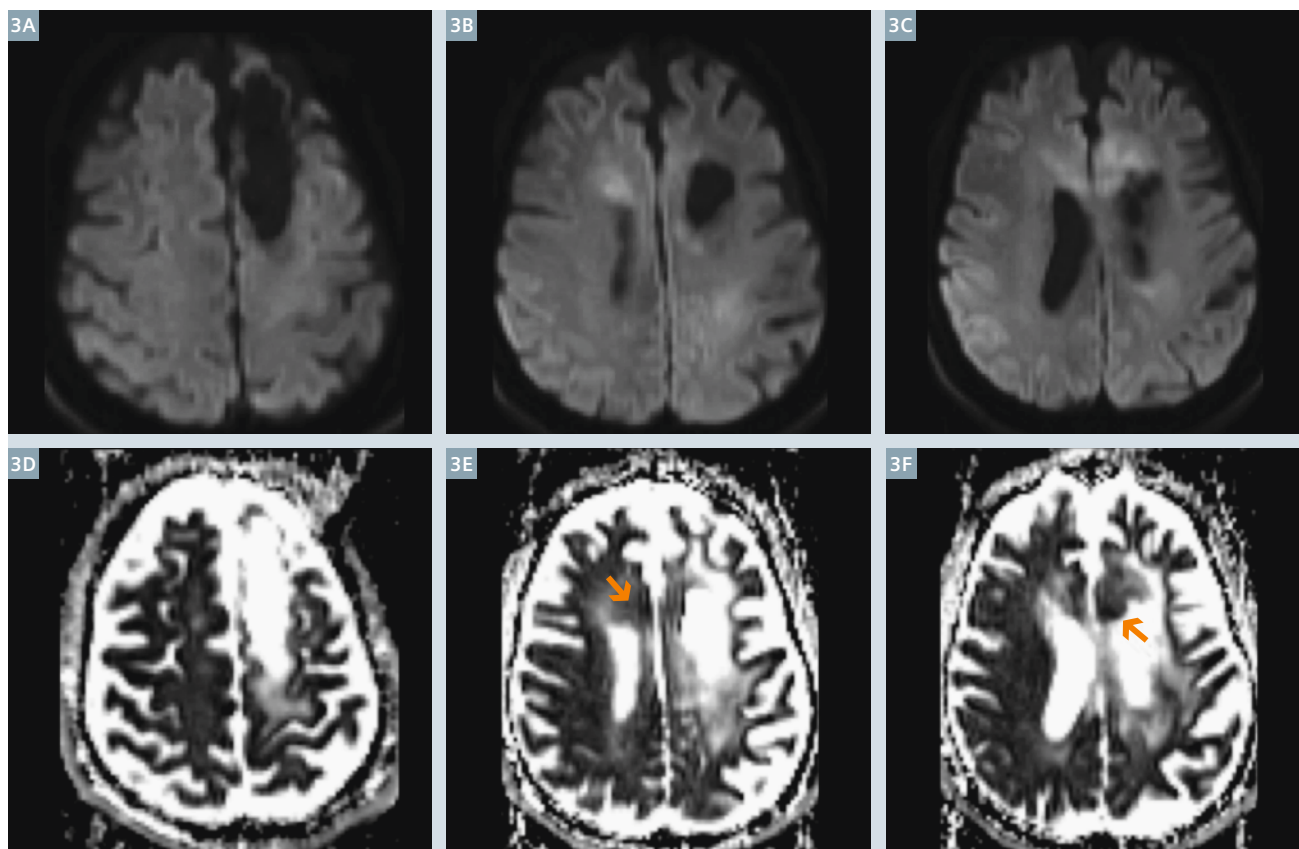
Simultaneous PET and MRI were acquired (Biograph mMR, Siemens Healthcare, Erlangen, Germany) using the tracer injection from the PET/CT exam performed on the same day. MR imaging of the brain including



1 Axial T2-weighted images demonstrate a surgical cavity in the left frontal region. Surrounding T2 bright signal abnormality is seen.



2 Corresponding contrast-enhanced T1w images demonstrate minimal heterogeneous enhancement (arrow).



3 Diffusion-weighted imaging and corresponding ADC maps demonstrate foci of restricted diffusion involving predominantly the genu of the corpus callosum (arrows).

axial and sagittal FLAIR, axial T2, diffusion, axial, coronal, and sagittal MPR, and axial T1 pre- and post-contrast images with 17 cc Magnevist intravenous contrast, and DSC-perfusion. PET imaging (15 minute list-mode) was acquired 139 minutes after 10.25 mCi injection of ^{18}F -FDG.

Imaging findings

The left frontal resection cavity appears unchanged in size since the prior examination. High T2/FLAIR signal surrounding the surgical cavity, anterior right frontal lobe and anterior body of corpus callosum has increased in size when compared to a prior study (Fig. 1).

There is new nodular enhancement in the genu and rostrum of the corpus callosum with mass effect. Some of this nodularity projects into the frontal horn of the left lateral ventricle

(Fig. 2). These areas of nodular enhancement demonstrate diffusion signal abnormality (Fig. 3) and hyperperfusion (Fig. 4) and are suspicious for recurrent tumor.

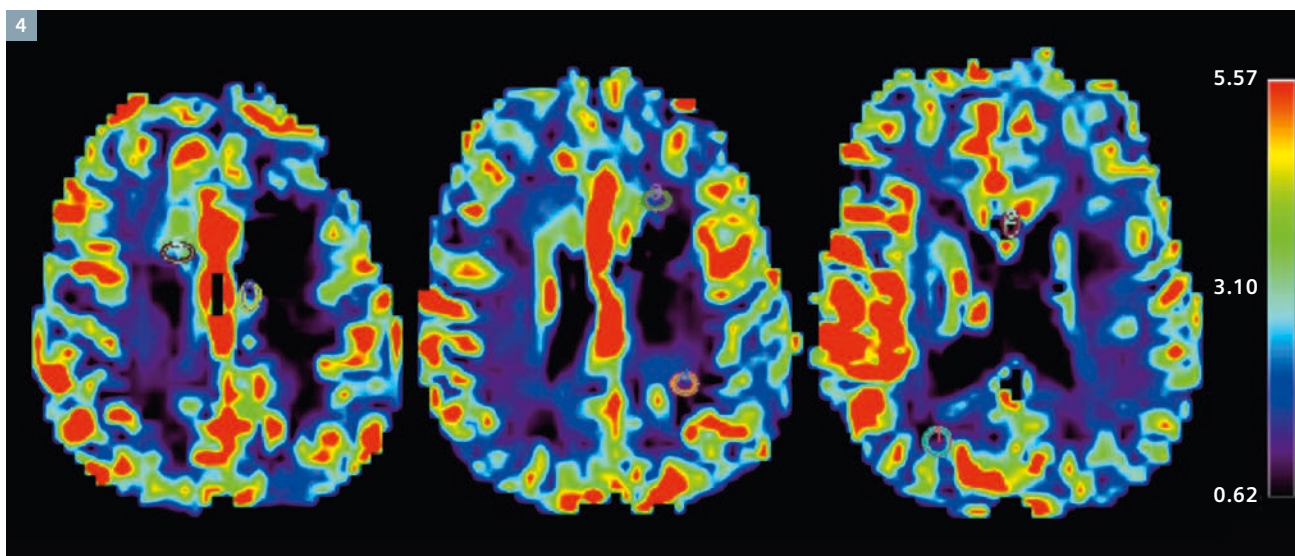
Furthermore, additional areas of diffusion signal abnormality are seen in the right frontal periventricular white matter and in the posteromedial margin of the left frontal resection cavity which demonstrate hyperperfusion and are also suspicious for recurrent tumor.

It is noted that there is mildly increased uptake (SUV_{MAX} : 7.1) associated with the new nodular enhancement at the genu and rostrum of the corpus callosum, left of midline (Fig. 5). The combined mild FDG uptake and new findings on MRI are concerning for recurrent tumor and less likely due to necrosis. There is no visible FDG uptake above background at the right

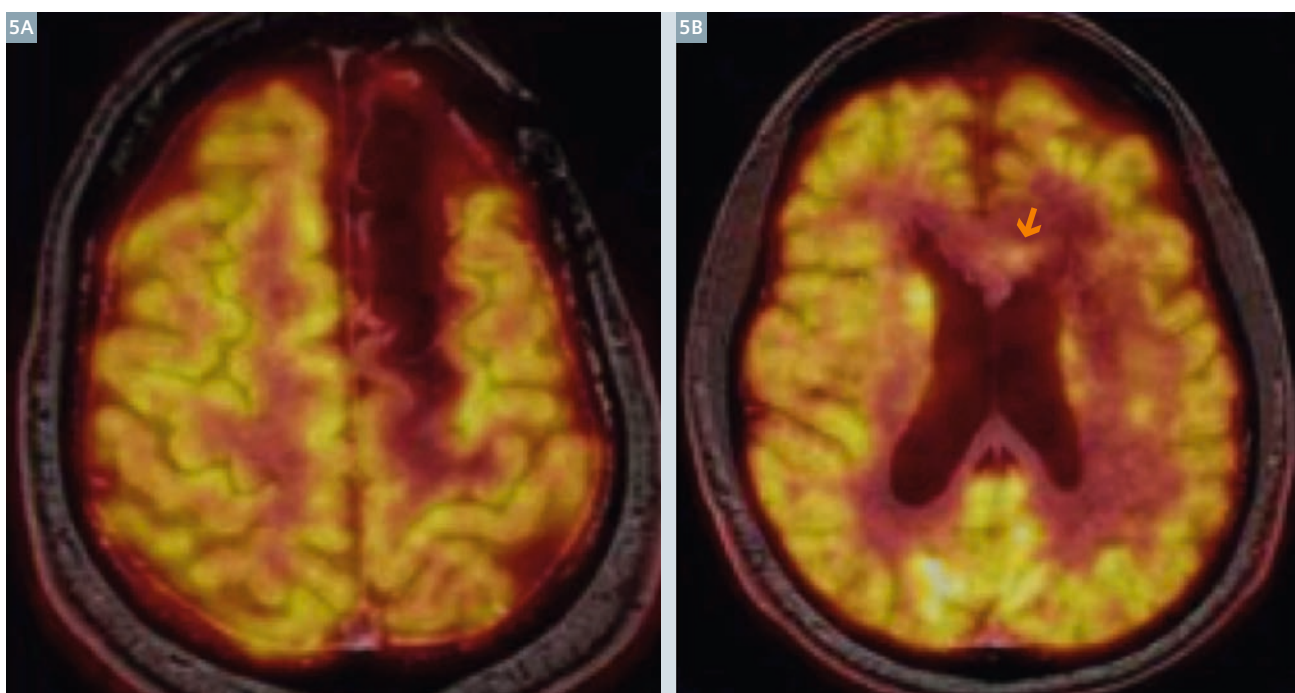
frontal periventricular white matter and at the posteromedial aspect of the left frontal resection cavity.

Conclusion

As this case demonstrates, the use of various MR contrasts in conjunction with simultaneously acquired PET shows promise to distinguish tumor recurrence from treatment-induced changes. The foci of increased FDG-uptake which corresponds to T2, DWI and DSC-perfusion, increased our confidence level and played a complementary role. The increased uptake as seen in this case suggests a promising role for PET-MR to distinguish tumor recurrence from treatment induced changes. However, these are only preliminary findings, and will need confirmation on larger patient population studies.



4 Corresponding DSC-MRI, perfusion maps demonstrate high rCBV (> 2.3) from the region of the treatment bed.



5 Corresponding PET-MR demonstrates areas of increased FDG-uptake (arrow) corresponding to areas of restricted diffusion and increased rCBV suggestive of tumor recurrence.

References

- 1 Fatterpekar GM, Galheigo D, Narayana A, Johnson G, Knopp E. Treatment-related change versus tumor recurrence in high-grade gliomas: a diagnostic conundrum – use of dynamic susceptibility contrast-enhanced (DSC) perfusion MRI. *AJR Am J Roentgenol*. 2012; 35(6):688-9.
- 2 Kim YH, Oh SW, Lim YJ, et al. Differentiating radiation necrosis from tumor recurrence in high-grade gliomas: assessing the efficacy of ^{18}F -FDG PET, ^{11}C -methionine PET and perfusion MRI. *Clin Neurol Neurosurg* 2010; 112(9):758-65.

Contact

Girish Fatterpekar, M.D.
Department of Radiology
NYU Langone Medical Center
New York, NY, USA
girish.fatterpekar@nyumc.org

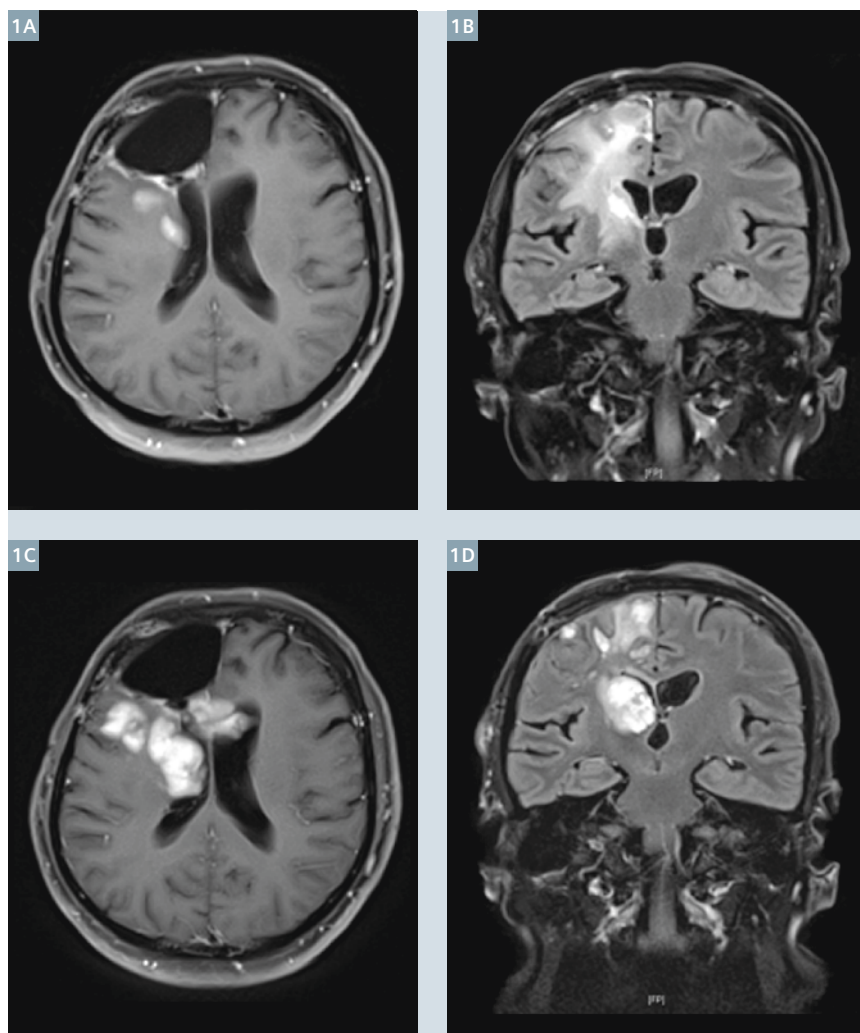
Clinical Application of Diffusion Tensor Imaging in Radiation Planning for Brain Tumors

S. Rogers¹; S. Bodis¹; G. Lutters¹; L. Remonda²; J Berberat^{1, 2}

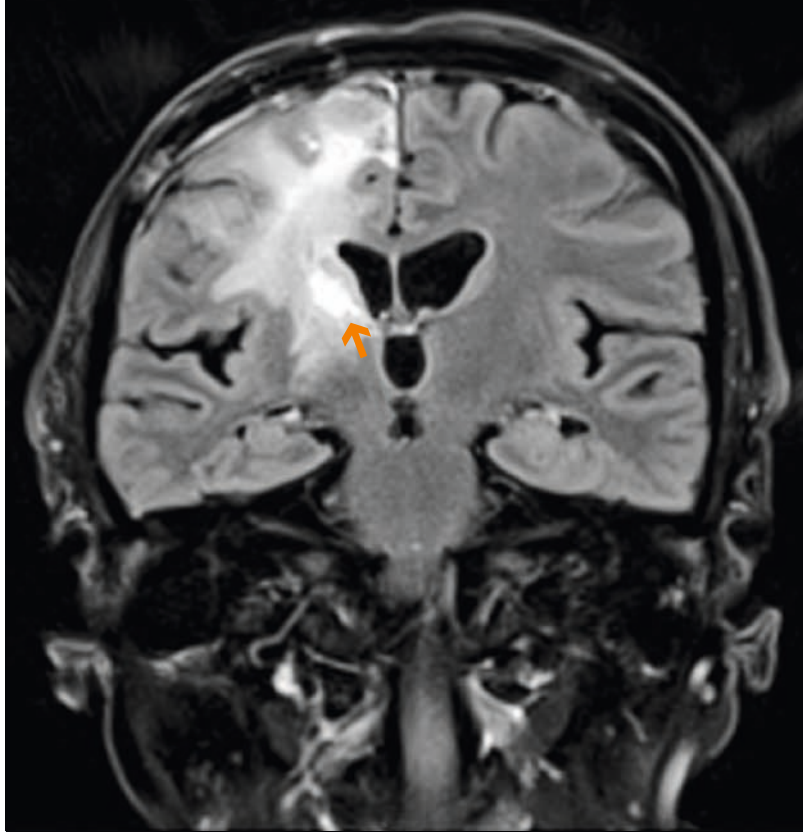
¹Radiation Oncology, Canton Hospital, Aarau, Switzerland

²Neuro-radiology, Canton Hospital, Aarau, Switzerland

Malignant brain tumors (glioma WHO grade III-IV) are notoriously difficult to treat despite an intensive combination of surgery, radiation and chemotherapy. Although there is an increasing number of 5-year survivors with this combined modality therapy, the median survival remains in the order of 14 months [1]. Pathological studies have demonstrated preferential tumor cell dissemination spread along white matter tracts and brain vessels [2], which limits the efficacy of both microsurgical resection and radiation therapy. The target for post-operative therapeutic radiation after maximal safe resection includes the resection cavity and any residual tumor visible on the postoperative T1-weighted Gadolinium-enhanced MRI. When surgery is not possible due to a high risk of neurological damage, a diagnostic biopsy is undertaken, followed by radiotherapy. To maximise the probability of including relevant microscopic spread from a glioblastoma (glioma WHO grade IV), uniform wide planning margins of up to 30 mm are typically added (Fig. 2B, green line). Some centres further extend this to include all visible edema on the T2-weighted imaging. Recent studies on the pattern of relapse in patients with high-grade glioma (HGG), predominantly glioblastoma, have suggested that tumor recurrence after maximal combined modality therapy occur within 2 cm of the original tumor location [3, 4]. This has led to a suggestion that a



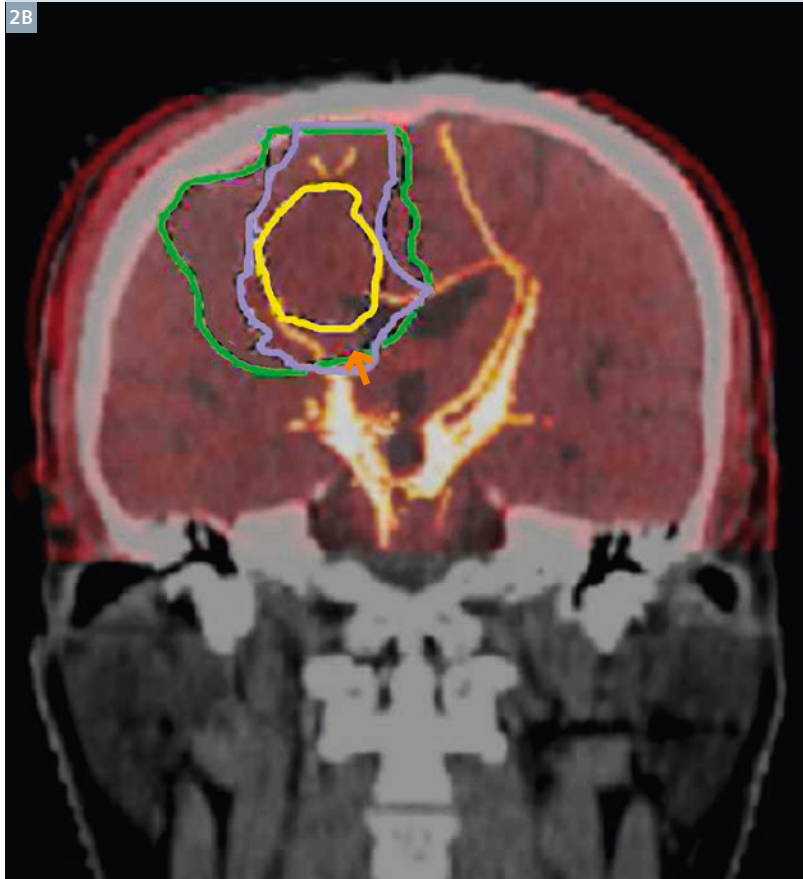
1 Transverse (T1w BLADE fs) and coronal (T2w TIRM dark fluid fs) MR images (1A, B) 12 months and (1C, D) 16 months after the operation. The patient developed a progressive tumor recurrence contiguous with residual tumor with subsequent extension along neighboring white matter tracts.



reduced margin, for example 1 cm, may be sufficient for the high-dose volume [3].

The addition of temozolomide chemotherapy as a radiation sensitizer and as adjuvant therapy is reported to be associated with an increased risk of normal brain toxicity (radionecrosis) of up to 20% [5]. Radiation-related side effects are dependent on both the prescription dose and the irradiated volume. A dose of at least 60 Gy has been shown to be necessary to control HGG, therefore it is compelling to instead reduce the planning target volume (PTV) where possible without compromising efficacy. Our aim is to derive a biologically targeted volume to ensure coverage of the regions at greatest risk of microscopic infiltration whilst excluding uninvolved brain. To this end, we have explored diffusion tensor imaging (DTI) and fractional anisotropy (FA) to identify areas of tumor infiltration, beyond that visible on T1w contrast-enhanced MRI. The method is derived from the isotropic (p) and anisotropic (q) maps of water diffusivity [6] and based on clinically validated data from patients with HGG [7].

Our technique is best illustrated using a clinical case as an example. This patient with histologically confirmed glioblastoma (GBM), showed tumor progression after surgery and radiation and developed a new lesion in the right thalamus (Fig. 1). The initial pre-operative work-up included DTI to assist the neurosurgeons in the identification and avoidance of apparently uninvolved white matter tracts to minimize the neurological sequelae of the surgery. All the MR imaging was done using a MAGNETOM Avanto 1.5T whole body scanner (Siemens Healthcare, Erlangen, Germany). These same scans were further analysed to extract data



2 Fusion of the MRI at recurrence 12 months post op with the DTI at recurrence 12 months post op suggests a route of spread via the radiologically abnormal right corticospinal tract.

regarding water diffusivity. The initial steps of the radiation planning technique were to co-register the T1w contrast-enhanced MRI with the planning CT scan. The residual enhancing tumor was contoured accordingly and the volume expanded by 1 cm (Fig. 2B, yellow line) to include brain at highest risk of infiltration. In addition, the DTI scan was co-registered and the volume was extended further along the tracts (Fig. 2B, purple line) in contact with the tumor to encompass likely microscopic spread. Any additional regions of tumor and infiltration, as detected by the p and q

maps, were delineated and then combined into the target volume by the planning software. This final volume was used to generate intensity modulated radiotherapy (IMRT) plans that were not used for clinical treatment (Fig. 2).

Using an in-house software program, we have developed a technique to incorporate regions of altered water diffusivity, reported to correspond with macroscopic tumor or microscopic infiltration, into the radiotherapy planning process. Conventional large volume irradiation for high-grade glioma carries an inevitable

risk of neuro-toxicity, which may be enhanced by combination with radiosensitizers. DTI and FA have previously been reported as diagnostic tools to assist with differential diagnosis, tumor grading, identifying tumor margins and predicting tumor relapse [7-9]. As white matter tracts and alterations in water diffusivity can also be targeted, we believe that future developments in radiation planning for HGG should endeavour to reduce the irradiated volume whilst maintaining adequate coverage of such regions likely to mediate relapse and spread.

References

- 1 Stupp R, Hegi ME, Mason WP, van den Bent MJ, Taphoorn MJ, Janzer RC, Ludwin SK, Allgeier A, Fisher B, Belanger K, Hau P, Brandes AA, Gijtenbeek J, Marosi C, Vecht CJ, Mokhtari K, Wesseling P, Villa S, Eisenhauer E, Gorlia T, Weller M, Lacombe D, Cairncross JG, Mirimanoff RO; European Organisation for Research and Treatment of Cancer Brain Tumour and Radiation Oncology Groups; National Cancer Institute of Canada Clinical Trials Group. Effects of radiotherapy with concomitant and adjuvant temozolomide versus radiotherapy alone on survival in glioblastoma in a randomized phase III study: 5-year analysis of the EORTC-NCIC trial. *Lancet Oncol*. 2009 10(5):459-66.
- 2 Giese A, Westphal M. Glioma invasion in the central nervous system. *Neurosurgery* 1996 39(2):235-50.
- 3 McDonald MW, Shu HK, Curran WJ Jr, Crocker IR. Pattern of failure after limited margin radiotherapy and temozolomide for glioblastoma. *Int J Radiat Oncol Biol Phys* 2011 1;79(1):130-6.
- 4 Milano MT, Okunieff P, Donatello RS, Mohile NA, Sul J, Walter KA, Korones DN. Patterns and timing of recurrence after temozolomide-based chemoradiation for glioblastoma. *Int J Radiat Oncol Biol Phys*. 2010 15;78(4):1147-55.
- 5 Rusthoven KE, Olsen C, Franklin W, Kleinschmidt-DeMasters BK, Kavanagh BD, Gaspar LE, Lillehei K, Waziri A, Damek DM, Chen C. Favorable prognosis in patients with high grade glioma with radiation necrosis: the University of Colorado experience. *Int J Radiat Oncol Biol Phys*. 2011 1;81(1):211-7.
- 6 Basser PJ, Mattiello J, LeBihan D. Estimation of the effective self-diffusion tensor from the NMR spin echo. *J Magn Reson B* 1994 103(3):247-54.
- 7 Price SJ, Jena R, Burnet NG, Hutchinson PJ, Dean AF, Peña A, Pickard JD, Carpenter TA, Gillard JH. Improved delineation of glioma margins and regions of infiltration with the use of diffusion tensor imaging: an image-guided biopsy study. *AJNR Am J Neuroradiol* 2006 27(9):1969-74.
- 8 Byrnes TJ, Barrick TR, Bell BA, Clark CA. Diffusion tensor imaging discriminates between glioblastoma and cerebral metastases in vivo. *NMR Biomed* 2011 24(1):54-60.
- 9 Mohsen LA, Shi V, Jena R, Gillard JH, Price SJ. Diffusion tensor invasive phenotypes can predict progression-free survival in glioblastomas. *Br J Neurosurg* 2013 27 [Epub ahead of print].

Contact

Jatta Berberat, Ph.D.
Canton Hospital
Tellstrasse
5001 Aarau
Switzerland
jatta.berberat@ksa.ch

Optimizing MRI for Radiation Oncology: Initial Investigations

James Balter¹; Yue Cao¹; Hesheng Wang¹; Ke Huang¹; Shu-Hui Hsu¹; Martin Requardt²; Steven M. Shea³

¹ Department of Radiation Oncology, University of Michigan, Ann Arbor, MI, USA

² Siemens Healthcare, Erlangen, Germany

³ Siemens Corporation, Corporate Technology, Baltimore, USA

Introduction

The superior soft tissue contrast, as well as potential for probing molecular composition and physiological behavior of tumors and normal tissues and their changes in response to therapy, makes MRI a tempting alternative to CT as a primary means of supporting the various processes involved in radiation therapy treatment planning and delivery. Obvious examples of the benefit of MRI over CT include target delineation of intracranial lesions, nasopharyngeal lesions, normal critical organs such as the spinal cord, tumors in the liver, and the boundaries of the prostate gland and likely cancerous regions within the prostate gland. For brachytherapy planning for cervical cancer, a recent GEC-ESTRO report directly recommends a change from traditional point-based prescriptions based primarily on applicator geometry, to

volumetric treatment plans and prescriptions aided by soft tissue visualization, specifically improved by the use of MRI. MRI-based maps of diffusion and perfusion have demonstrated potential for predicting therapeutic outcome for tumors as well as normal tissues, and current clinical trials seek to validate their roles and performance as a means to individualize therapy to improve outcomes (minimize toxicity and improve local tumor control). In addition to these advantages, MRI has been initially investigated as a means to better map the movement and deformation of organs over time and due to physiological processes such as breathing.

The historically accepted challenges in using MRI for primary patient modeling in radiation oncology have included distortion, lack of electron density information, and lack of

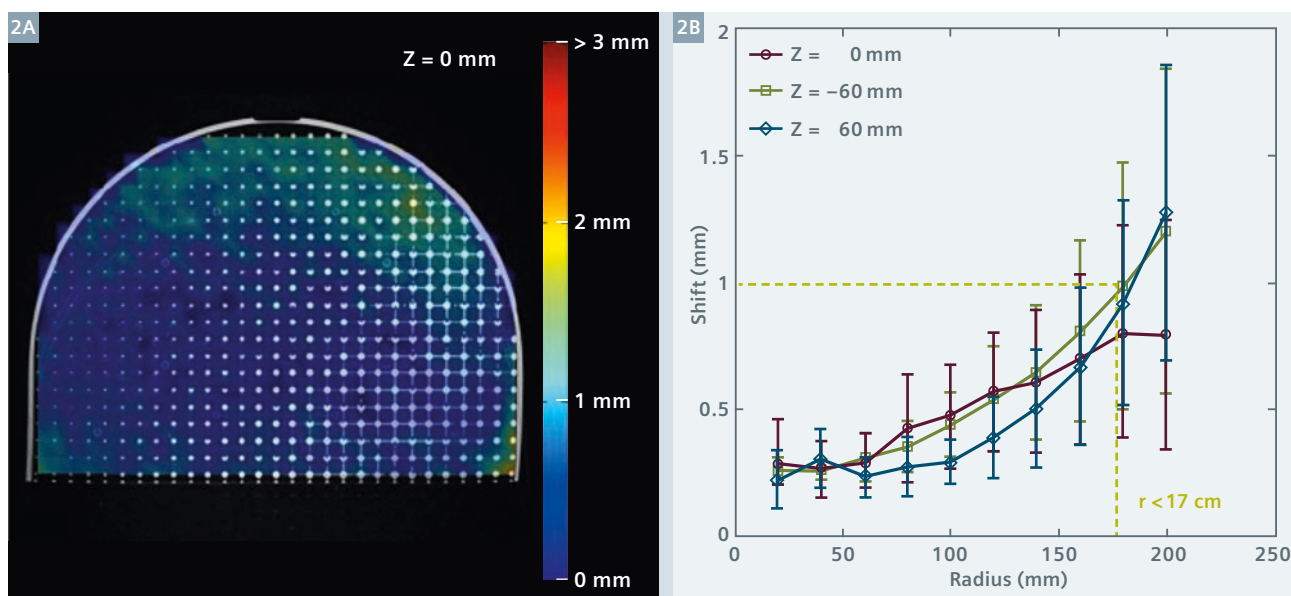
integrated optimized systems to scan patients immobilized in treatment configuration.

MRI 'simulator' system

Over the past several years, we have investigated the feasibility of MRI systems to function in the same roles that CT scanners have for the past 10–15 years, that is as primary tools for patient modeling for radiation therapy. These efforts have accelerated in the past years with the installation of a dedicated MRI 'simulator' at the University of Michigan, based on a 3T wide-bore scanner (MAGNETOM Skyra, Siemens Healthcare, Erlangen, Germany), outfitted with a laser marking system (LAP, Lueneburg, Germany) and separate detachable couch tops supporting brachytherapy and external beam radiation therapy applications.



1 MRI simulation system shows a volunteer in position for initial setup wearing a customized face mask (**1A**). Close-up view of anterior coil setup and crosshairs from laser marking system (**1B**).



2 Colorwash of measured distortion through an axial plane of the distortion phantom (2A). Magnitude of distortion-induced shifts in circles of increasing radius from the bore center in axial planes at the center and ± 6 cm along the bore (2B).

The process of integrating MRI into the standard workflow of radiation oncology requires attention be paid to a number of specific areas of system design and performance. In our instance, we chose a system that could potentially support both external beam therapy as well as brachytherapy. The brachytherapy requirement played a specific role in some of our design choices. As the high-dose-rate (HDR) brachytherapy system was housed in a room across the hall from the MRI suite, a room design was created that permitted the direct transfer of patients from MRI scanning to treatment. Typically brachytherapy treatment has involved transferring patients to and from imaging systems, a process that could potentially influence the treatment geometry and changes the dose delivered away from that planned. Treating a patient directly without moving them has significant advantages for geometric integrity as well as patient comfort. To facilitate such treatments, a detachable couch was chosen as part of the magnet specifications, and two such couches were specifically purchased to support simultaneous treatment of patients on the couch used for MRI scanning and scanning of other patients for subsequent external beam treatments.

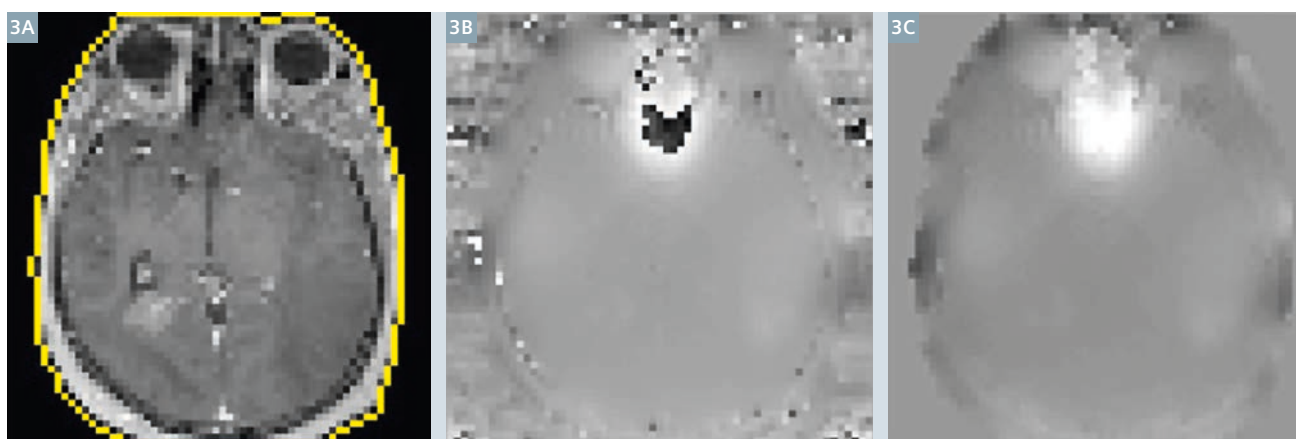
To support external beam radiotherapy, patients need to be scanned in positions and configurations that can be reproduced at treatment. In addition to necessitating a wide bore MRI scanner, an indexed flat table top insert was purchased from a company that specializes in radiation therapy immobilization systems (Civco, Kalona, IA, USA). A number of immobilization accessories were customized for use in the MRI environment, most notably a head and neck mask attachment system. To support high quality scanning of patients in treatment position without interfering with their configuration for treatment, a series of attachments to hold surface coils (primarily 18-channel body coils) relatively close to the patient without touching are used.

Initial commissioning and tests

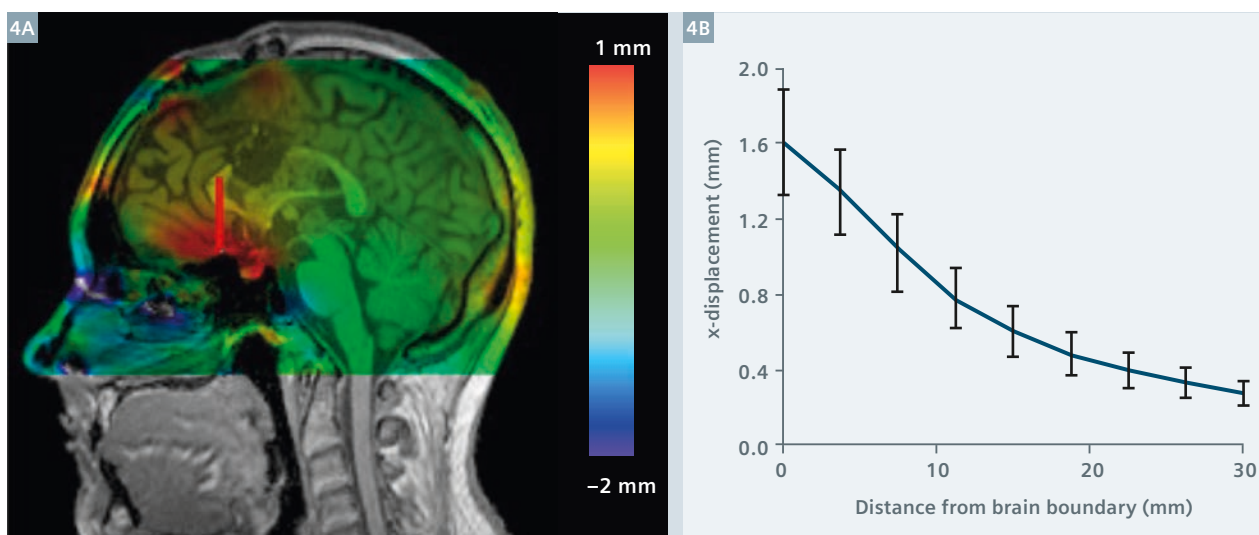
To commission the system, a number of tests were performed in addition to the standard processes for MRI acceptance and quality assurance. The laser system was calibrated to the scanner coordinates through imaging of a phantom with externally visible laser alignment markings and internal MRI-identifiable coordinates

indicating the nominal laser intersection, and end-to-end tests were performed on phantoms and volunteers to establish the accuracy of isocenter marking using MRI scans as a source of input.

To characterize system-level distortion, a custom phantom was developed to fill the bore of the magnet (with perimeter space reserved for testing the 18-channel body coil if desired). The resulting phantom was a roughly cylindrical section with a sampling volume measuring 46.5 cm at the base, with a height of 35 cm, and a thickness of 16.8 cm. This sampling volume was embedded with a three-dimensional array of interconnected spheres, separated by 7 mm center-to-center distances. The resulting system provided a uniform grid of 4689 points to sample the local distortion. The phantom was initially scanned using a 3D, T1-weighted, spoiled gradient echo imaging sequence (VIBE, TR 4.39 ms and TE 2.03 ms, bandwidth 445 Hz/pixel) to acquire a volume with field-of-view of $500 \times 500 \times 170$ mm with a spatial resolution of $0.98 \times 0.98 \times 1$ mm. Standard 3D shimming was used for scanning, and 3D distortion correction was applied to the images prior



3 T1-weighted image with external contour delineated as a mask (3A). The B_0 inhomogeneity map acquired from this subject (3B) was unwrapped within the boundaries of the mask, yielding the resulting distortion map (3C).
Reprinted with permission from Wang H, Balter J, Cao Y. Patient-induced susceptibility effect on geometric distortion of clinical brain MRI for radiation treatment planning on a 3T scanner. *Phys Med Biol* 58(3):465-77, 2013.



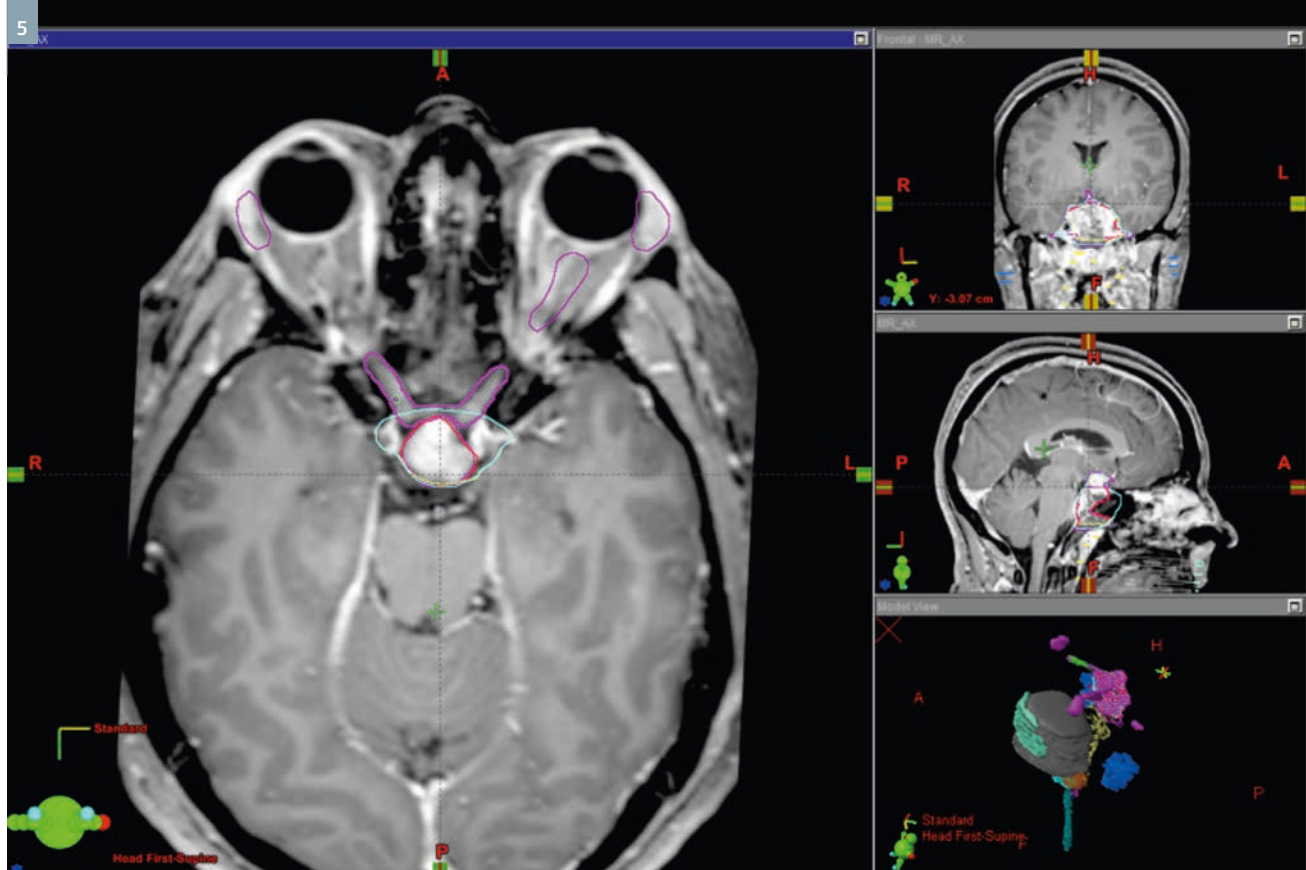
4 Colorwash of distortion-induced displacements through a sagittal plane of a subject (4A). Analysis of displacements along a line moving away from the sinus (red line in fig. 4A) shows the falloff of distortion due to susceptibility differences as a function of distance from the interface (4B).
Reprinted with permission from Wang H, Balter J, Cao Y. Patient-induced susceptibility effect on geometric distortion of clinical brain MRI for radiation treatment planning on a 3T scanner. *Phys Med Biol* 58(3):465-77, 2013.

to analysis. For this initial test, the body coil integrated into the magnet was used. Automated analysis of the images localized the sphere centers, yielding a deformation vector field that described the influence of system-level distortion on the measured sphere locations. This initial test demonstrated the accuracy of coordinate mapping via this scanning protocol, with average 3D distortions of less than 1 mm at radii of up to 17 cm in planes through the bore center

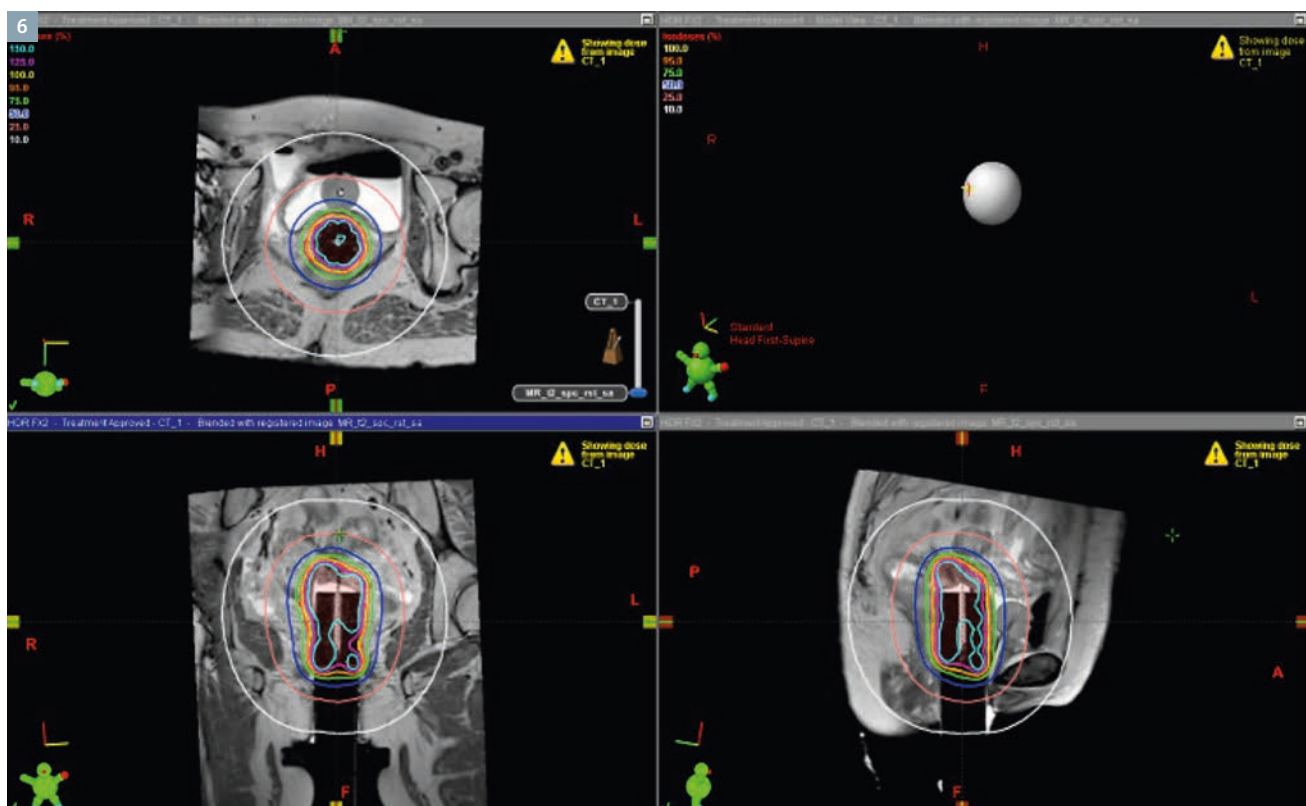
as well as ± 6 cm along the bore length. Of note, scanning was performed using the *syngo* MR D11 software version. Future tests will be performed on the *syngo* MR D13 release.

To begin to assess the impact of subject-induced susceptibility on distortions, B_0 inhomogeneity maps were acquired during routine patient scanning and analyzed (for 19 patients) under an IRB-approved protocol.

These maps were acquired using a 2D, double-echo, spoiled gradient echo sequence (GRE field mapping TE_1 4.92 ms, TE_2 7.38 ms, TR 400 ms, flip angle 60 degrees, voxel size $3.5 \times 3.5 \times 3.75$ mm), masked by the boundaries of the head acquired from T1-weighted images, and unwrapped using an algorithm from the Oxford Center for Functional Magnetic Resonance Imaging of the Brain [1]. The resulting maps showed homogeneity



5 Post-contrast T1-weighted images of a patient scanned in an immobilization mask using an anterior 18-channel body surface coil and a posterior 4-channel small soft coil and displayed in a radiation therapy treatment planning system (Eclipse, Varian, Palo Alto, CA, USA). Various delineated structures shown are used to guide optimization of intensity-modulated radiation therapy.



6 Display from a brachytherapy treatment planning system (Brachyvision, Varian, Palo Alto, CA, USA) showing orthogonal planes through cylindrical applicator implanted in a patient. Source locations (red dashes through the center of the applicator) are shown, as well as radiation isodose lines.

of 0.035 ppm or less over 88.5% of a 22 cm diameter sphere, and 0.1 ppm or less for 100% of this volume.

These inhomogeneity maps were applied to calculate distortions from a typical clinical brain imaging sequence (3D T1-weighted MPRAGE sequence with TE 2.5 ms, Siemens TR 1900 ms, TI 900 ms, flip angle 9 degrees, voxel size $1.35 \times 1.35 \times 0.9$ mm, frequency-encoding sampling rate of 180 Hz/pixel). On these images, 86.9% of the volume of the head was displaced less than 0.5 mm, 97.4% was displaced less than 1 mm, and 99.9% of voxels exhibited less than 2 mm displacement. The largest distortions occurred at interfaces with significant susceptibility differences, most notably those between the brain and either metal implants or (more significantly) adjacent air cavities. In the location with the largest displacement (interface with the sinus), the average displacement of 1.6 mm at the interface falls to below 1 mm approximately 7 mm away.

Examples of clinical use

We have implemented a number of scanning protocols in our first year of operation. Routine scans are performed for patients with intracranial lesions of all forms, as well as for those with nasopharyngeal tumors, hepatocellular carcinoma, and certain spinal and pelvic lesions. Routine use of the system for MRI-based brachytherapy of patients with cervical cancer using a ring and tandem

system is currently pending modification of part of the applicator for safety and image quality reasons, although patients undergoing other implants (e.g. cylinders) have had MRI scans to support treatment planning.

Summary

We have implemented the initial phase of MRI-based radiation oncology simulation in our department, and have scanned over 300 patients since operations began just over one year ago. The system demonstrates sufficient geometric accuracy for supporting radiation oncology decisions for external beam radiation therapy, as well as brachytherapy. Work is ongoing in optimizing MRI scanning techniques for radiation oncology in various parts of the body and for various diseases. In addition to current and future work in optimizing MRI for use in routine radiation therapy,

a variety of research protocols are underway using this system. A major current focus is on using MRI without CT for external beam radiation therapy. Results of these efforts will be presented in future articles.

References

- 1 Jenkinson M. Fast, automated, N-dimensional phase-unwrapping algorithm. *Magn Reson Med*. 2003 Jan;49(1):193-7.
- 2 Dimopoulos JC, Petrow P, Tanderup K, Petric P, Berger D, Kirisits C, Pedersen EM, van Limbergen E, Haie-Meder C, Pötter R. Recommendations from Gynaecological (GYN) GEC-ESTRO Working Group (IV): Basic principles and parameters for MR imaging within the frame of image based adaptive cervix cancer brachytherapy. *Radiother Oncol* 103(1):113-22, 2012.
- 3 Wang H, Balter J, Cao Y. Patient-induced susceptibility effect on geometric distortion of clinical brain MRI for radiation treatment planning on a 3T scanner. *Phys Med Biol* 58(3):465-77, 2013.



Contact

James M. Balter, Ph.D., FAAPM
Professor and co-director,
Physics division
Department of Radiation Oncology
University of Michigan
Ann Arbor, MI
USA
Phone: +1(734)936-9486
jbalter@umich.edu

MAGNETOM Combi Suite Radiation Therapy. Combining MRI Intelligence and Therapeutic Expertise

Annemarie Hausotte, Ph.D.

Siemens Healthcare, Imaging & Therapy Division, Erlangen, Germany

MRI's excellent soft-tissue differentiation supports target structure delineation, helps to identify structures and organs at risk, and therefore contributes to accurate treatment planning and delivery.

The MAGNETOM Combi Suite Radiation Therapy, which is available for 1.5T MAGNETOM Aera and 3T MAGNETOM Skyra, is a perfect tool for the radiation therapy (RT) treatment planning workflow.

Today's standard for radiation therapy planning

In 2009, nearly one million patients in the U.S. received radiation therapy.

Approximately 88% of these patients received external beam treatments from a linear accelerator [1], which demands careful treatment planning, precise patient set-up, and reproducible patient positioning. Patients are immobilized during pre-treatment imaging and throughout the treatment with positioning devices such as thermoplastic masks or vacuum cushions, ideally in exactly the same way throughout.

In 2009, 98% of all image-based RT treatment plans in the U.S. were based on computed tomography (CT) images [2]. In nearly all cases where MR images were used within the

context of treatment planning, these were used in conjunction with CT images. CT data – acquired for example with a Siemens SOMATOM Definition AS Open system – serves as the primary data for localizing target structures and organs at risk, for calculating dose, and for simulating the treatment.

MRI intelligence for radiation therapy planning

MRI offers excellent soft-tissue contrast without radiation dose, making it ideal for oncology imaging and – especially – radiation therapy planning, where CT data can be enhanced by valuable multi-contrast as well as

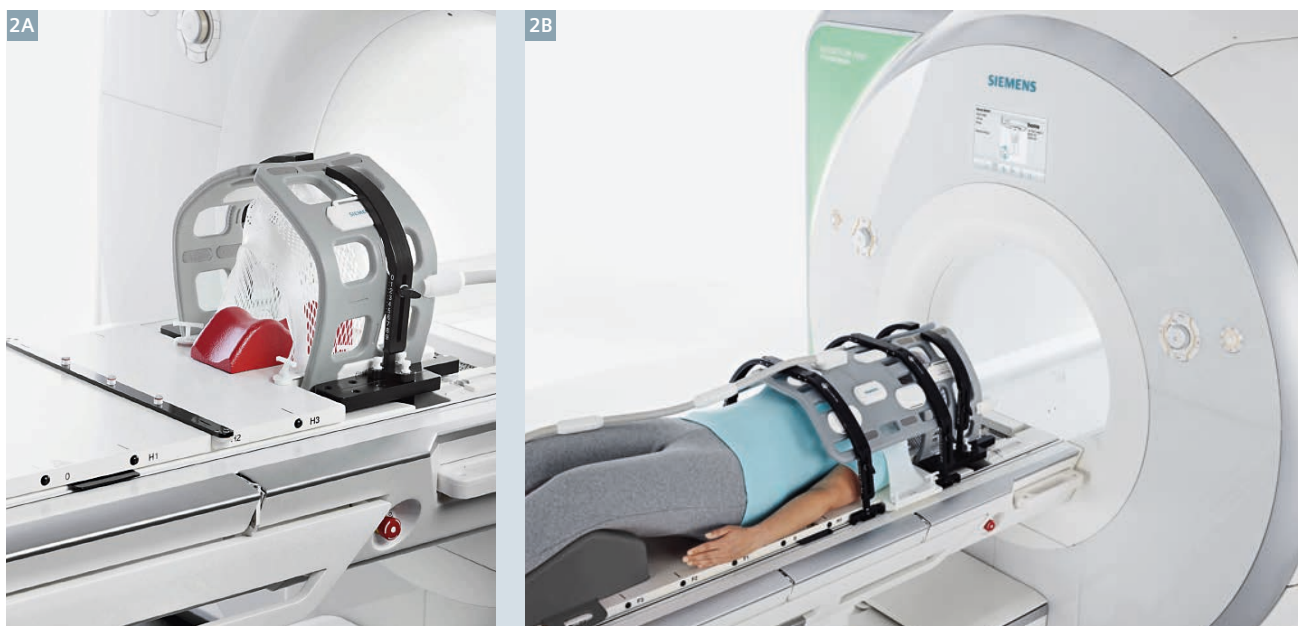
1A



1B



1 Siemens' recommended MR systems supporting RT imaging. (1A) 1.5T MAGNETOM Aera and (1B) 3T MAGNETOM Skyra with the MAGNETOM Combi Suite Radiation Therapy.



2 MAGNETOM Combi Suite Radiation Therapy options. **(2A)** Flat couch top with indexing, allowing RT-like patient set-up. The Flex 4 coils enable imaging even in the case of thermoplastic mask fixation. The coil holders help to mount the coils. **(2B)** Set-up with the Body 18 coil mounted close to the patient without contact.

multi-parametric MR data for additional confidence in treatment planning. Fast isotropic 3D sequences such as SPACE or VIBE along with 3D distortion correction enable better anatomical correlation. Advanced applications and imaging sequences, such as REVEAL and MR spectroscopy, offer additional pathology characterization.

Tumors of the brain, in the head & neck region or tumors of the prostate or rectum are good examples of cases where MRI can provide useful additional information for treatment planning, offering high-quality image-guided treatments to patients. Other examples are cervical tumors and gynecological tumors in general. MR images provide great accuracy in defining target structures and organs to be spared during treatment.

Accounting for the needs of radiation therapy in MRI

MAGNETOM Aera and MAGNETOM Skyra, both featuring a 70 cm open bore design, are today's top-of-the-line choices in 1.5T and 3T MRI systems. The bore size supports very different patient set-ups, as is the case for radiation therapy planning imaging. Inte-

grated Tim 4G coil technology offers up to 204 coil elements, delivering more signal than ever. With its high-density coils, Tim 4G also enables up to 128 channels and can be flexibly integrated into a variety of different applications to support even large anatomical coverage. The Tim Dockable Table supports the MRI workflow at both radiology-installed scanners and dedicated radiation oncology MR systems, by allowing the patient to be prepared outside the scanner room. This enables scanning within standard radiological timeslots and increases workflow flexibility. Finally, the MAGNETOM Combi Suite Radiation Therapy allows for reproducible radiation therapy-like positioning during MR scanning, easing the enhancement of CT data with MRI data during the treatment planning process.

MAGNETOM Combi Suite Radiation Therapy

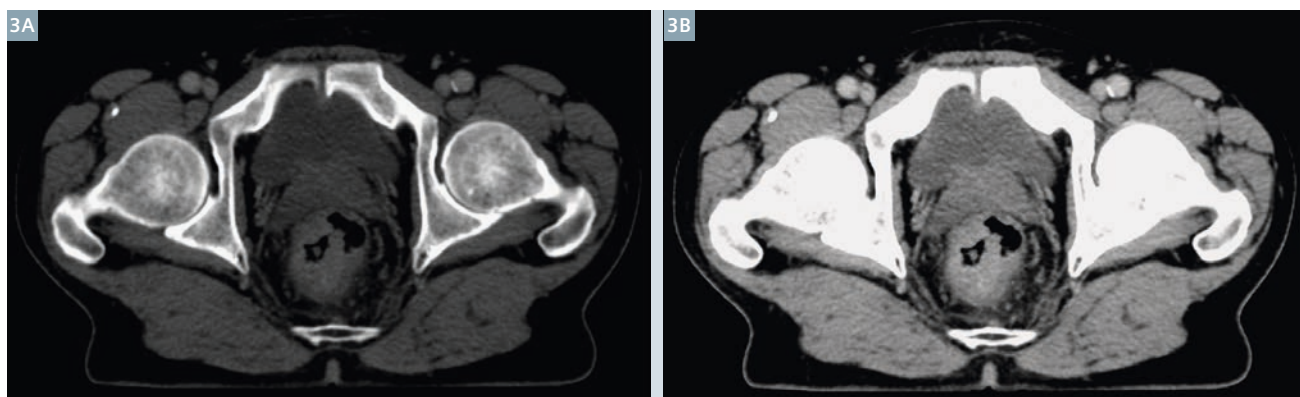
MAGNETOM Combi Suite Radiation Therapy comprises Siemens' comprehensive offering of MRI-related solutions to support high accuracy radiation therapy treatment planning. Table 1 lists the various components of the suite.

Manufacturers of radiation therapy positioning devices, including CIVCO, offer a variety of MR-compatible patient positioning devices (fitting the CIVCO RT Positioning Package).

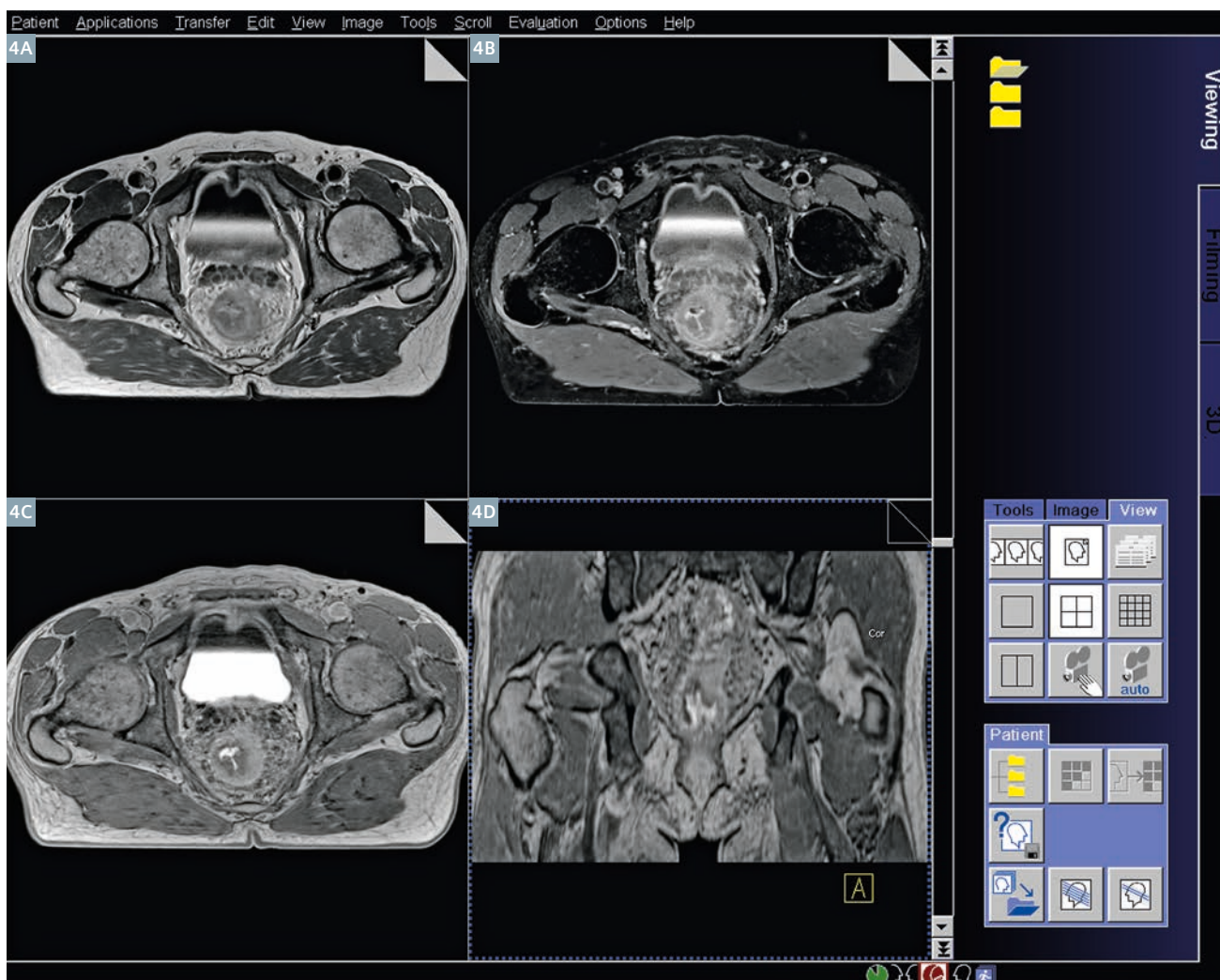
Table 2 gives examples for Tim 4G coil arrangements for RT imaging (sorted by body regions) and identifies the mounts from the CIVCO RT Positioning Package that could be used.

Feedback from the clinical community

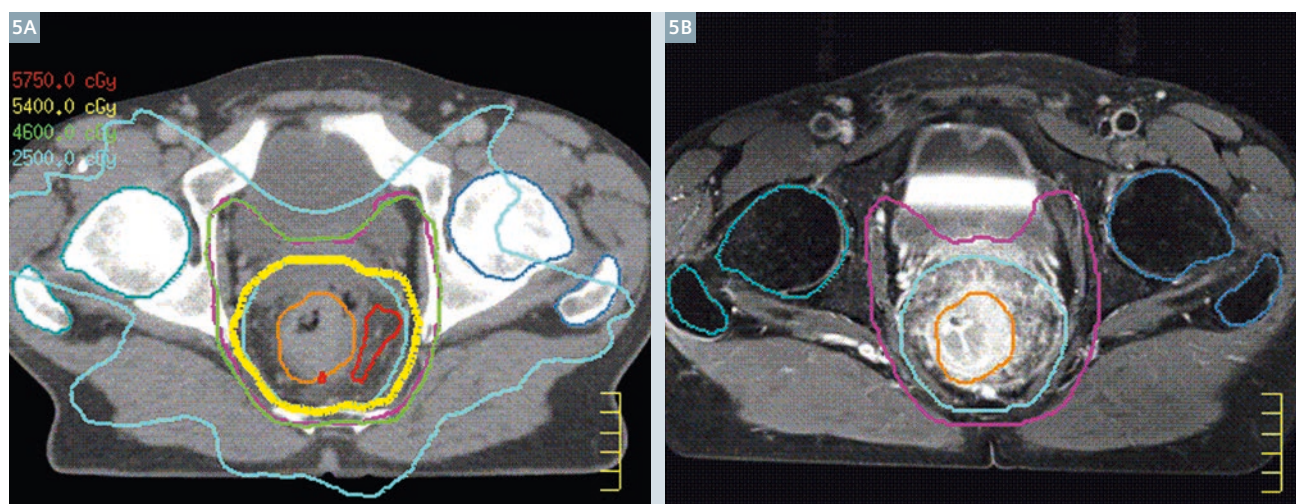
One of the first MAGNETOM Aera systems equipped with MAGNETOM Combi Suite Radiation Therapy options is installed in the Radiology department of the Sozialstiftung Bamberg in Bamberg, Germany. This scanner is a shared system, with reserved timeslots for radiation therapy treatment planning imaging. Dr. Thomas Koch, head of Medical Physics in the radiation oncology department at Bamberg, is impressed by the radiation therapy positioning package: "It works very well. It has made image fusion in our treatment planning system much easier and faster."



3 CT planning data of a patient with rectum carcinoma. (3A) Bone window, (3B) soft-tissue window).
 Courtesy of Sozialstiftung Bamberg, Bamberg, Germany.



4 Additional MR planning data for the same patient as in Fig. 3. (4A) T1-weighted contrast-enhanced TSE, (4B) T1w ce TSE fs, (4C) T1w 3D VIBE fs, (4D) coronal MPR of the 3D VIBE.
 Courtesy of Sozialstiftung Bamberg, Bamberg, Germany.



5 Image-based RT treatment planning for the same patient as in figures 3 and 4. **(5A)** CT with contoured organs and isodose lines, **(5B)** MR with contoured organs.
Courtesy of Sozialstiftung Bamberg, Bamberg, Germany.

Table 1:
Components of MAGNETOM Combi Suite Radiation Therapy

Components	Vendor	Remarks
Tim 4G coils	Siemens	required
Tim Dockable Table	Siemens	recommended
RT Positioning Package (MR-compatible couch top with indexing and coil mounts)	CIVCO	required; allows direct mounting of CIVCO Type S masks
External laser systems	LAP	recommended for virtual simulation

Note: MAGNETOM Combi Suite Radiation Therapy and its various components are available only for MAGNETOM Aera and MAGNETOM Skyra.

Table 2: Tim 4G coil arrangements for radiation therapy imaging

Region	Tim 4G coils	Mounting	Alternative / Option
Cranial	2-Flex 4 (Small/Large) with interfaces	Head coil mounts	1-Flex 4 (Small/Large) + Body 18
Head & Neck	2-Flex 4 (Small/Large) with interfacesw + Body 18 + Spine 32	Head coil mounts + Body coil mounts	1-Flex 4 (Small/Large) + Body 18 + Spine 32 coil
Abdominal	Body 18 + Spine 32 coil	Body coil mounts	a second Body 18 can be used for obese patients

Note: The brackets indicate alternatives.

Acknowledgement

I would like to thank Dr. Thomas Koch (Sozialstiftung Bamberg, Germany) for his kind support.

References

- 1 ASTRO www.rtanswers.org, 06/2013.
- 2 IMV 2010 Radiation Therapy Market Summary Report.

Contact

Annemarie Hausotte, Ph.D.
 Siemens Healthcare
 Imaging & Therapy Division
 Allee am Roethelheimpark 2
 91052 Erlangen, Germany

Phone: +49 9131 84-8931
 Mobile: +49 173 965-3714
annemarie.hausotte@siemens.com
siemens.com

The editorial staff at the German Cancer Research Center and at Siemens Healthcare extends their appreciation to all the radiologists, technologists, physicists, experts and scholars who donate their time and energy – without payment – in order to share their expertise with the readers of MAGNETOM Flash.

MAGNETOM Flash – Imprint

© 2013 by Siemens AG,
Berlin and Munich,
All Rights Reserved

Publisher:

Siemens AG

Medical Solutions
Business Unit Magnetic Resonance,
Karl-Schall-Straße 6, D-91052 Erlangen,
Germany

Guest Editor:

Professor Heinz-Peter Schlemmer, M.D.
Head of the Dept. of Radiology,
German Cancer Research Center.
Professor of Radiology,
University of Heidelberg, Germany

Associate Editor: Antje Hellwich
(antje.hellwich@siemens.com)

Editorial Board: Wellesley Were;
Ralph Strecker; Sven Zühlsdorff, Ph.D.;
Gary R. McNeal, MS (BME);
Peter Kreisler, Ph.D.

Production: Norbert Moser, Siemens AG,
Medical Solutions

Layout: independent Medien-Design
Widenmayerstrasse 16, D-80538 Munich,
Germany

Printer: G. Peschke Druckerei GmbH,
Schatzbogen 35, D-81829 Munich,
Germany

Note in accordance with § 33 Para.1 of
the German Federal Data Protection Law:
Despatch is made using an address file
which is maintained with the aid of an
automated data processing system.

MAGNETOM Flash is sent free of charge
to Siemens MR customers, qualified
physicians, technologists, physicists and
radiology departments throughout the
world. It includes reports in the English
language on magnetic resonance:
diagnostic and therapeutic methods and
their application as well as results and
experience gained with corresponding
systems and solutions. It introduces from
case to case new principles and proce-
dures and discusses their clinical poten-
tial. The statements and views of the
authors in the individual contributions
do not necessarily reflect the opinion of
the publisher.

The information presented in these
articles and case reports is for illustration
only and is not intended to be relied
upon by the reader for instruction as to
the practice of medicine. Any health
care practitioner reading this information
is reminded that they must use their
own learning, training and expertise in
dealing with their individual patients.
This material does not substitute for that
duty and is not intended by Siemens
Medical Solutions to be used for any
purpose in that regard. The drugs and
doses mentioned herein are consistent
with the approval labeling for uses and/or
indications of the drug. The treating
physician bears the sole responsibility for
the diagnosis and treatment of patients,
including drugs and doses prescribed in

connection with such use. The Operating
Instructions must always be strictly
followed when operating the MR system.
The sources for the technical data are the
corresponding data sheets. Results may
vary.

Partial reproduction in printed form of
individual contributions is permitted,
provided the customary bibliographical
data such as author's name and title of
the contribution as well as year, issue
number and pages of MAGNETOM Flash
are named, but the editors request that
two copies be sent to them. The written
consent of the authors and publisher is
required for the complete reprinting of
an article.

We welcome your questions and
comments about the editorial content of
MAGNETOM Flash. Please contact us at
magnetomworld.med@siemens.com.

Manuscripts as well as suggestions,
proposals and information are always
welcome; they are carefully examined
and submitted to the editorial board for
attention. MAGNETOM Flash is not
responsible for loss, damage, or any
other injury to unsolicited manuscripts
or other materials. We reserve the right
to edit for clarity, accuracy, and space.
Include your name, address, and phone
number and send to the editors, address
above.

MAGNETOM Flash is also available on the internet:

www.siemens.com/magnetom-world

Siemens Healthcare Publications

Our publications offer the latest information and background for every healthcare field. From the hospital director to the radiological assistant – here, you can quickly find information relevant to your needs.



MAGNETOM Flash
Everything from the world of magnetic resonance imaging.



SOMATOM Sessions
Everything from the world of computed tomography.



Imaging Life
Everything from the world of molecular imaging innovations.



AXIOM Innovations
Everything from the world of interventional radiology, cardiology, and surgery.



Heartbeat
Everything from the world of sustainable cardiovascular care.



Medical Solutions Online

The online version includes additional video features and greater depth to the articles in the printed healthcare leadership magazine. Read online at: www.siemens.com/medical-solutions

For current and past issues and to order the magazines, please visit www.siemens.com/healthcare-magazine

On account of certain regional limitations of sales rights and service availability, we cannot guarantee that all products included in this brochure are available through the Siemens sales organization worldwide. Availability and packaging may vary by country and is subject to change without prior notice. Some/All of the features and products described herein may not be available in the United States.

The information in this document contains general technical descriptions of specifications and options as well as standard and optional features which do not always have to be present in individual cases.

Siemens reserves the right to modify the design, packaging, specifications, and options described herein without prior notice.

Please contact your local Siemens sales representative for the most current information.

Note: Any technical data contained in this document may vary within defined tolerances. Original images always lose a certain amount of detail when reproduced.

Not for distribution in the US

Global Business Unit

Siemens AG
Medical Solutions
Magnetic Resonance
Henkestrasse 127
DE-91052 Erlangen
Germany
Phone: +49 9131 84-0
www.siemens.com/healthcare

Local Contact Information

Asia/Pacific:

Siemens Medical Solutions
Asia Pacific Headquarters
The Siemens Center
60 MacPherson Road
Singapore 348615
Phone: +65 6490 6000

Canada:

Siemens Canada Limited
Healthcare Sector
1550 Appleby Lane
Burlington, ON L7L 6X7, Canada
Phone +1 905 315-6868

Europe/Africa/Middle East:

Siemens AG, Healthcare Sector
Henkestr. 127
91052 Erlangen, Germany
Phone: +49 9131 84-0

Latin America:

Siemens S.A., Medical Solutions
Avenida de Pte. Julio A. Roca No 516, Piso
C1067 ABN Buenos Aires, Argentina
Phone: +54 11 4340-8400

USA:

Siemens Medical Solutions USA, Inc.
51 Valley Stream Parkway
Malvern, PA 19355-1406, USA
Phone: +1 888 826-9702

Global Siemens Headquarters

Siemens AG
Wittelsbacherplatz 2
80333 Munich
Germany

Global Siemens Healthcare Headquarters

Siemens AG
Healthcare Sector
Henkestrasse 127
91052 Erlangen
Germany
Phone: +49 9131 84-0
www.siemens.com/healthcare